

NUMERICAL STUDY OF THE FRACTIONAL QUANTUM HALL EFFECT: A
FEW-BODY PERSPECTIVE

A Dissertation

Submitted to the Faculty

of

Purdue University

by

Bin Yan

In Partial Fulfillment of the

Requirements for the Degree

of

Doctor of Philosophy

May 2019

Purdue University

West Lafayette, Indiana

THE PURDUE UNIVERSITY GRADUATE SCHOOL
STATEMENT OF DISSERTATION APPROVAL

Dr. Christopher H. Greene, Chair

Department of Physics and Astronomy

Dr. Francis Robicheaux

Department of Physics and Astronomy

Dr. Rudro R. Biswas

Department of Physics and Astronomy

Dr. Tongcang Li

Department of Physics and Astronomy

Approved by:

Dr. John P. Finley

Head of the Departmental Graduate Program

ACKNOWLEDGMENTS

First and foremost, I would like to express my sincere appreciation to my advisor, Professor Chris H. Greene. I have benefited so much from his great insights as a scientist, his enthusiasm and patience as an advisor, and his kindness and support during my graduate study. I learned so much from the many inspiring and fruitful conversations with Chris. The work presented in this dissertation would never have happened without his guidance and help.

I would like to thank the people that I have had the pleasure of working with directly at Purdue, especially Dr. Rachel Wooten and Dr. Kevin Daily for their inspiration and valuable help on my research. Having the opportunity to collaborate with Dr. Rudro R. Biswas is also a great and valuable experience. I want to thank every member of Greene's group. I have benefited a lot from active discussions with them.

I would like to thank all my friends for encouraging me with their best wishes. Last but not least, I thank my family for all their love and support. To them, I dedicate this dissertation.

TABLE OF CONTENTS

	Page
LIST OF TABLES	vi
LIST OF FIGURES	vii
ABSTRACT	x
1 INTRODUCTION	1
2 BASICS	4
2.1 Landau Levels	4
2.2 Degenerate Spaces	9
2.2.1 Single Particle Space	9
2.2.2 Many-Body Space	11
2.3 Fractional Quantum Hall States	16
2.3.1 Ground States at Fractional Filling Factors	16
2.3.2 Edge Modes	18
2.3.3 Bulk Excitations and Anyons	18
3 HYPERSPHERICAL REPRESENTATION	21
3.1 Hyperspherical Forms	22
3.1.1 Relative Hamiltonian	22
3.1.2 Coordinate Transformation	22
3.1.3 Grand Angular Momentum	23
3.2 Hyperspherical-Slater Determinant Transformation	25
3.2.1 Enumerating the Slater Determinants of a $\{K, M_{tot}\}$ Manifold	26
3.2.2 Operator Diagonalizations	28
3.2.3 Coulomb Matrix Elements at a Fixed Hyperradius	29
3.2.4 Two-Body Matrix Elements of the Coulomb Potential	30
3.2.5 Examples	31

	Page
3.3 Novel Excitations	33
3.3.1 Interacting Hyperspherical Forms	35
3.3.2 Collective Excitations	37
4 BULK-EDGE CORRESPONDENCE	45
4.1 Topological Order	46
4.2 Entanglement Entropy and Entanglement Spectrum	47
4.3 Bulk-Edge Correspondence	51
4.3.1 Model Edge States	55
4.3.2 Numerical Results	59
5 SUMMARY AND OUTLOOK	63
REFERENCES	65
A BOSON-FERMION CORRESPONDENCE	74
B TWO-BODY MATRIX ELEMENTS OF THE COULOMB POTENTIAL	77
C ENUMERATION OF SLATER DETERMINANTS OF A FIXED $\{K, M_{tot}\}$ MANIFOLD	81
D CENTER-OF-MASS OPERATORS	86
E ALGORITHMS FOR COMPUTING ENTANGLEMENT SPECTRUM	92
VITA	96

LIST OF TABLES

Table	Page
4.1 Table I from Ref. [100]. The number of edge modes at various angular momentum ΔM in the 14-orbital subsystem. The total system has 10 particles occupying 28 orbitals. Upper and lower tables correspond to five and four particles, respectively. P is the number of free edge modes, i.e., the number of restricted integer partitions. D_p represents the dimension of the Hilbert space of projected edge modes; D_m labels the observed multiplicity of levels in the entanglement spectrum.	59

LIST OF FIGURES

Figure	Page
1.1 Fig. 1 from Ref. [4]. Hall resistance $R_{xy} = V_y/I_x$ and magnetoresistance $R_{xx} = V_x/I_x$ versus the magnetic field.	2
2.1 The single particle wave functions in the lowest Landau level at $\phi=0$ for $m=0, -3, -10$, in the magnetic length scale.	6
2.2 Fig. 1 from Ref. [30]. Diagram describing the Landau levels and how the ladder operators move among the states $ \epsilon, m\rangle$, where ϵ is the Landau level and m is the 2-D angular momentum quantum number.	8
2.3 The magnitudes of the single particle wavefunctions for $m = 0, -3, -10$, in the magnetic length scale. In the lowest Landau level, single particle orbitals have ring-like shapes with widths on the order of the magnetic length scale.	10
2.4 Fig. 8 from Ref. [17]. Total degeneracy of anti-symmetric states for the four-body system in the lowest Landau level as a function of $ M $. Solid and dashed lines show upper and lower envelope functions, respectively, while the points show the number of degenerate anti-symmetric states in that manifold for each value of $ M $	15
2.5 Fig. 10 from Ref. [17]. Relative degeneracies for the six-body system are shown as a function of $ M $. Squares show the integer quantum Hall effect and the Laughlin $\nu = 1/3, 1/5, \dots$ states, triangles show the Jain states of two filled composite Landau levels, and circles show the remaining unidentified states.	16
2.6 Spectrum of eight electrons in the disk geometry under Coulomb interaction with total angular momentum $ M $ from 68 to 84. The Laughlin $1/3$ state and two filling factor in Jain's sequence have been identified.	19
2.7 The ground state single particle density profiles for six electrons. Blue line is the ground state density at $ M =45$, which is the $\nu = 1/3$ Laughlin state. Blue dashed line is the ground state at $ M =51$, which corresponds to a one-quasi-hole excitation. Red dotted line is the density line-shape of the quasi-hole state subtracted with the Laughlin ground state. Integration of the "hole region"(within around $r=2$) shows a total density $1/3$, which is identified as the $1/3$ positively charged quasi-hole.	20

Figure	Page
3.1 Fig. 2 from Ref. [30]. Hyperradial potential curves for a four-electron system. The blue lines (lower branch) are hyperradial potentials for $K = -M = 10$, which correspond to the lowest Landau level. The red lines (upper branch) correspond to $K = -M + 2 = 12$. The energy gap between separate clusters is approximately equal to the cyclotron excitation, while the smaller splittings within each branch are due to Coulomb interactions. The relative strength of the Coulomb interaction, $\kappa = \frac{e^2}{4\pi\epsilon\lambda_0 \hbar\omega_c}$, is set to be 1, which is the typical order for experiments in gallium arsenide.	32
3.2 Fig. 3 from Ref. [30]. The ground state energies of 8 particles in the lowest Landau level ($K = M $) at various K values as a function of the magnetic field, using experimental parameters matching a cold gallium arsenide system [65]. The magnetic field dependent zero-point energy has been subtracted for scale. The curves correspond to various K values ranging from $K = 28$ (filling factor $\nu = 1$) to $K = 84$ ($\nu = 1/3$). Curves for quantum Hall states at $\nu = 1, 2/3, 2/5$ and $1/3$ are marked as red lines from left to right respectively.	33
3.3 Fig. 1 from Ref. [51]. Hyperradial potential curves and the hyperradial bound states for the four particle, $\nu = 1$ system. The ground state for $\nu = 1$ has hyperangular quantum numbers $K = 6, M = -6$ and $n_R = 0$, and is totally isolated. The hyperradial excitation takes the system from the $n_R = 0$ state with energy E_0 to the first hyperradially excited state with $n_R = 1$ and energy E_1 . The E_0 plus the cyclotron energy is shown as a (blue) dashed line for contrast. Other excited potential curves and their ground state energies with the same M with are shown in pale grey.	38
3.4 Fig. 2 from Ref. [51]. (a) The hyperradial vibrational (HRV) mode excitation energies for Coulomb interactions as a function of κ for $N = 4, \dots, 9$ particles at $\nu = 1$ filling factor. From the lowest curve (red) with $N = 4$, the number of particles increases to $N = 9$ for the uppermost (black) curve. (b) The HRV energies for Coulomb interactions versus particle number for various filling factors [$\nu = 1$ (red crosses), $\nu = 2/3$ (green squares), $\nu = 2/5$ (blue triangles), and $\nu = 1/3$ (black circles)]. The values of κ are calculated from corresponding experimental magnetic fields in Tesla from [85]: $\nu = 1$ corresponds to 9T, $\nu = 2/3$ to 14T, $\nu = 2/5$ to 25T, and $\nu = 1/3$ to 29T. (c) The HRV excitation energies for dipole-dipole interactions as a function of κ . In this case the number of particles decreases from $N = 4$ downward to $N = 9$ on the plot. (d) The HRV energies for dipole-dipole interactions at $\kappa = 1$. The filling factors are labeled as in (b). For Coulomb interactions, the $\kappa = e^2/(4\pi\lambda_0\hbar\omega_c)$, and for dipole-dipole interactions, $\kappa = c_{dd}/(4\pi\lambda_0^3\hbar\omega_c)$, where c_{dd} is $\mu_0\mu_{mag}^2$ for polarized magnetic dipoles or d^2/ϵ_0 for polarized electric dipoles.	40

Figure	Page
3.5 Fig. 3 from Ref. [51]. The hyperradial vibrational modes versus κ for the $\nu = 1/3$ filling state for both (a) Coulomb, and (b) dipole-dipole interactions shown on the same scales relative to $\hbar\omega_c$. The detuning for the dipole-dipole interacting system exhibits stronger N dependence. . . .	41
4.1 Fig. 1 from Ref. [100]. Entanglement spectrum of the 17-orbital subsystem at the 6-particle sector. The total system of 12 particles in 34 total orbitals is prepared in (Upper) the ideal Laughlin state and (Lower) the realistic Coulomb interaction ground state. The color of the pseudo-energy levels indicate the overlaps between the corresponding entanglement spectrum eigenstates and the edge states of the subsystem. Inset: Entanglement entropy v.s. the square root of the number of orbitals (n_A) in subsystem A , which is proportional to the length of the boundary. The blue dashed line is our fit to the first 17 points, which are in the linear region away from the edge of the total system.	53
4.2 Fig. 2 from Ref. [100]. The projection probabilities for the whole entanglement spectrum of the 5-particle sector (left) and the 4-particle sector (right) for the case of Coulomb ground state. The cases of both ideal edge states (upper) and realistic edge states of Coulomb interaction are examined.	57
4.3 Fig. 3 from Ref. [100]. Typical patterns for the projection probabilities. Red squares represent the probabilities for 5 particles at $\Delta M = 6$ ($ M = 36$). Blue dots correspond to the 4-particle sector at $\Delta M = 8$ ($ M = 26$). Projection probabilities are computed using (a) the model edge states for the Laughlin case and (b) the real edge states for Coulomb interactions. . . .	58
4.4 Fig. 4 from Ref. [100]. The spectrum of 5 particles under the Haldane V_1 pseudo-potential with an open boundary condition (red levels) and with the same boundary condition as the 14-orbital subsystem (blue levels). The blue levels are shifted slightly to the right from their corresponding angular momenta. For the case of an open boundary condition, the degeneracies of the ground states are 1, 1, 2, 3, 5, 7, which are identical to the number of the ideal edge states.	62
C.1 Diagram describing the ordering of the single-particle orbitals $ \epsilon, m\rangle$ by Landau level and order of the polynomial.	82

ABSTRACT

Yan, Bin Ph.D., Purdue University, May 2019. Numerical Study of the Fractional Quantum Hall Effect: a Few-Body Perspective. Major Professor: Chris H. Greene.

When confined to a finite, two-dimensional area and exposed to a strong magnetic field, electrons exhibit a complicated, highly correlated quantum behavior known as the quantum Hall effect. This dissertation consists of finite size numerical investigations of this effect. One line of study develops treatment of the fractional quantum Hall effect using the hyperspherical method, in conjunction with applications to the few-body quantum Hall systems, e.g., highly-controlled atomic systems. Another line of research fully utilizes the developed numerical techniques to study on the platform of finite size fractional quantum Hall states the bulk-edge correspondence principle, which is universal for phases in topological orders. It has been demonstrated that the eigenstates associated with the entanglement spectrum reveal more information about the ground state than the spectrum alone.

1. INTRODUCTION

Electrons in two-dimensions exhibit very interesting behaviors. In strong magnetic fields, electrons condense into phases that contain fractionally charged quasi-particles [1, 2] obeying fractional statistics. These new phases are known as the quantum Hall effect [3–5], which cannot be classified within Landau’s symmetry breaking picture. In typical experiments on two-dimensional electron systems, the Hall resistance and the magnetoresistance are shown to have quantized values at integer and certain fractional filling factors. Extensive headway has been made in developing a theoretical picture of this effect [6–16], but it still remains far from being completely understood.

In recent years, there has been significant interest and progress in reproducing and studying the quantum Hall effect and its bosonic analog in highly-controlled atomic systems. Among those developments, recent theoretical work [17] tackled the quantum Hall problem from a completely different viewpoint by using the hyperspherical adiabatic technique [18–20] developed originally for atomic systems [21–23]. On one hand, it brought new insight into the field of quantum Hall physics. On the other hand, it introduced theoretical toolkits that are more suitable for the study of quantum Hall effect in few-body systems, such as electrons in quantum dots and cold atoms in rotational traps [24–28].

In one line of studies in this dissertation, we continue pursuing in this direction. Numerical techniques are developed to back up the previous hyperspherical approach and push our capacity to numerically probe a larger number of particles. The hyperspherical method is then applied to study the collective excitations in few-body fractional quantum Hall systems. Novel excitations called the hyperradial breathing modes are predicted.

The fractional quantum Hall system is one of the cornerstones in modern condensed matter physics. It is the first experimentally measured and theoretically

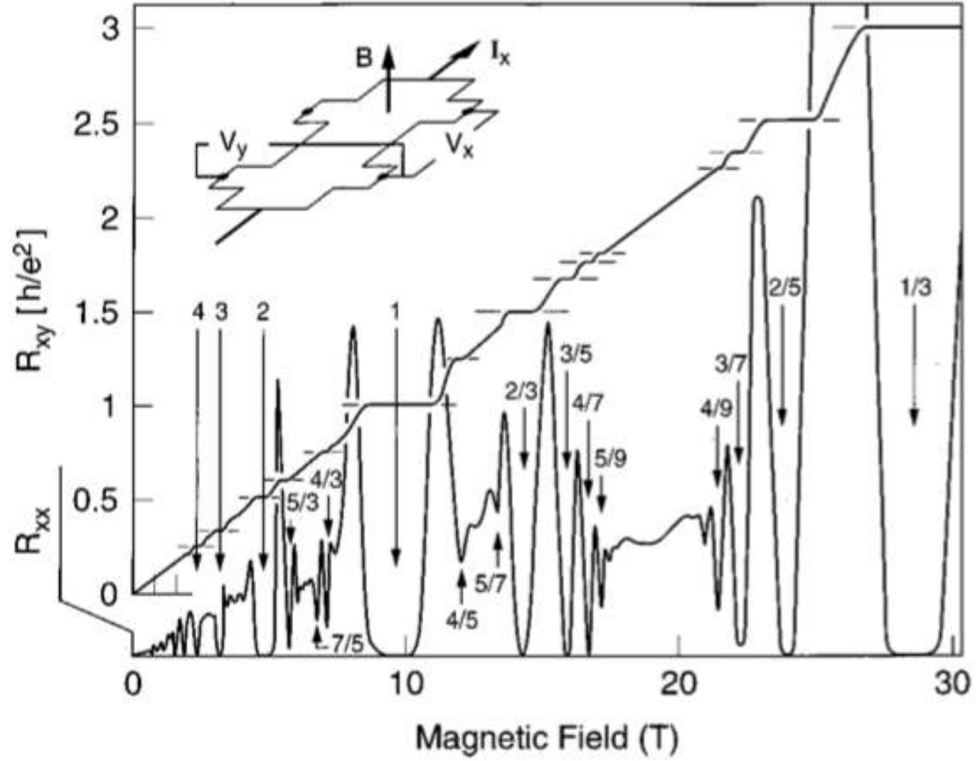


Fig. 1.1. Fig. 1 from Ref. [4]. Hall resistance $R_{xy} = V_y/I_x$ and magnetoresistance $R_{xx} = V_x/I_x$ versus the magnetic field.

recognized system that shows non-trivial topological orders, which go beyond the conventional Landau symmetry breaking classifications of the phases of matter. Another line of research of this dissertation studies the principle called the bulk-edge correspondence, which is a universal principle for states having a topological order. We perform the first finite system numerical calculation using the platform of fractional quantum Hall states to verify this principle.

The dissertation is organized as follows. Chapter 2 reviews the basic Landau level physics: the localized single particle orbitals in two dimensions with the perpendicular magnetic field; the Landau level index, angular momentum quantum numbers; as well as the degenerate single-particle and many-body Hilbert spaces. The concept

of exceptional degeneracy shows deep connections between the fractional quantum Hall states and the relative degeneracy of the underlying non-interacting many-body Hilbert space. We also derive the correspondence between the fermion and boson Hilbert spaces. Basics for the fractional quantum Hall ground states and quasi-hole (particle) excitations are also reviewed. Chapter 3 introduces the hyperspherical representation of the many-electron basis functions, with which the fractional quantum Hall problem was solved. A technique that connects the hyperspherical method and the conventional Slater-determinant approach is also presented. An application of the hyperspherical method to study the collective excitation of the fractional quantum Hall system is developed. Chapter 4 discusses the bulk-edge correspondence in fractional quantum Hall states. A historical line of the developments for the search of “order parameters” for the topological phases is reviewed, which leads to the principle called the bulk-edge correspondence. A finite size numerical study that confirms this principle is presented. Chapter 5 summarizes this dissertation and discusses future directions.

2. BASICS

2.1 Landau Levels

The Hamiltonian for a non-relativistic electron with mass m_e in two dimensions in a perpendicular magnetic field is given by

$$H = \frac{1}{2m_e}(-i\hbar\nabla + e\mathbf{A})^2 \quad (2.1)$$

in SI unit, where the electron charge is defined as $-e$. \mathbf{A} is the vector potential of the uniform magnetic field, $B\hat{z} = \nabla \times \mathbf{A}$. The eigenstate and eigenvalue problem of the above Hamiltonian can be solved under a special choice of gauge, the symmetric gauge,

$$\mathbf{A} = \frac{\mathbf{B} \times \mathbf{r}}{2} = \frac{B}{2}(-y, x, 0), \quad (2.2)$$

which preserves the rotational symmetry of the system.

With this choice of \mathbf{A} , the Hamiltonian can be written in Cartesian coordinates as

$$H = -\frac{\hbar^2}{2m_e}\nabla^2 + \frac{e^2B^2}{8m_e}(x^2 + y^2) + \frac{eB}{2m_e}L_z, \quad (2.3)$$

where $L_z = -i\hbar(x\partial_y - y\partial_x)$ is the z -component of the angular momentum operator. In the magnetic length scale where length is expressed in the units of l_B ,

$$l_B = \sqrt{\frac{\hbar}{m_e\omega_c}}, \quad (2.4)$$

the Hamiltonian is further reduced to the following form in polar coordinates:

$$H = -\frac{1}{2}\left\{\frac{1}{r}\partial_r r\partial_r - \frac{L_z^2}{\hbar^2 r^2}\right\} + \frac{1}{8}r^2 + \frac{1}{2\hbar}L_z. \quad (2.5)$$

The single particle eigenstate in this gauge in the magnetic length scale can be written as:

$$\psi_n^m(r, \phi) = \sqrt{\frac{n!}{2^{|m|+1}\pi(n+|m|)!}} e^{im\phi} r^{|m|} e^{-r^2/4} L_n^{|m|}(r^2/2), \quad (2.6)$$

with energy and angular momentum

$$\begin{aligned} E &= \hbar\omega_c\left(n + \frac{m + |m|}{2} + \frac{1}{2}\right), \quad n = 0, 1, 2, \dots, +\infty, \\ L_z &= m\hbar, \quad m = \infty, \dots, 0, -1, -2, \dots -\infty. \end{aligned} \quad (2.7)$$

Here $L_n^{|M|}$ is the associated Laguerre polynomial. The energy levels separated by $\hbar\omega_c = \hbar \frac{eB}{m_b c}$ are called Landau levels. $\omega_c \equiv eB/m_e$ is the cyclotron frequency. n and m are the radial quantum number and the rotational quantum number about the z -axis, respectively.

It is more convenient to use the Landau level label ϵ instead of the radial quantum number n ; these are related by

$$\epsilon = n + \frac{m + |m|}{2}. \quad (2.8)$$

States with the same Landau level label ϵ all share the same energy in unit of $\hbar\omega_c$,

$$E^{(1)} = \epsilon + \frac{1}{2}. \quad (2.9)$$

The Landau level spacing is proportional to the strength of the magnetic field. In the limit of an infinite magnetic field, or equivalently the zero mass limit, the kinetic energy dominates the interaction energy scale between particles. One can restrict the problem to the lowest Landau level. In a typical quantum Hall experiment in GaAs, the ground state gap under Coulomb interaction is smaller than the cyclotron energy by one order of magnitude. Theoretical studies ignoring Landau level mixing have correctly predicted most of the universal features of the quantum Hall effect. In the following, unless specified in certain problems, we will restrict the discussion to the spin-polarized particles in the lowest Landau level.

In the lowest Landau level, the only free quantum number of the single-particle states is the angular momentum quantum number m . Wave function Eq. (2.6) is then reduced to

$$\begin{aligned} \psi^m(r, \phi) &= \sqrt{\frac{1}{2^{|m|+1}\pi|m|!}} e^{im\phi} r^{|m|} e^{-r^2/4} \\ &\propto z^{|m|} e^{-z\bar{z}/4}, \end{aligned} \quad (2.10)$$

which has a beautiful feature as an analytic function, multiplying an overall Gaussian factor, in the two dimensional complex coordinate $z = x - iy$. Fig. 2.1 and Fig. 2.3. show the plots of the wave function Eq. (2.10) for different values of m . Those single particle orbitals are localized in ring shapes with widths on the order of a few magnetic lengths.

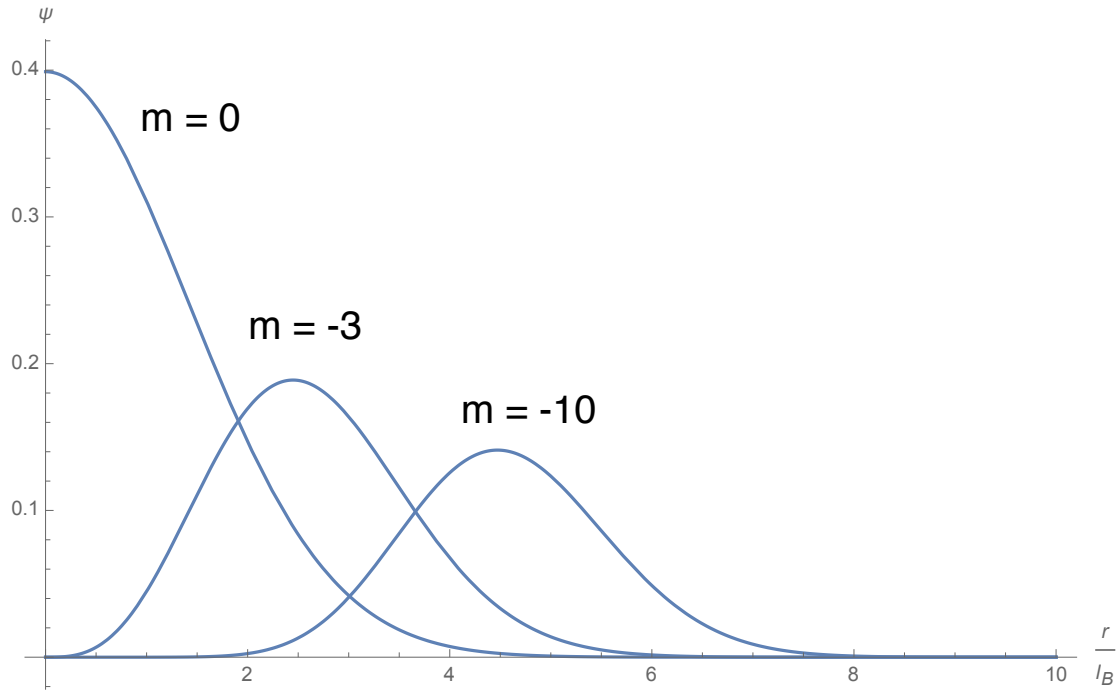


Fig. 2.1. The single particle wave functions in the lowest Landau level at $\phi=0$ for $m=0, -3, -10$, in the magnetic length scale.

It is convenient to express the single-particle states in bra-ket notation, $|\epsilon, m\rangle$. The well-known ladder operators cause transitions among the single-particle states [29]. The effect of the operators on the kets is summarized below:

$$\begin{aligned}
b |\epsilon, m\rangle &= \begin{cases} +1, & m < 0 \\ -1, & m \geq 0 \end{cases} \sqrt{\epsilon - m} |\epsilon, m + 1\rangle \\
b^\dagger |\epsilon, m\rangle &= \begin{cases} +1, & m \leq 0 \\ -1, & m > 0 \end{cases} \sqrt{\epsilon - m + 1} |\epsilon, m - 1\rangle \\
a |\epsilon, m\rangle &= \begin{cases} +1, & m > 0 \\ -1, & m \leq 0 \end{cases} \sqrt{\epsilon} |\epsilon - 1, m - 1\rangle \\
a^\dagger |\epsilon, m\rangle &= \begin{cases} +1, & m \geq 0 \\ -1, & m < 0 \end{cases} \sqrt{\epsilon + 1} |\epsilon + 1, m + 1\rangle \\
ab |\epsilon, m\rangle &= -\sqrt{\epsilon}\sqrt{\epsilon - m} |\epsilon - 1, m\rangle \\
a^\dagger b^\dagger |\epsilon, m\rangle &= -\sqrt{\epsilon + 1}\sqrt{\epsilon + 1 - m} |\epsilon + 1, m\rangle
\end{aligned} \tag{2.11}$$

The lowest rung of each ladder obeys

$$\begin{aligned}
b |\epsilon, \epsilon\rangle &= 0 \\
a |0, m\rangle &= 0.
\end{aligned} \tag{2.12}$$

Figure 2.2 depicts the single-particle states, arranged according to m along the horizontal and Landau level ϵ along the vertical. Red lines indicate states that are neighbors according to the b and b^\dagger operators. The b operators raise the m quantum number up to the maximum value where m is equal to the Landau level, e.g. for the lowest level $m_{\max} = 0$. Blue lines indicate states that are neighbors according to the a and a^\dagger operators. The a operators lower the Landau level to a minimum value of $\epsilon = 0$, while simultaneously modifying the m quantum number by one unit each time a or a^\dagger is applied. Green lines indicate states that are neighbors according to the ab and $a^\dagger b^\dagger$ operators. These combined operators raise or lower the Landau level while preserving the m quantum number. In Chapter 3, these convention and rules of ladder operators will be used to derive transformations between two representations of the many electron basis functions.

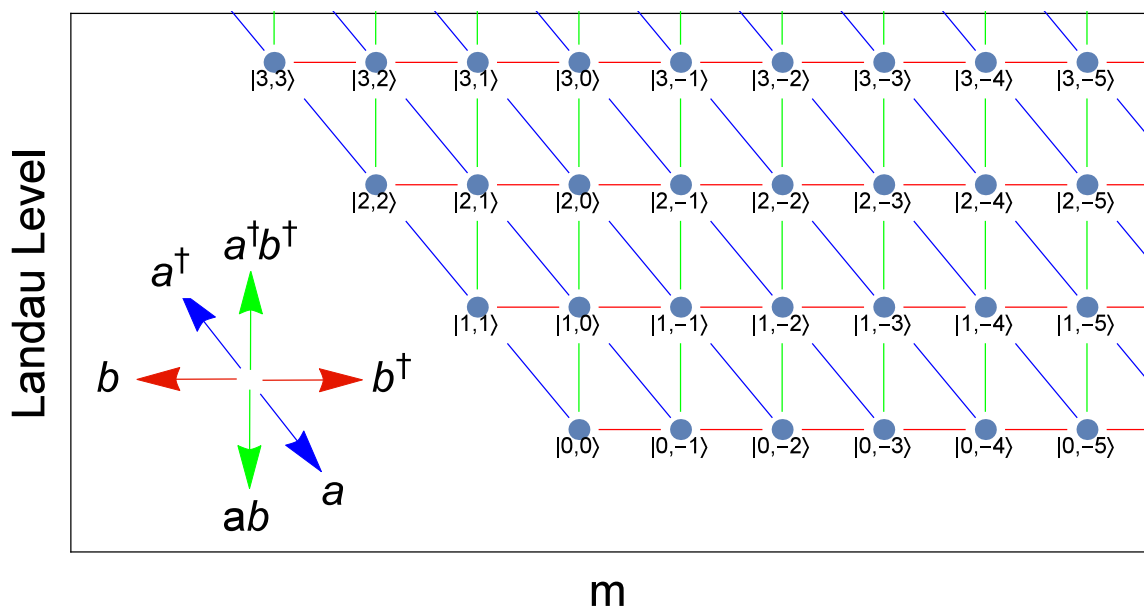


Fig. 2.2. Fig. 1 from Ref. [30]. Diagram describing the Landau levels and how the ladder operators move among the states $|\epsilon, m\rangle$, where ϵ is the Landau level and m is the 2-D angular momentum quantum number.

2.2 Degenerate Spaces

We first discuss the degenerate single particle Hilbert space, and then construct the many-body Hilbert space with the direct product of single-particle spaces. Degeneracy of the system can be traced from two different directions: 1) The physical system is confined to a finite area, and 2) the system has no sharp boundaries. The former case is most suitable for the conventional condensed matter systems, where the electrons are restricted to a finite macroscopic area, e.g., the two-dimensional GaAs system. The latter case is the best platform for the study of few-body systems, for instance, electrons in quantum dots or cold atoms in rotational traps.

2.2.1 Single Particle Space

For the case of finite area restriction, we discuss the degeneracy of the system in the thermodynamic limit, namely, where the size of the area is much larger than the magnetic length. To preserve the rotational symmetry, we use the symmetric gauge and assume that the system has a disk geometry with radius R . In the thermodynamic limit, the degeneracy of the single particle space has a topological nature and does not rely on the particular shape of the boundaries. In the disk geometry, the allowed single particle orbitals are those that appear mostly within the radius R . By “mostly” we mean that the peak values of the single particle wave functions are less than the radius of the disk. Away from the peak, the single particle wave functions damp very quickly over the distance scale of magnetic length, thus, only a few single particle orbitals near the boundary are modified by the boundary potential. The total degeneracy, in the thermodynamic limit, is thus barely affected. The rigorous proof of the counting of degeneracy can be found elsewhere [31].

Simple calculation demonstrates that the peak values of the single particle orbitals appears at

$$r_{peak}^2 = (2|m| + 1) \frac{\hbar c}{eB}. \quad (2.13)$$

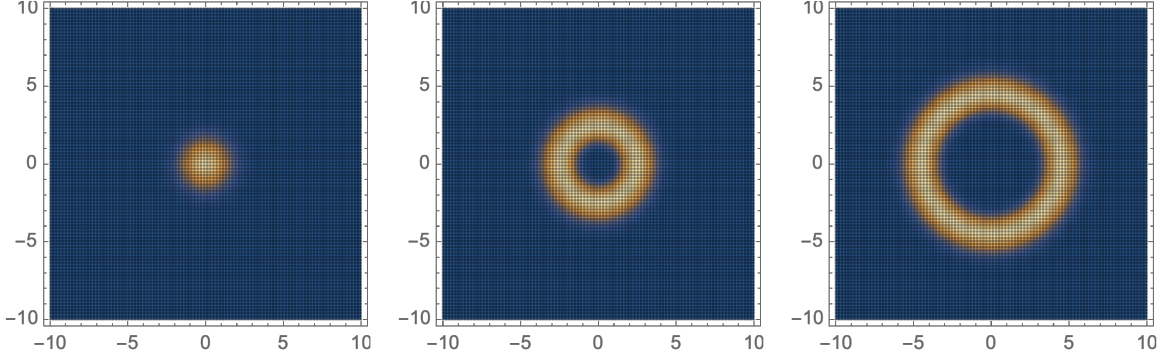


Fig. 2.3. The magnitudes of the single particle wavefunctions for $m = 0, -3, -10$, in the magnetic length scale. In the lowest Landau level, single particle orbitals have ring-like shapes with widths on the order of the magnetic length scale.

The number of single particle states that exist within the disk area, in the limit of $|m| \gg 1$, is given by solving $r_{peak} = R$, that is,

$$\begin{aligned}
 N_\phi &= 2R^2 \frac{eB}{\hbar c} \\
 &= \frac{\Phi}{\Phi_0},
 \end{aligned}
 \tag{2.14}$$

where $\Phi = \pi R^2 B$ is the total magnetic flux going through the system, and $\Phi_0 = \frac{\hbar c}{e}$ is defined as the magnetic flux quanta. Thus, the number of allowed single particle states within a given area is equal to the number of magnetic flux quanta within that area.

The integer quantum Hall effect happens when all the allowed single particle states in some given number of Landau levels are occupied, in other words, the ratio of the number of electrons and the number of flux quanta, $\nu = N_e/N_\phi$, equals an integer. To explain the fractional quantum Hall effect, where ν is a fractional number, one has to include the interactions between particles. When interaction is considered, a gapped ground state is then selected from the degenerate many-body Hilbert space.

Calculations of the spectrum and the properties of low-lying states of the fractional quantum Hall problem will be discussed in the following chapters.

2.2.2 Many-Body Space

The many-body Fock space can be constructed as the direct product of the allowed single particle spaces.

For systems without confining potentials, or few-body systems where the boundary effect is crucial even for the bulk state, one cannot truncate the single-particle Hilbert space by cutting the real space with hard wall boundaries as described in the last section. The many-body interaction problem should then be solved within the many-body Hilbert space constructed from all the single-particle states. However, when considering a many-particle problem, since the centripetal nature of a typical realistic two body interaction, e.g., Coulomb interaction between electrons or P-wave contact interaction in cold atoms, the total angular momentum ($M_{tot} = \sum_i m_i$) of a given number of particles is still a good quantum number. One can thus focus on the Hilbert subspace \mathcal{H}_M which has a fixed total angular momentum M . Furthermore, the statistics of the particle under consideration requires the total many-body wave functions to be symmetric (for bosons) or anti-symmetric (for fermions). \mathcal{H}_M can then be decomposed into the direct sum of three orthogonal subspaces:

$$\mathcal{H}_M = \mathcal{H}_M^s \oplus \mathcal{H}_M^a \oplus \mathcal{H}_M^u, \quad (2.15)$$

where $\mathcal{H}_M^s, \mathcal{H}_M^a, \mathcal{H}_M^u$ are the sub-spaces (subset for \mathcal{H}_M^u) of symmetric, anti-symmetric and asymmetric functions, respectively.

In some cases it is more convenient to further separate out the center-of-mass motion and define the fixed relative angular momentum subspace $\{M_{rel}\}$ as a subspace of $\{M_{tot}\}$, in which all basis functions have vanishing center-of-mass angular momentum. In the following section describing the hyperspherical approach, we also define another quantum number, K , exact for the non-interacting systems and still an approximately good quantum number in the presence of interactions, which labels

the eigenvalue of the grand angular momentum operator \hat{K}^2 . The resulting subspace with fixed values of K and M is then called the $\{K, M\}$ manifold.

Basis Functions— There are many choices of the many-body wave function basis. Two commonly used sets of basis functions for the spaces \mathcal{H}_M^s and \mathcal{H}_M^a are boson permanents and fermion Slater determinants. A formal definition of these basis functions is given in Appendix A. In the next chapter, we also introduce a set of basis functions in collective coordinates of the many-particle system, namely, the hyperspherical functions. A transformation between the conventional Slater determinants and the hyperspherical basis functions is also given.

Boson-Fermion Mapping— The Hilbert space of N bosons with total angular momentum M is isomorphic to the Hilbert space of N fermions with total angular momentum $M + \frac{N(N-1)}{2}$, which we denote as

$$\mathcal{H}_M^s \cong \mathcal{H}_{M + \frac{N(N-1)}{2}}^a. \quad (2.16)$$

This can be shown [32] to derive from the simple fact that for each symmetric polynomial $P(z_i)$ of N variables of total order M , there exists an antisymmetric polynomial $P'(z_i) = \prod_{i < j} (z_i - z_j) P(z_i)$ of order $M + \frac{N(N-1)}{2}$, where $\prod_{i < j} (z_i - z_j)$ is the Vandermonde polynomial [33]. Thus, the mapping from the Hilbert space of N bosons to the Hilbert space of N fermions can be defined as a multiplication of a Vandermonde polynomial equipped with a proper normalization factor:

$$\mathcal{F} : \psi(\{z_i\}) \in \mathcal{H}_M^s \rightarrow \mathcal{N} \prod_{i < j}^N (z_i - z_j) \psi(\{z_i\}) \in \mathcal{H}_{M + \frac{N(N-1)}{2}}^a. \quad (2.17)$$

Here, ψ is a normalized N -body symmetric wave function. \mathcal{N} is a normalization factor that makes the resulting N -body fermionic wave function normalized. Given a set of many-body basis functions in the Hilbert space \mathcal{H}_M^s (or \mathcal{H}_M^a), turning on the interaction between particles breaks the degeneracy of the system. A natural question to ask is that, is the fractional quantum Hall ground state or the quasi-hole state in \mathcal{H}_M^a , mapped to a ground state or quasi-hole like state in the corresponding fermionic state in $\mathcal{H}_{M - \frac{N(N-1)}{2}}^s$? This is a highly non-trivial problem. Due to different

statistics of boson and fermion, projected interactions in the two different spaces take completely different forms. There is no simple reason to say that the dynamics of bosons and fermions in their corresponding spaces should be linked in this way. To answer this question, we develop the representation of the mapping \mathcal{F} , which is derived in Appendix A.

Exceptional Degeneracy— In this section, we compute the degeneracy $d^a(N, M)$ of the Hilbert space \mathcal{H}_M^a for the given N particles. The trend of degeneracy $d(N, M)$ as a function of M is shown [17] to have a positive correlation with the ground state energy gaps for a small number of particles. That is, for filling factors where there is a large ground state energy gap, which is usually an indication of a fractional quantum Hall state, the underlying degenerate space without interaction also shows a relatively larger degeneracy than the neighborhood spaces. This relation was understood from a perturbation theory picture [17], that is, in a set of functions, turning on interactions will typically act to lower the energy of the ground state relative to all the higher-energy states. This effect is strengthened by the presence of additional degeneracy in the system. As a result, it is predicted [17] that manifolds with exceptionally high degeneracy are likely to also produce identifiable fractional quantum Hall states.

The degeneracy of space \mathcal{H}_M^s is given by Eq. (25) of [34]

$$d^s(N, M) = p_N(M) - p_{N-1}(M), \quad (2.18)$$

where $p_N(M)$ is the number of partitions of the integer M into parts no longer than N . $p_N(M)$ can be calculated using a generating function [35]

$$Z_N(x) = \prod_{j=1}^N \frac{1}{1-x^j} = \sum_{M=1}^{\infty} x^M p_N(M). \quad (2.19)$$

The above two equations, combined with the fact that there is an exact mapping between \mathcal{H}_M^s and $\mathcal{H}_{M+\frac{N(N-1)}{2}}^a$, the degeneracy $d^a(N, M)$ of the fermion space \mathcal{H}_M^a can be calculated by the following generating function [17]:

$$G_N(x) = x^{N(N-1)} \prod_{j=2}^N \frac{1}{1-x^j} = \sum_{M=0}^{\infty} x^M d^a(N, M). \quad (2.20)$$

The degeneracy given by the above equations has been verified [17] to match exactly to brute force calculations for many values of N and M . Fig. 2.4 shows the degeneracy $d^a(4, M)$ for the four-particle system as a function of M . It can be seen that the general trend as $|M|$ increases is that the total degeneracy oscillates about an overall polynomial growth.

In order to extract the small variations of the degeneracy on top of the overall polynomial growth, we apply the method as described in Ref. [17] of deriving two polynomial functions that envelop the degeneracies and then compare the relative heights above the lower envelope. The upper and lower envelop functions are defined by extracting the polynomial part of $d^a(N, M)$ giving by Eq. (2.20), and then forcing the polynomial going through the integer quantum Hall point at $|M| = \frac{N(N-1)}{2}$ and zero degeneracy value at $|M| = \frac{N(N-1)}{2} + 1$. As depicted in Fig. 2.4, the solid and dashed lines show the upper and lower envelope functions, respectively. As a concrete example, consider the four particle case. The exact solution of the degeneracy is giving by Eq. (56) of [17]:

$$d^a(4, M) = \frac{1}{48}M^2 + \frac{(-1)^{|M|} - 1}{16}|M| + \frac{1}{288}[-27(-1)^{|M|} - 1 + 36 \sin(\frac{\pi|M|}{2}) - 36 \cos(\frac{\pi|M|}{2}) + 64 \cos(\frac{2\pi|M|}{3})]. \quad (2.21)$$

The upper and lower envelop polynomial satisfying the above requirement are [17]:

$$\begin{aligned} d_{upp}^a(4, M) &= \frac{1}{48}M^2 + \frac{1}{4}, \\ d_{low}^a(4, M) &= \frac{1}{48}M^2 - \frac{M}{8} - \frac{7}{48}. \end{aligned} \quad (2.22)$$

More detailed calculation can be found in Ref. [17]. From the upper and lower envelope functions, the relative degeneracy $d_{rel}^a(N, M)$ is defined by Eq. (59) of [17]:

$$d_{rel}^a(N, M) = \frac{d^a(N, M) - d_{low}^a(N, M)}{d_{upp}^a(N, M) - d^a(N, M)}, \quad (2.23)$$

which is, the relative height of $d^a(N, M)$ above the lower envelope, with respect to the separation between the two envelope functions.

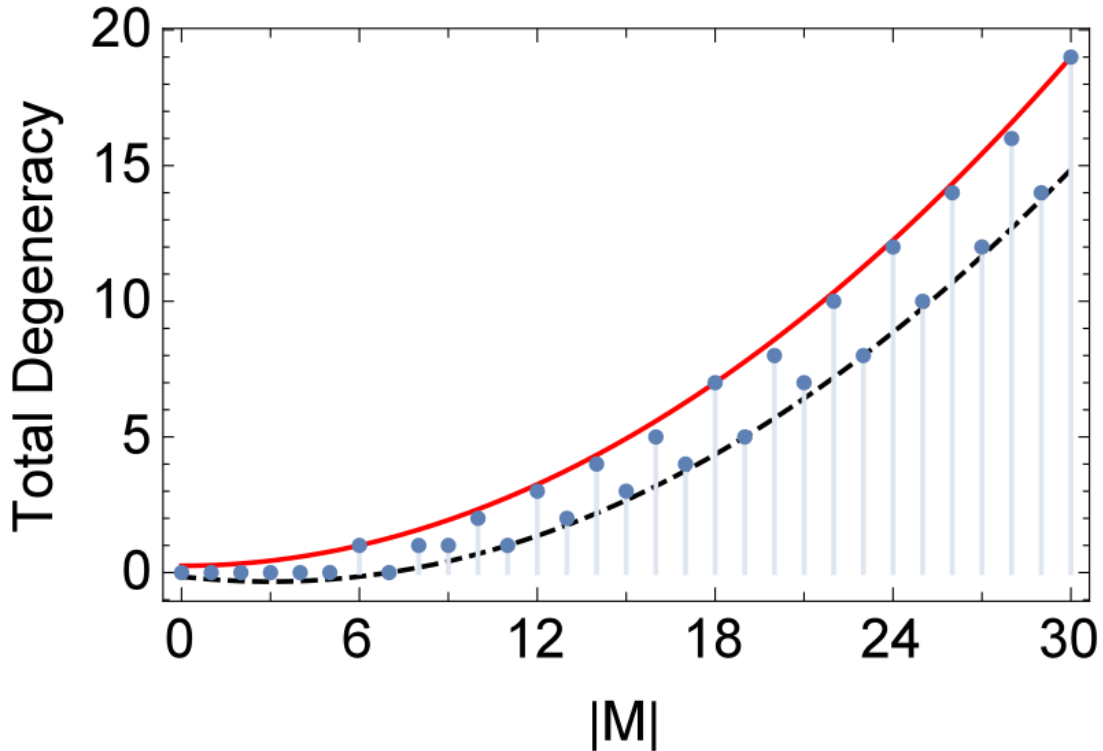


Fig. 2.4. Fig. 8 from Ref. [17]. Total degeneracy of anti-symmetric states for the four-body system in the lowest Landau level as a function of $|M|$. Solid and dashed lines show upper and lower envelope functions, respectively, while the points show the number of degenerate anti-symmetric states in that manifold for each value of $|M|$

Fig. 2.5 shows the relative degeneracy $d_{rel}^a(6, M)$ of the six-body system as calculated from Eq. (2.23) as a function of M . The squares mark the degeneracies of the integer quantum Hall and Laughlin states. The triangles identify the degeneracies of Jain states of two filled composite fermion Landau levels. Circles show the remaining unidentified states.

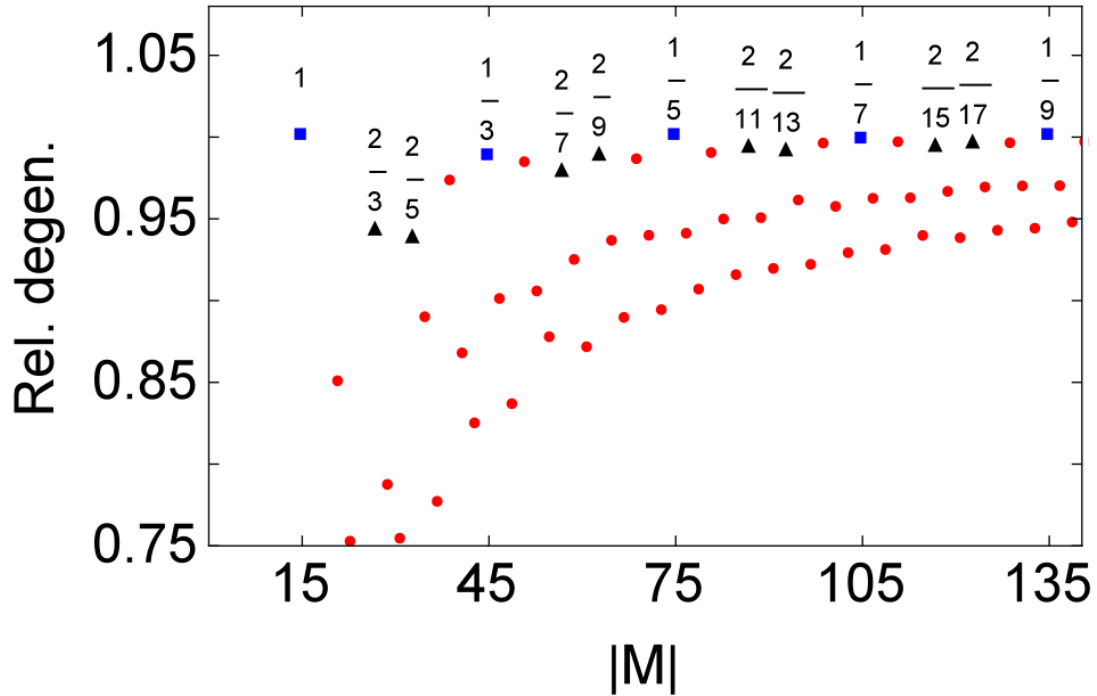


Fig. 2.5. Fig. 10 from Ref. [17]. Relative degeneracies for the six-body system are shown as a function of $|M|$. Squares show the integer quantum Hall effect and the Laughlin $\nu = 1/3, 1/5, \dots$ states, triangles show the Jain states of two filled composite Landau levels, and circles show the remaining unidentified states.

2.3 Fractional Quantum Hall States

2.3.1 Ground States at Fractional Filling Factors

At certain strength of the magnetic field, the Hall conductance exhibits plateaus regimes. This happens when the filling factor, i.e., the ratio between the number of electrons and the number of magnetic flux quanta equals certain fractional numbers. At these filling fractions the electrons condense into a ground state with non-trivial topological orders. The system is incompressible, i.e., there is a finite gap for the bulk excitations. However, there exist gapless excitations on the edge. Bulk excitations

are also well described by fractionally charged quasi-particles, with novel exchange symmetry. These particles are classified as (non-)Abelian anyons with fractional statistics.

Studies of the quantum Hall ground states at fractional filling factors fall into two categories: The low energy effective (topological) field theory, and the wavefunction approach. The latter include model wavefunctions, e.g., Laughlin's wavefunction, Haldane and Halperin hierarchy, Jain's sequences, and finite size numerical simulations. This work will focus on the wavefunction perspective.

To illustrate the basic ideas, take for example the simplest case of filling factors $\nu = 1/m$, where for fermions (bosons) m is an odd (even) integer. Laughlin's famous wavefunction for the ground state at these filling factors is

$$\mathcal{N} \prod_{i < j}^N (z_i - z_j)^m \prod_i e^{-\frac{|z_i|^2}{4}} \quad (2.24)$$

in the magnetic length scale. Here \mathcal{N} is a normalization constant, and $z = x - iy$ is the two-dimensional complex coordinate for particles. It can be seen that for N particles, the highest order of the monomials for any particle is $m(N - 1)$, which, according to the single particle basis functions in the lowest Landau level, corresponds to the outermost orbit, the one with the largest angular momentum magnitude equal to $m(N - 1)$. Thus, the system has $m(N - 1) + 1$ magnetic flux quanta, which corresponds to a filling factor $\nu = N/(m(N - 1) + 1) \approx 1/m$ for large N .

The Laughlin state is verified by carrying out numerically exact diagonalizations. Fig. 2.6 shows an example for the spectrum of the quantum Hall Hamiltonian with Coulomb interactions. The Laughlin $\nu = 1/3$ state is identified with a relatively larger gap separating the energy from the rest of the spectrum. For few-body calculations, the Laughlin state has an overlap with the realistic ground state for that corresponding value of M which is close to unity. However, it is known that this high degree of overlap is not preserved in the thermodynamic limit. Nevertheless, the Laughlin state captures many of the crucial features of the fractional quantum Hall states.

2.3.2 Edge Modes

When the total angular momentum of the system is slightly away from the critical total angular momentum, which corresponds to a particular fractional quantum Hall state, the state of the system is described by the gapless edge excitations on top of the fractional quantum Hall state. Take for instance the edge excitations near $\nu = 1/m$, the edge excitations can be modeled by the following (unnormalized) wavefunction,

$$\Psi_{edge} = \prod_i s_{n_i} \prod_{i < j} (z_i - z_j)^{1/\nu} \prod_i e^{-\frac{|z_i|^2}{4}}, \quad (2.25)$$

where $s_n = \sum_i z_i^n$ is the power sum symmetric polynomial. These edge modes are indistinguishable from the Laughlin ground states in the bulk, but exhibit extra structures on the edge. Chapter 4 will further explore and utilize these model edge excitations to study the bulk-edge correspondence principle in the fractional quantum Hall states.

2.3.3 Bulk Excitations and Anyons

When the ratio of the number of electrons to the number of magnetic flux quanta is away from the filling fractions where there exist fractional quantum Hall states, e.g., the magnetic field is slight tuned away from the critical values such that the number of magnetic flux is increased (decreased), the system condenses into states which are described by excitations of quasi-holes (quasi-particles) on top of the fractional quantum Hall state.

For instance, the following (unnormalized) wavefunction describes a quasi-hole excited from the Laughlin wavefunction at filling factor $\nu = 1/m$:

$$\prod_i z_i \prod_{i < j}^N (z_i - z_j)^m \prod_i e^{-\frac{|z_i|^2}{4}}. \quad (2.26)$$

In this case the total angular momentum is increased by $|\Delta M| = N$, and the total number of flux quanta is increased by one. This corresponds to a quasi-hole excitation at the center of the system ($z = 0$). This excitation possesses a fractional charge e/m .

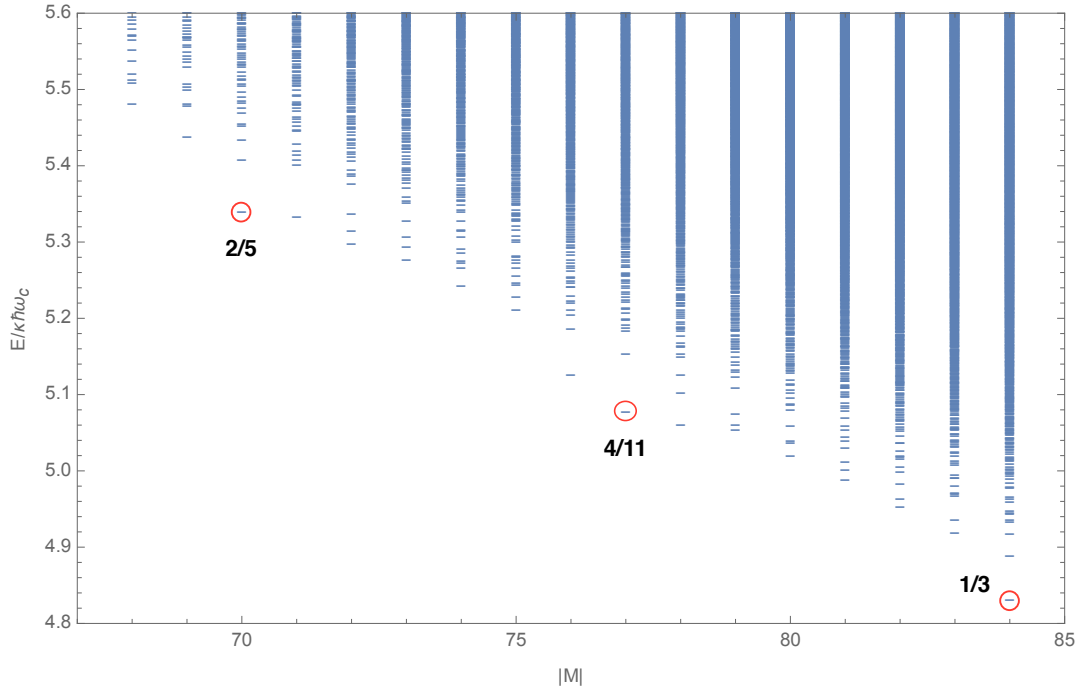


Fig. 2.6. Spectrum of eight electrons in the disk geometry under Coulomb interaction with total angular momentum $|M|$ from 68 to 84. The Laughlin $1/3$ state and two filling factor in Jain's sequence have been identified.

The fractional quantum Hall ground states are expected to have a uniform single particle density,

$$\rho = \sum_{i=1}^N \delta(\vec{r} - \vec{r}_i), \quad (2.27)$$

which preserves the translational and rotational symmetry of the Hamiltonian. Single particle profiles also help to identify quasi-particle structures of the excited states. In Fig. 2.7, we plot the single particle density of the six-electron $1/3$ Laughlin state, as well as the one with a single quasi-hole excitation. The non-uniform density is explained as the strong edge effect in the finite size few-body system. We thus subtract the non-uniform background from the quasi-hole density, such that the edge effect is

eliminated. The resulting density profile (dotted red line in Fig. 2.7) shows a clear hole-structure, which carries approximate $1/3$ positive charge.

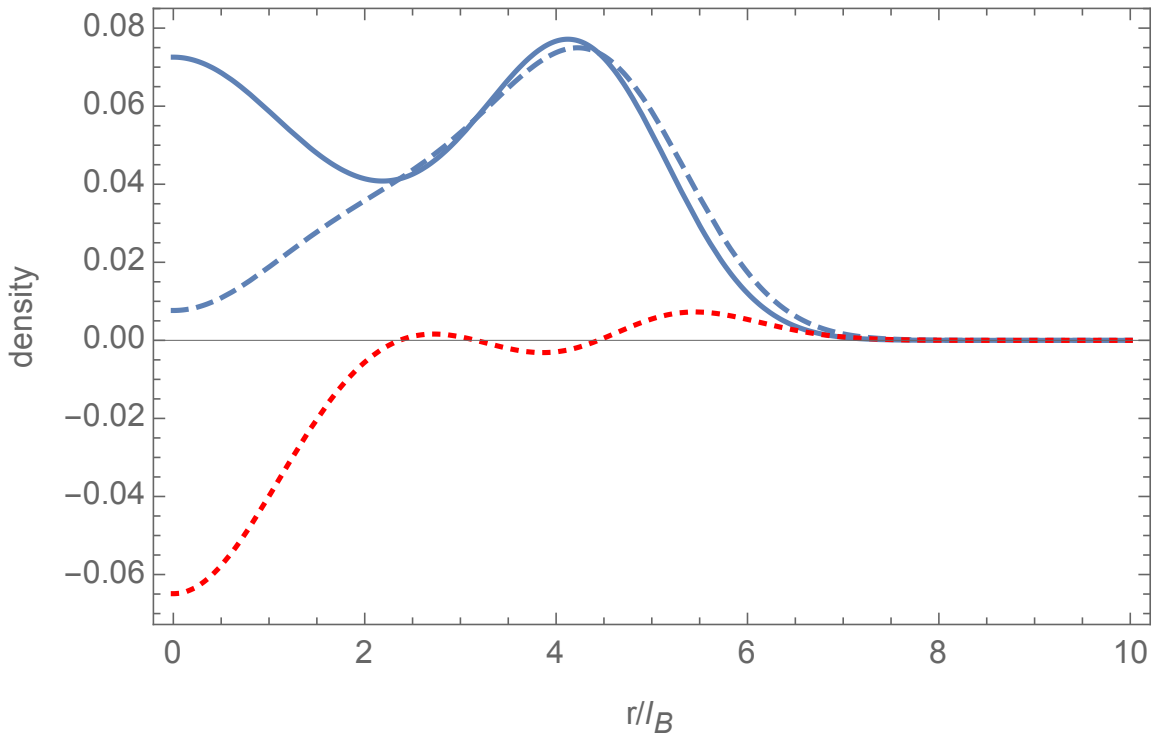


Fig. 2.7. The ground state single particle density profiles for six electrons. Blue line is the ground state density at $|M|=45$, which is the $\nu = 1/3$ Laughlin state. Blue dashed line is the ground state at $|M|=51$, which corresponds to a one-quasi-hole excitation. Red dotted line is the density line-shape of the quasi-hole state subtracted with the Laughlin ground state. Integration of the "hole region" (within around $r=2$) shows a total density $1/3$, which is identified as the $1/3$ positively charged quasi-hole.

3. HYPERSPHERICAL REPRESENTATION

As has been outlined in the previous chapter, the fractional quantum Hall effect has been tackled in various approaches, including the low energy effective topological field theories, model wavefunctions, as well as exact numerical diagonalizations. Different approaches have their own advantages and capture certain aspects of the problem.

On the other hand, in the past decade, continued interest in reproducing and studying the fermionic quantum Hall effect and its bosonic analog in highly-controlled atomic systems also demands innovative and unconventional methods of studying the few-body quantum Hall effect. This motivated a more recent line of attack [17], which developed a novel approach to the quantum Hall problem was presented that is based on the adiabatic hyperspherical representation [18–20], which originated in and has been extensively used in the context of few-body physics [20–23]. In contrast to the conventional techniques which use the single particle representations, such as the Slater determinant construction of the many body wavefunction, this approach inherently uses collective coordinates. Thus the hyperspherical method not only provides complementary advantages and alternative qualitative pictures compared to previous methods, it is also more suitable for the discussion of few-body systems (i.e., cold atoms in rotating traps [24–28], electrons in a quantum dot [36–49]). Other recent studies have successfully applied the hyperspherical method to the study of the two-dimensional three-boson problems [50] in the presence of a perpendicular magnetic field, and to the study of inter-Landau level collective excitations [51].

3.1 Hyperspherical Forms

3.1.1 Relative Hamiltonian

In contrast to the conventional approach, where the many-body states are constructed using a single particle basis, the hyperspherical method treats the many-body Hamiltonian collectively, namely, the many-body basis functions are solved directly from the Schrödinger equation. To achieve this, we first separate the N-body noninteracting Hamiltonian H_N into center-of-mass (H_{CM}) and relative (H_{rel}) components. The center-of-mass behaves like an independent single particle, while the non-interacting relative Hamiltonian takes the form of

$$H_{rel} = -\frac{1}{2\mu} \sum_{j=1}^{N_{rel}} \nabla_j^2 + \frac{\mu}{8} \sum_{j=1}^{N_{rel}} (x_j^2 + y_j^2) + \frac{1}{2\hbar} \sum_{j=1}^{N_{rel}} L_{z_j}^{rel}, \quad (3.1)$$

where x_j and y_j are the Cartesian components of $N_{rel} = N - 1$ relative Jacobi vectors $\boldsymbol{\rho}_j$, and μ is a dimensionless mass scaling factor [52, 53],

$$\mu = \left(\frac{1}{N}\right)^{1/N_{rel}}. \quad (3.2)$$

The definition of Jacobi vectors in terms of single particle coordinates is somewhat arbitrary. (As an example of the transformation, see Sec. III in Ref. [17])

3.1.2 Coordinate Transformation

The hyperspherical coordinates are a high dimension analogue of the three-dimensional spherical coordinates. The overall size of the system is characterized by a single scalar coordinate, the hyperradius R , which is defined as

$$R^2 = \sum_{j=1}^{N_{rel}} \rho_j^2. \quad (3.3)$$

The remaining degrees of freedom, which represent the geometry of the system, are encoded in a set of coordinates, the hyperangles $\boldsymbol{\Omega}$. The definition of the hyperangles has some arbitrariness, and there are many different schemes in the literature [54–

56]. The major focus of this paper does not depend on the specific definition of the hyperangles. To see a concrete example of this transformation, refer to Sec. IV.A in Ref [17].

3.1.3 Grand Angular Momentum

Under the transformation to hyperspherical coordinates, the relative non-interacting Hamiltonian, Eq. (3.1), transforms to

$$H_{\text{rel}} = -\frac{1}{2\mu}\nabla_{R,\Omega}^2 + \frac{\mu}{8}R^2 + \frac{1}{2\hbar}L_z^{\text{rel,tot}}. \quad (3.4)$$

Here $L_z^{\text{rel,tot}}$ is the z -component of the total relative angular momentum. The Laplacian operator in hyperspherical coordinates is given by

$$\nabla_{R,\Omega}^2 = \frac{1}{R^{2N_{\text{rel}}-1}}\partial_R R^{2N_{\text{rel}}-1}\partial_R - \frac{\hat{\mathbf{K}}^2}{R^2}. \quad (3.5)$$

$\hat{\mathbf{K}}$ is called the grand angular momentum operator [55], whose eigenfunctions are represented by the orthonormal hyperspherical harmonics $\Phi_{Ku}^{(M)}(\Omega)$, where

$$\hat{\mathbf{K}}^2\Phi_{Ku}^{(M)}(\Omega) = K(K + 2N_{\text{rel}} - 2)\Phi_{Ku}^{(M)}(\Omega). \quad (3.6)$$

Here, the subscript u labels different degenerate eigenfunctions with the same K and M . M is the quantum number of the total relative angular momentum, which is a good quantum number for any central two-body potential. The hyperspherical harmonics $\Phi_{Ku}^{(M)}(\Omega)$ are the simultaneous eigenstates of $\hat{\mathbf{K}}^2$ and $L_z^{\text{rel,tot}}$ under constraint $|M| \leq K$.

For the non-interacting case, the hyperspherical harmonics $\Phi_{Ku}^{(M)}(\Omega)$ are exact analytical solutions, labeled by the index u for given good quantum number K for the grand angular momentum and M for the total angular momentum. The detailed form of the solutions depends on the choice of hyperspherical coordinate transformation described in the previous section. Ref. [17] presents a semicanonical coupling scheme for the coordinate transformation and the corresponding hyperspherical harmonics expressions.

However, the hyperspherical harmonics $\Phi_{Ku}^{(M)}(\boldsymbol{\Omega})$ are in general non-symmetrized, i.e., not admitting any symmetry under particle exchanges. The intrinsic statistics of electrons demands that the total wavefunctions must be anti-symmetric respect to exchanges of any two particle coordinates. The hyperradial part (as a function of the hyperradius R) is by definition symmetric. The hyperspherical harmonics thus need to be anti-symmetrized before serving as basis functions. Ref. [17] developed a procedure to anti-symmetrize the hyperspherical harmonics, by find proper linear combinations of the un-symmetrized harmonics $\Phi_{Ku}^{(M)}(\boldsymbol{\Omega})$ within a space of fixed quantum number K and M . The anti-symmetrized hyperspherical harmonics are labeled by a new index a as $\Phi_{Ka}^{(M)}(\boldsymbol{\Omega})$.

The full eigensolutions of the non-interacting relative Hamiltonian (3.4) are separable into anti-symmetrized hyperspherical harmonics $\Phi_{Ka}^{(M)}(\boldsymbol{\Omega})$ and hyperradial functions $F_{n_R K}^{(M)}(R)$,

$$\Psi(R, \boldsymbol{\Omega}) = R^{-N_{\text{rel}}+1/2} F_{n_R K}^{(M)}(R) \Phi_{Ka}^{(M)}(\boldsymbol{\Omega}). \quad (3.7)$$

The hyperradial functions $F_{n_R K}^{(M)}(R)$ satisfy a one-dimensional differential equation, the scaled Schrodinger equation:

$$\left\{ -\frac{1}{2\mu} \frac{d^2}{dR^2} + U_K^{(M)}(R) - E \right\} F_{n_R K}^{(M)}(R) = 0, \quad (3.8)$$

where the hyperradial potentials $U_K^{(M)}(R)$ are given by

$$U_K^{(M)}(R) = \frac{(K + N_{\text{rel}} - 1/2)(K + N_{\text{rel}} - 3/2)}{2\mu R^2} + \frac{\mu}{8} R^2 + \frac{1}{2} M. \quad (3.9)$$

Under this potential, the hyperradial functions also admit exact analytical solutions:

$$F_{n_R K}^{(M)}(R) = \mathcal{N} e^{-\frac{\mu R^2}{4}} L_{n_R}^{K+N_{\text{rel}}-1} \left(\frac{\mu R^2}{2} \right) R^{K+N_{\text{rel}}-1/2}, \quad (3.10)$$

where L is the associate Laguerre polynomial and $n_R = 0, 1, 2, \dots$ is the hyperradial quantum number. The normalization constant is given by

$$\mathcal{N} = \sqrt{\frac{n_R! \mu^{K+N_{\text{rel}}}}{\Gamma(n_R + K + N_{\text{rel}}) 2^{K+N_{\text{rel}}-1}}}. \quad (3.11)$$

The many-body states Eq. (3.7) then serve as the basis for the study of interacting problems. In practice, an adiabatic approximation that initially treats the hyperradius R as a parameter is adopted, in other words, the fixed R Hamiltonian is diagonalized at a fixed hyperradius in the space of hyperspherical harmonics.

We note the following remarks. 1) The forms of the hyperspherical harmonics $\Phi_{Ku}^{(M)}(\Omega)$ depend on the coordinate transformation scheme. They are simple functions to express in hyperspherical coordinates, but become cumbersome to use as the computational basis when re-expressed in particle Cartesian coordinates. 2) The grand angular momentum quantum number K ($K = 0, 1, 2, \dots$) is a good quantum number in the noninteracting limit, and it has been demonstrated to be an approximately good quantum number even in the presence of Coulomb interactions. 3) There are $(2N_{\text{rel}} - 2 + 2K)(2N_{\text{rel}} - 3 + K)! / (K!(2N_{\text{rel}} - 2)!)$ linearly independent hyperspherical harmonics in a given K manifold. However, these basis functions generally do not possess the proper symmetry under particle permutation. Thus a process of finding all linear combinations that have the desired symmetric must be performed, which makes the use of the hyperspherical basis functions even more challenging. The next section develops a method to minimize the above difficulties, by implementing a representation of the anti-symmetrized hyperspherical harmonics in terms of Slater determinants of single particle basis functions (See also Refs. [56–60]).

3.2 Hyperspherical-Slater Determinant Transformation

The hyperspherical approach discussed in the previous sections in this chapter tackles the quantum Hall problem from a collective perspective. Through a coordinate transformation, this method solves the many-body Schrödinger equation directly in terms of hyperspherical harmonics. This point of view highlights many key properties of the system which do not emerge naturally from the independent particle framework. However, a drawback of the hyperspherical method is that the hyperspherical harmonics do not *a priori* possess any intrinsic particle permutation

symmetry, while the many-fermion wavefunctions are required to be antisymmetric under particle exchange. As a consequence, an anti-symmetrization process should normally be performed in order to generate basis functions with the proper exchange symmetry [17, 61–64]. (The many-boson problem also poses a similar drawback with symmetrization. An alternative method sometimes used to attack this (anti-)symmetrization problem is via postsymmetrization [22], which we do not pursue here, because we prefer to work with far smaller pre-symmetrized basis sets.) This (anti-)symmetrization step is the main bottleneck limiting the computational power of the hyperspherical method. In order to solve this problem, we implement here a basis of Slater determinants (permanents) which can overcome this difficulty because they are explicitly antisymmetrized (symmetrized). We establish here the reduction of the conventional Slater determinant basis functions to the many-body hyperspherical basis function spaces [30]. A similar technique has previously been implemented in some nuclear physics calculations [57–60].

3.2.1 Enumerating the Slater Determinants of a $\{K, M_{tot}\}$ Manifold

The first task is to find all possible Slater determinants that can form part of a given $\{K, M_{tot}\}$ manifold with the center of mass included. Here, M_{tot} is the total projection quantum number, $M_{tot} = \sum_{j=1}^N m_j$, and K is the grand angular momentum quantum number. K , as was shown in a previous study [17], is an approximately good quantum number in the many-body quantum Hall problem. In fact, K is equal to the order of the harmonic polynomial of the many-body wave function in a fixed $\{K, M_{tot}\}$ manifold. Producing the list of N -particle Slater determinants that span a given fixed $\{K, M_{tot}\}$ manifold is equivalent to finding the complete list of sets of N single-particle orbitals that obey a short list of restrictions:

1. All N single particle orbitals selected for a given Slater determinant must be allowed:

- The maximum order of the polynomial part of any single particle orbital, given by $k_i = 2\epsilon_i - m_i$ for the i^{th} orbital must be greater than or equal to zero, $2\epsilon_i - m_i \geq 0$
 - The radial quantum number, n_i , for the i^{th} orbital must be non-negative, $n_i \geq 0$. This restricts the selection of $\epsilon_i = n_i + (m_i + |m_i|)/2$,
2. The total angular momentum M_{tot} is the sum of the single-particle m_i values,

$$M_{tot} = \sum_{i=1}^N m_i. \quad (3.12)$$

3. The total grand angular momentum, K , is equal to the total order of the N -particle harmonic polynomial of the product of the selected N single-particle orbitals. This is determined by the rule

$$K = \sum_{i=1}^N (2\epsilon_i - m_i). \quad (3.13)$$

The total orders of the single particle polynomials are represented graphically in Fig. C.1.

4. For fermions, the orbitals must all be different in order to satisfy the Pauli exclusion principle.

Each set of N single-particle orbitals that satisfies this list of rules defines a single Slater determinant in the desired $\{K, M_{tot}\}$ manifold. The complete set of all Slater determinants that satisfy these rules spans the entire $\{K, M_{tot}\}$ manifold basis, and each totally hyperspherical function in that $\{K, M_{tot}\}$ manifold that is antisymmetric with respect to particle-interchange can be expressed as a linear combination of these Slater determinants.

This Slater determinant list can be found directly by testing all single-particle orbital sets that satisfy this list of rules, although the procedure is somewhat tedious to carry out by hand and requires significant testing. An alternative streamlined and more systematic method of finding the complete set of Slater determinants of a fixed

$\{K, M_{tot}\}$ manifold using integer partitions and contingency tables is described in Appendix C.

3.2.2 Operator Diagonalizations

If the functional space is reduced to states in which the center of mass is in its absolute ground state, then that also implies that $K_{CM} = 0$. Thus, finding the eigenvalues of K_{tot} for the set of center-of-mass-reduced states is effectively equivalent to the problem of finding the eigenvalues of K_{rel} .

The relevant operators for this work are

$$L_{CM} = \frac{\hbar}{N} \sum_{j=1}^N (a^\dagger a - b^\dagger b)_j + \frac{\hbar}{2N} \sum_{j=1}^N \sum_{k \neq j}^N \left[a_k^\dagger a_j + a_j^\dagger a_k - (b_k^\dagger b_j + b_j^\dagger b_k) \right], \quad (3.14)$$

$$H_{CM} = \frac{1}{2} + \frac{1}{N} \sum_{j=1}^N a_j^\dagger a_j + \frac{1}{2N} \sum_{j=1}^N \sum_{k \neq j}^N (a_k^\dagger a_j + a_j^\dagger a_k), \quad (3.15)$$

and

$$\begin{aligned} \hat{K}^2 = & \sum_{j=1}^N \left([a^\dagger a - b^\dagger b]_j^2 + (2N - 2) [a^\dagger a + b^\dagger b]_j \right) \\ & + \sum_j \sum_{k \neq j} \left([a^\dagger a + b^\dagger b]_j [a^\dagger a + b^\dagger b]_k - 2 (a_j^\dagger b_j^\dagger a_k b_k + a_j b_j a_k^\dagger b_k^\dagger) \right). \end{aligned} \quad (3.16)$$

The detailed derivations of these operator expressions are given in Appendix D.

In practice, for a given set of Slater determinant basis functions, the L_{CM} operator is diagonalized and the eigenvectors corresponding to 0 eigenvalue are selected. Next, the H_{CM} operator is diagonalized in the basis of $L_{CM} = 0$ states and the eigenvectors with corresponding 1/2 eigenvalues are selected. Lastly, if necessary, the \hat{K}^2 operator is diagonalized in the basis of $L_{CM} = 0$, $E_{CM} = 1/2$, and the eigenvectors with corresponding $K(K + 2N - 2)$ eigenvalues (the minimum eigenvalues) are selected. In the lowest Landau level, there are zero Landau level excitations and all states having $L_{CM} = 0$ turn out to have the smallest possible value of $K(K + 2N - 2)$, which are the eigenvalues of the \hat{K}^2 operator. Thus only the L_{CM} operator needs to be diagonalized.

3.2.3 Coulomb Matrix Elements at a Fixed Hyperradius

We assume we have basis functions $\Psi(\mathbf{r}_1, \mathbf{r}_2, \dots)$ in the independent particle Slater determinant representation with $L_{CM} = 0$, $E_{CM} = 1/2$, and fixed M . We may also sometimes need matrix elements between basis functions having different values of K . Matrix elements at a fixed hyperradius R can be computed by equating the integral over all Cartesian coordinates with the integral over the center of mass and the relative function expressed in hyperspherical coordinates.

Our starting point is

$$\begin{aligned} & \int \Psi_{K'}^*(\mathbf{r}_1, \mathbf{r}_2, \dots) V(\mathbf{r}_{12}) \Psi_K(\mathbf{r}_1, \mathbf{r}_2, \dots) d\mathbf{r}_1 d\mathbf{r}_2 \dots \\ &= \int |\Psi(\mathbf{R}_{CM})|^2 d\mathbf{R}_{CM} \int \Psi_{K'}^*(R; \Omega) V(R; \Omega) \Psi_K(R; \Omega) R^{2N-1} dR d\Omega \end{aligned} \quad (3.17)$$

where it is assumed that for every basis function the center of mass is in its absolute ground state and can be separated off. The basis functions are labeled by the K quantum number. The left-hand-side of Eq. (3.17) is assumed to be known from standard Slater determinant basis methods and we label it I . The center of mass integral on the right-hand-side of Eq. (3.17) is unity. Moreover, the hyperradial and hyperangular parts of the basis functions are known. This leaves

$$\begin{aligned} I &= \int \Psi_{K'}^*(R; \Omega) V(R; \Omega) \Psi_K(R; \Omega) R^{2N-1} dR d\Omega \\ &= \int \Phi_{K'}^*(\Omega) \left(\int \mathcal{N}^* e^{-\frac{\mu}{4} R^2} R^{K'} V(R; \Omega) \mathcal{N} e^{-\frac{\mu}{4} R^2} R^K R^{2N-1} dR \right) \Phi_K(\Omega) d\Omega \end{aligned} \quad (3.18)$$

where \mathcal{N} is the normalization of the hyperradial wave function. In the case of power law potentials, the hyperradial dependence of the interaction potential V is separable, $V(R; \Omega) = R^p V(\Omega)$. Thus the hyperradial integral can be factored from the hyperangular integral, which leaves

$$\frac{I}{\langle K' | R^p | K \rangle} = \int \Phi_{K'}^*(\Omega) V(\Omega) \Phi_K(\Omega) d\Omega \quad (3.19)$$

where $\langle K' | R^p | K \rangle$ is the hyperradial matrix element,

$$\langle K' | R^p | K \rangle = \left(\frac{2}{\mu} \right)^{p/2} \frac{\Gamma([K + K' + 2N + p]/2)}{\sqrt{\Gamma(K + N) \Gamma(K' + N)}}. \quad (3.20)$$

3.2.4 Two-Body Matrix Elements of the Coulomb Potential

According to the Slater-Condon rules, the matrix elements of any two-body operators \hat{O} in the basis of N-body Slater determinants $|\epsilon_1, m_1\rangle|\epsilon_2, m_2\rangle\dots|\epsilon_N, m_N\rangle$ can be expressed as a sum in terms of two-body matrix elements

$$\langle\epsilon_1, m_1|\langle\epsilon_2, m_2|\hat{O}_{12}|\epsilon_1', m_1'\rangle|\epsilon_2', m_2'\rangle, \quad (3.21)$$

where the number 1 and 2 label the two particles. In the case of Coulomb interactions, or a general class of interactions where the potential depends only on the inter-particle distance r , it is more convenient to compute the two-body matrix element in terms of center-of-mass and relative coordinates,

$$\langle N, M|\langle n, m|\hat{O}(r)|N', M'\rangle|n', m'\rangle = \delta_{N,N'}\delta_{M,M'}\langle n, m|\hat{O}(r)|n', m'\rangle, \quad (3.22)$$

where we use $|N, M\rangle(|n, m\rangle)$ to label the center-of-mass(relative) coordinate state.

The only non-vanishing transformation coefficients are these between bases that satisfy the condition

$$\begin{aligned} i + j &= N \\ k + l &= N - M \\ \epsilon_1 + \epsilon_2 &= N + n \\ m_1 + m_2 &= M + m, \end{aligned} \quad (3.23)$$

which is given by

$$\begin{aligned} &\langle \epsilon_1 m_1 \epsilon_2 m_2 | N M n m \rangle \\ &= \mathcal{C} \frac{\mathcal{A}_1 \mathcal{A}_2}{\mathcal{A}_c \mathcal{A}_r} \sum_{i=0}^{\epsilon_1} \sum_{j=0}^{\epsilon_2} \sum_{k=0}^{\epsilon_1 - m_1} \sum_{l=0}^{\epsilon_2 - m_2} (-1)^{2\epsilon_2 - m_2 - j - l} C_{\epsilon_1}^i C_{\epsilon_2}^j C_{\epsilon_1 - m_1}^k C_{\epsilon_2 - m_2}^l, \end{aligned} \quad (3.24)$$

where $\mathcal{C} = (1/\sqrt{2})^{2\epsilon_1 + 2\epsilon_2 - m_1 - m_2}$ and

$$\mathcal{A} = \frac{(-1)^{\min\{n, n-m\}}}{\sqrt{n!(n-m)!}}, \quad (3.25)$$

the subscripts of which are labels of the corresponding particle. Derivation of the above transformation can be find in Appendix B.

3.2.5 Examples

As a concrete example of implementing the procedure described above, a four-electron system is studied in this section. The table below lists the number of Slater determinants at various values of K s. The total angular momentum M is fixed to be -10 .

K	10	12	14
D1	5	41	144
D2	2	7	12

D1 is the number of Slater determinants that may be part of the $\{K, M\}$ manifold before diagonalizing H_{cm} , L_{cm} and K^2 operators (the process in Section 3.2.1). D2 is the number of Slater determinants after selecting the correct eigenvalue of K and choosing the linear combinations that have the values $L_{CM} = 0$ and $H_{CM} = 1/2$ in the center-of-mass motion (the process in Section 3.2.2 is performed).

For instance, there are 5 Slater determinant at $K = 10$:

$$\begin{aligned}
 |\psi_1\rangle &= |0, 0\rangle|0, -1\rangle|0, -4\rangle|0, -5\rangle, \\
 |\psi_2\rangle &= |0, 0\rangle|0, -2\rangle|0, -3\rangle|0, -5\rangle, \\
 |\psi_3\rangle &= |0, -1\rangle|0, -2\rangle|0, -3\rangle|0, -4\rangle, \\
 |\psi_4\rangle &= |0, 0\rangle|0, -1\rangle|0, -2\rangle|0, -7\rangle, \\
 |\psi_5\rangle &= |0, 0\rangle|0, -1\rangle|0, -3\rangle|0, -6\rangle.
 \end{aligned} \tag{3.26}$$

The basis functions with $L_{cm} = 0$, $H_{cm} = 1/2$ and $K = 10$ are the linear combinations of the above five Slater determinants,

$$\begin{aligned}
 |\Psi_1\rangle &= 0.6727|\psi_1\rangle - 0.2212|\psi_2\rangle + 0.4946|\psi_3\rangle + 0.2760|\psi_4\rangle - 0.4216|\psi_5\rangle, \\
 |\Psi_2\rangle &= -0.2805|\psi_1\rangle - 0.3335|\psi_2\rangle + 0.7458|\psi_3\rangle - 0.2760|\psi_4\rangle + 0.4216|\psi_5\rangle.
 \end{aligned} \tag{3.27}$$

The next step is to diagonalize the Coulomb interaction at fixed hyperradius, that is, the hyperradius is treated as an adiabatic parameter (as described in Section 3.2.3). The hyperradius potential curves are plotted in Fig. 3.1.

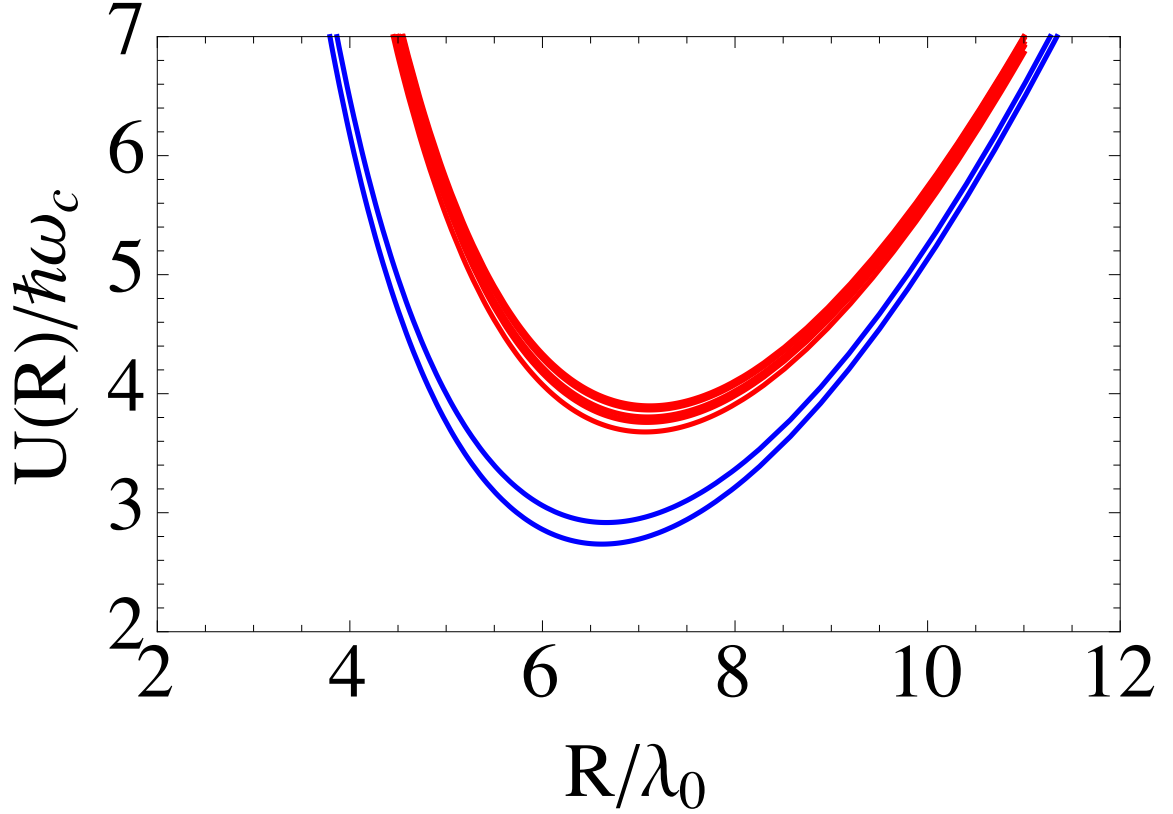


Fig. 3.1. Fig. 2 from Ref. [30]. Hyperradial potential curves for a four-electron system. The blue lines (lower branch) are hyperradial potentials for $K = -M = 10$, which correspond to the lowest Landau level. The red lines (upper branch) correspond to $K = -M + 2 = 12$. The energy gap between separate clusters is approximately equal to the cyclotron excitation, while the smaller splittings within each branch are due to Coulomb interactions. The relative strength of the Coulomb interaction, $\kappa = \frac{e^2}{4\pi\epsilon\lambda_0} \frac{1}{\hbar\omega_c}$, is set to be 1, which is the typical order for experiments in gallium arsenide.

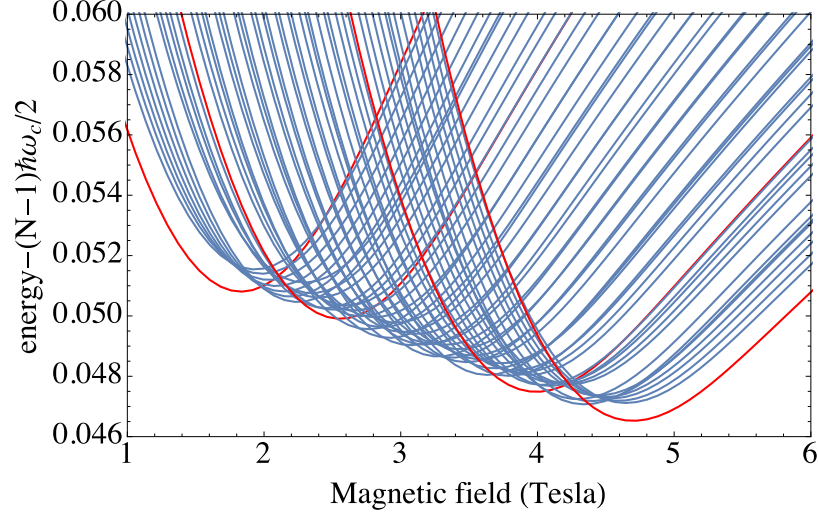


Fig. 3.2. Fig. 3 from Ref. [30]. The ground state energies of 8 particles in the lowest Landau level ($K = |M|$) at various K values as a function of the magnetic field, using experimental parameters matching a cold gallium arsenide system [65]. The magnetic field dependent zero-point energy has been subtracted for scale. The curves correspond to various K values ranging from $K = 28$ (filling factor $\nu = 1$) to $K = 84$ ($\nu = 1/3$). Curves for quantum Hall states at $\nu = 1, 2/3, 2/5$ and $1/3$ are marked as red lines from left to right respectively.

Fig. 3.2 shows an example of the calculation of a 8-particle system in the lowest Landau level ($K = |M|$). In the absence of coupling between different K manifolds, the ground state energies are calculated by first diagonalizing the Coulomb interaction within a hyperangular $\{K, M\}$ manifold then solving the hyperradial Schrödinger's equation numerically with a restricted maximum hyperradius.

3.3 Novel Excitations

In condensed matter and atomic physics alike, particle interactions can give rise to collective behaviors in many-body systems with dramatic and often unexpected properties [4, 66–68]. In no system are collective behaviors more central than in the fractional quantum Hall system, where the properties of low-energy quasi-particle excitations continue to drive new theoretical and experimental discoveries [5, 6, 10, 69, 70].

For example, among such low-energy excitations, one type of density oscillations known as the magnetoroton was described quite early in the description of the fractional quantum Hall effect [71,72]. However, collective excitations at higher energies, near the cyclotron frequency $\omega_c = eB/m$, are considerably less well explored: while the center-of-mass excitation, which is indistinguishable in frequency from the single particle excitation frequency ω_c by Kohn's theorem [73], is clearly predicted by theory, experiments in capacitance spectroscopy [74], optical emission spectroscopy [75], and high-intensity pulsed terahertz spectroscopy [76] have detected behaviors that defy the simple single-particle or Kohn's theorem predictions, indicating that the cyclotron frequency excitation regime exhibits interesting new physics. A variety of numerical treatments have been used to characterize quantum Hall systems [8,44,77–79], but isolating any specific excitation in the cyclotron energy regime from many of these models is daunting since the excitation spectrum is highly complicated.

However, the hyperspherical approach discussed in this chapter is particularly suitable for probing this type of excitations. Recasting the quantum Hall problem in the adiabatic hyperspherical representation [44, 79] highlights the existence of a unique type of vibrational mode [17] that may be directly measurable. This section implements the hyperspherical method and the numerical techniques developed in the previous sections to examine the origin and properties of a particular type of vibrational excitation observable in quantum Hall systems, which we call the hyperradial breathing mode. We will also discuss possible schemes for its measurement in experiments in both condensed matter and cold atom systems. The many-body quantum Hall Hamiltonian for N electrons confined to two-dimensions in a strong, perpendicular magnetic field in the symmetric gauge also describes a rotating two-dimensional gas of neutral atoms in a harmonic trap (or even non-rotating, see below), except for the form of the interactions [56]. This makes the latter an ideal system for comparing the effect of different interactions on the collective behaviors of the system.

3.3.1 Interacting Hyperspherical Forms

In the symmetric gauge, the relative coordinate interacting Hamiltonian can be rewritten in hyperspherical coordinates as

$$H_{\text{rel}} = -\frac{1}{2\mu} \nabla_{R,\Omega}^2 + \frac{\mu}{8} R^2 + \frac{1}{2} L_z^{\text{rel}} + \kappa C(\Omega) V(R), \quad (3.28)$$

where $\nabla_{R,\Omega}^2$ is the Laplacian in hyperspherical coordinates [55], $\mu = N^{-1/N_{\text{rel}}}$ is a dimensionless mass scaling factor, and $C(\Omega)$ is the hyperangular part of the interactions. κ is a dimensionless parameter that determines the interaction strength.

The last term in Eq. (3.28) represents the interactions in terms of the hyperspherical coordinates, with the lengths scaled by l_B for the system in question. For the condensed matter system, the interactions are simply Coulomb repulsive, but in two-dimensional cold atom systems, a variety of interactions can be implemented by different experimental choices.

The form of the hyperangular term $C(\Omega)$ depends on the form of the interactions and on the specific choices of Jacobi vectors and hyperspherical coordinates transformations, and $V(R)$ takes the simple forms $1/R$ for Coulomb interactions or $1/R^3$ for polarized dipole-dipole interactions.

As has been discussed in the previous sections in this chapter, in the absence of interactions, the quantum Hall Hamiltonian is exactly separable into a hyperradial and a hyperangular Hamiltonian. The solutions are products of hyperradial functions times hyperangular functions known as the hyperspherical harmonics from K-harmonic theory [80],

$$\Psi(R, \Omega) = R^{-N_{\text{rel}}+1/2} F_{n_R, K}^{(M)}(R) \Phi_{K, a}^{(M)}(\Omega). \quad (3.29)$$

However, in presence of interaction, such a separate solution is no longer strictly correct. Instead, the hyperangular channel functions parametrically depend on R :

$$\Psi(R, \Omega) = R^{-N_{\text{rel}}+1/2} \sum_{\chi} F_{E_{\chi}}^{(M)}(R) \Phi_{\chi}^{(M)}(R, \Omega), \quad (3.30)$$

where the channel functions, $\Phi_\chi^{(M)}(R, \boldsymbol{\Omega})$, labeled by χ , are orthonormal to each other for any given fixed hyperradius:

$$\int d\boldsymbol{\Omega} \Phi_\chi^{(M)*}(R, \boldsymbol{\Omega}) \Phi_{\chi'}^{(M)}(R, \boldsymbol{\Omega}) = \delta_{\chi\chi'}. \quad (3.31)$$

Treating the hyperradius R as an adiabatic parameter, the adiabatic Hamiltonian can be written as

$$H_{ad} = \frac{1}{2\mu R^2} \{ \hat{\mathbf{K}}^2 + (N_{rel} - 1/2)(N_{rel} - 3/2) \} + \frac{\mu}{8} R^2 + \frac{1}{2} M + \kappa \frac{C(\boldsymbol{\Omega})}{R}, \quad (3.32)$$

which is diagonalized for each fixed value of the hyperradius.

The procedure to diagonalize the adiabatic Hamiltonian and obtain the eigenstates is the following. First expand the channel functions $\Phi_\chi^{(M)}(R, \boldsymbol{\Omega})$ at a fixed hyperradius in terms of the anti-symmetrized hyperspherical harmonics,

$$\Phi_\chi^{(M)}(R, \boldsymbol{\Omega}) = \sum_{Ka} c_{Ka}(R) \Phi_{Ka}^{(M)}(\boldsymbol{\Omega}). \quad (3.33)$$

The matrix elements of the adiabatic Hamiltonian H_{ad} under this expansion are

$$\langle H_{ad} \rangle = U_K^{(M)}(R) \delta_{KK'} \delta_{aa'} + \kappa \frac{\langle K'a' | C(\boldsymbol{\Omega}) | Ka \rangle}{R}, \quad (3.34)$$

where the integrals indicated by the brackets are performed only over the hyperangles. The a 's label the anti-symmetrized hyperspherical harmonics within a given K manifold.

The eigenenergy of the above adiabatic Hamiltonian matrix determine a set of adiabatic potentials $U_\chi^{(M)}(R)$ through

$$H_{ad} \Phi_\chi^{(M)}(R, \boldsymbol{\Omega}) = U_\chi^{(M)}(R) \Phi_\chi^{(M)}(R, \boldsymbol{\Omega}). \quad (3.35)$$

Typical inter-particle interactions, such as the interactions which only depends on the relative distance between particles, do not break the degeneracy of the M manifold, i.e., M remains as a good quantum number. However, interactions do induce coupling between different K manifolds. In fact, it has been shown [17] to be a good approximation to neglect the coupling between different K manifolds and to

apply degenerate perturbation theory. The adiabatic Hamiltonian is then diagonalized within each K manifold, with restricted matrix elements $\langle Ka'|C(\Omega)|Ka\rangle$. The resulting eigenvalues $C^{(M)K\gamma}$ then determine a set of adiabatic potentials:

$$U_\chi^{(R)}(R) \approx \delta_{KK'}(U_K^{(M)}(R) + \kappa \frac{C^{(M)K\gamma}}{R}). \quad (3.36)$$

These potential curves enter the scaled Schrodinger equations which are to be solved, yielding the final ground state as well as the excitations.

3.3.2 Collective Excitations

We restrict our investigation to clusters of electric or magnetic dipoles aligned with the axis of rotation interacting purely via repulsive dipole-dipole interactions [51], which are among the class of interactions that can drive the formation of quantum Hall liquids [81–83]. Then the term κ in the interacting Hamiltonian Eq. (3.28) is the ratio of the interaction energy to the Landau-level separation: for Coulomb interactions, $\kappa = e^2/(4\pi\epsilon\lambda_0\hbar\omega_c)$; for dipole-dipole interactions, $\kappa = c_{dd}/(4\pi\lambda_0^3\hbar\omega)$, where $c_{dd} = \mu_0\mu_{mag}^2$ for polarized magnetic dipoles with magnetic moment μ_{mag} , and $c_{dd} = d^2/\epsilon_0$ for polarized electric dipoles with dipole moment d . The form of the hyperangular term $C(\Omega)$ depends on the form of the interactions and on the specific choices of Jacobi vectors and hyperspherical coordinates, and $V(R)$ takes the simple forms $1/R$ for Coulomb interactions or $1/R^3$ for polarized dipole-dipole interactions.

Implementing the procedure developed in the previous section, excitations in the hyperradial dimension can be extracted. These represent collective density excitations of the finite system, which we call the hyperradial breathing mode.

As a simple example, Fig. 3.3 shows the hyperradial curves and energies for the four-particle integer quantum Hall state ($M = 6$, $K = 6$, and $n_R = 0$) in GaAs and all excited states with $M = 6$ that are approximately $\hbar\omega_c$ higher in energy. We are interested in the lowest energy hyperradial excitation, the transition from $n_R = 0$ to $n_R = 1$ with energy (E_1E_0) for any given set of hyperangular quantum numbers, as is highlighted with the vertical (red) arrow in Fig. 3.3. It is a density excitation,

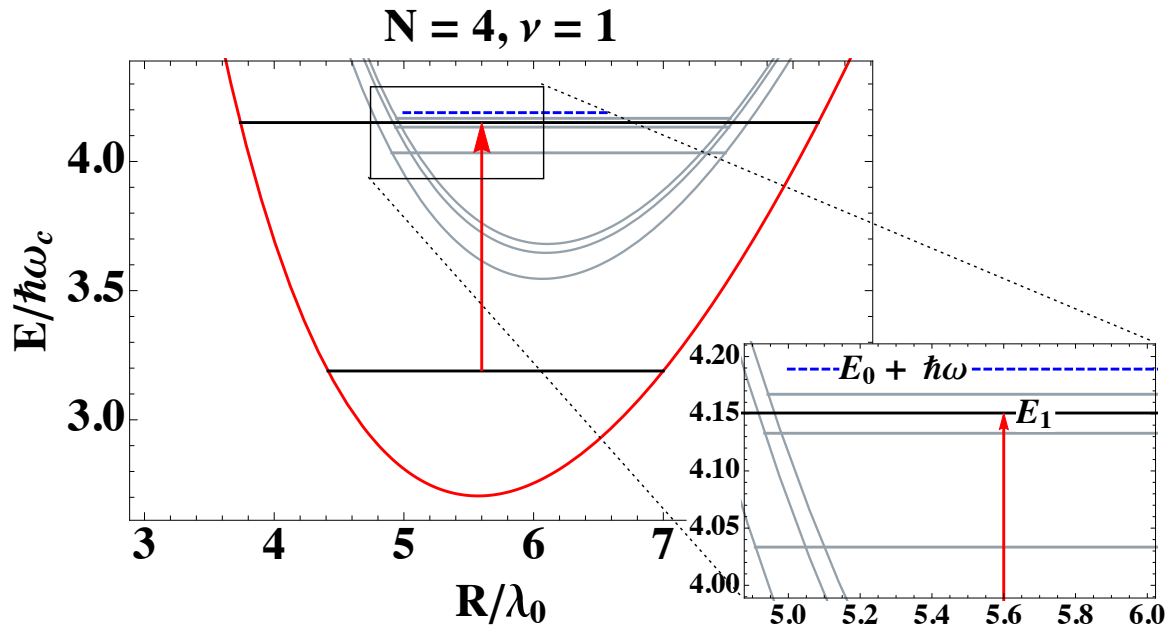


Fig. 3.3. Fig. 1 from Ref. [51]. Hyperradial potential curves and the hyperradial bound states for the four particle, $\nu = 1$ system. The ground state for $\nu = 1$ has hyperangular quantum numbers $K = 6, M = -6$ and $n_R = 0$, and is totally isolated. The hyperradial excitation takes the system from the $n_R = 0$ state with energy E_0 to the first hyperradially excited state with $n_R = 1$ and energy E_1 . The E_0 plus the cyclotron energy is shown as a (blue) dashed line for contrast. Other excited potential curves and their ground state energies with the same M with are shown in pale grey.

but unlike the magnetoroton, it is not a low-energy excitation within a Landau level, and it includes physics beyond the single mode approximation of a simple oscillator model [71, 72, 84]. Using more exact numerical techniques here constitutes including some level of Landau-level mixing in our approximation; our previous studies give bounds to the hyperangular contribution to Landau-level mixing, and indicate that hyperangular Landau-level mixing, or coupling between K manifolds, is weak for lowest Landau-level ground states and modest values of κ .

Figure 3.4 gives the energy separation between the ground state and the first hyperradial excited state for several important lowest Landau-level filling factors in the GaAs system (top) and the cold atom system (bottom) as a function of κ (left) and the number of particles (right). For Fig. 3.4(b), the values of κ used for each filling factor are taken from the experimental results of [85]. Since cold atom systems are hypothetically more tunable and currently lack an experimental paradigm, κ was set to 1 for all filling factors of the dipole-dipole interaction calculations shown in Fig. 3.4(d). We note that the hyperradial excitation energy $E_1 - E_0$ for Coulomb repulsion is smaller than $\hbar\omega_c$ for all tested systems, while the opposite is true for the dipole-dipole interacting system. In general, the vibrational mode excitation energy detuning from $\hbar\omega_c$ in both cases is largest when κ is large and when the filling factor is smallest, although this trend does not hold universally for Coulomb interactions, as there are a few exceptions [which are difficult to see in the scales of Fig. 3.4(b)]. Increasing the number of particles weakens the detuning in both cases as well, and this trend is stronger in the dipole-dipole interacting system, as can be seen in Fig. 3.5, which compares the two systems at filling factor $\nu = 1/3$ on equivalent scales.

We have not yet found a simple interpretation for the nonmonotonic N dependence of the energy shifts, but it is likely due to finite size effects. In the composite fermion (CF) picture, a N -electron Laughlin ground state consists of the N transformed CFs totally filling the lowest CF Landau levels (known in the CF picture as Lambda levels). The N -electron Jain states, in contrast, consist of $N/2 - 1$ CFs filling the lowest CF lambda level and $N/2 + 1$ CFs filling the second lambda level. As can

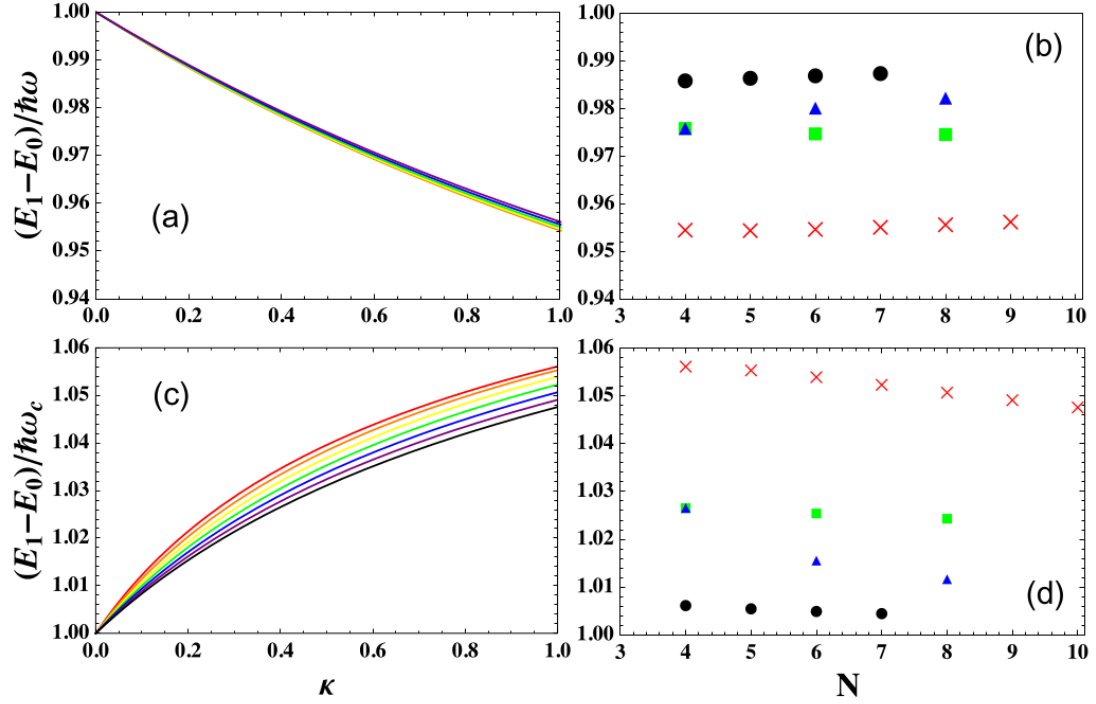


Fig. 3.4. Fig. 2 from Ref. [51]. (a) The hyperradial vibrational (HRV) mode excitation energies for Coulomb interactions as a function of κ for $N = 4, \dots, 9$ particles at $\nu = 1$ filling factor. From the lowest curve (red) with $N = 4$, the number of particles increases to $N = 9$ for the uppermost (black) curve. (b) The HRV energies for Coulomb interactions versus particle number for various filling factors [$\nu = 1$ (red crosses), $\nu = 2/3$ (green squares), $\nu = 2/5$ (blue triangles), and $\nu = 1/3$ (black circles)]. The values of κ are calculated from corresponding experimental magnetic fields in Tesla from [85]: $\nu = 1$ corresponds to 9T, $\nu = 2/3$ to 14T, $\nu = 2/5$ to 25T, and $\nu = 1/3$ to 29T. (c) The HRV excitation energies for dipole-dipole interactions as a function of κ . In this case the number of particles decreases from $N = 4$ downward to $N = 9$ on the plot. (d) The HRV energies for dipole-dipole interactions at $\kappa = 1$. The filling factors are labeled as in (b). For Coulomb interactions, the $\kappa = e^2/(4\pi\lambda_0\hbar\omega_c)$, and for dipole-dipole interactions, $\kappa = c_{dd}/(4\pi\lambda_0^3\hbar\omega_c)$, where c_{dd} is $\mu_0\mu_{mag}^2$ for polarized magnetic dipoles or d^2/ϵ_0 for polarized electric dipoles.

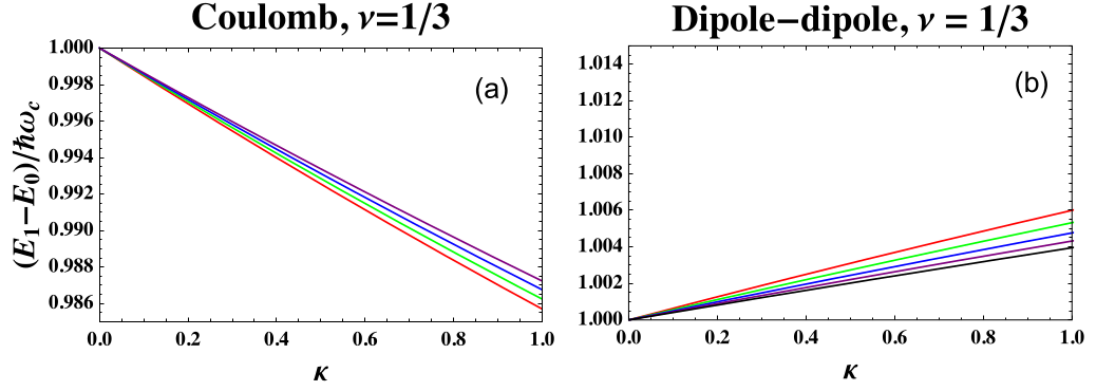


Fig. 3.5. Fig. 3 from Ref. [51]. The hyperradial vibrational modes versus κ for the $\nu = 1/3$ filling state for both (a) Coulomb, and (b) dipole-dipole interactions shown on the same scales relative to $\hbar\omega_c$. The detuning for the dipole-dipole interacting system exhibits stronger N dependence.

be seen from this picture, increasing the number of particles for a Laughlin system increases the Hilbert space size of a single lambda level at twice the rate as increasing the number of particles for a Jain system. As a result, the largest Jain systems we ran numerically are more affected by finite size effects than the largest Laughlin systems we ran. Access to more significant computing resources would allow the exploration of more structurally complicated few-body quantum Hall states in the lowest Landau level requiring more particles (e.g., the 4/11 state [86, 87]), which could establish whether the nonmonotonicity is uniquely due to few-body behaviors.

Experimentally, this hyperradial breathing mode cannot be excited through purely optical means because the laser field only operates on the center of mass for equal-mass, equal-charge particles, and should not induce transitions of the internal degrees of freedom of the system without additional terms in the Hamiltonian involving significant coupling between the center of mass and relative degrees of freedom (which we neglect in this work, but could include localized anisotropic features of the back-

ground, e.g., impurities or lattice defects). However, the transition could be induced by a time-dependent perturbation to the radial harmonic confinement of the form

$$V'(t) = a \cos \omega_0 t \sum_{i=1}^N r_i^2 = a \cos \omega_0 t \left(\frac{1}{N} r_{cm}^2 + \mu R^2 \right), \quad (3.37)$$

where a is the strength of the weak potential, r_i are the single-particle coordinates, and ω_0 is the hyperradial transition frequency. From the form of Eq. (3.37), it is clear that such a potential can perturbatively excite the center of mass or the hyperradial degrees of freedom, but the hyperradial excitation can be spectroscopically selected by the choice of frequency. For a two-dimensional electron gas, this oscillating potential could be achieved by weakly oscillating the perpendicular magnetic field at high frequencies, although the terahertz frequencies required for typical samples will be experimentally challenging to achieve, and detection will also prove difficult.

Measuring the hyperradial breathing modes should be more feasible in trapped cold atom or cold molecule systems interacting via repulsive dipole-dipole interactions, where the harmonic perturbation of Eq. (3.37) can be produced by flexing the trapping potential in a time-dependent manner. Collective modes have been previously observed directly in Bose-Einstein condensates [88] and degenerate Fermi gases, including in two dimensions [89], using trap-oscillating techniques in the absence of internal rotation as a tool to evaluate various internal properties of the gas.

Construction of a cold atom or cold molecule quantum Hall gas remains a significant experimental challenge, but the cold atom systems present a dramatic range of tunability which could be ideal for probing these vibrational modes. Using, for example, the magnetic dipole interactions of ^{161}Dy [90] and assuming a $\nu = 1$ filling factor, dipole trap with a planar trapping frequency of $\omega = 30$ kHz has κ of only 2.6×10^{-3} , and a detuning of only ≈ 22 Hz, but a much tighter trap could enhance the detuning, since κ varies with the square root of ω_c . Substituting magnetic dipolar atoms with cold electric-dipolar alkali molecules, which have intrinsic dipole moments of around 1 D, can also dramatically enhance the effect. For example, fermionic LiRb has an intrinsic dipole moment of around 4.1 D [91], so in a 15 kHz trap, $\kappa = 1.5$

and the detuning for the $N = 4$, $M = 6$ integer quantum Hall state is around 2 kHz. The greatest challenge in this experimental system will be the measurement of the energy, but there are several methods that might prove effective. For an array of quantum Hall droplets, photoassociation measurements in the spirit of [92, 93] may be sensitive enough to measure the few-body excitation energies. Alternately, it may be feasible to directly measure the total absorption of the perturbative light by the many droplets. If instead the successful quantum Hall experiment consists of a single droplet of only a few particles in a deep-well, optical tweezer, the excitation energy might be measured by Coulomb explosion imaging [94] or by a sensitive trap loss [95].

While most discussions of the quantum Hall effect for ultracold atoms have envisioned rotating traps, it should be pointed out that the spectra predicted here can be observed also for a nonrotating isotropic two-dimensional (2D) trap. This is because the difference in the Hamiltonian between a rotating versus a nonrotating trap is simply the presence of the constant term $\frac{1}{2}L_z^{rel}$ in Eq. (3.28), which is present only for a rotated trap in the rotating frame. But since L_z^{rel} is a conserved quantity for this system, the energy levels should be observable if the appropriate relative angular momentum modes are created for the number of atoms or molecules in the trap. For example, in a nonrotating 2D trap containing four identical, spin-polarized fermionic atoms, the Laughlin 1/3 state is the lowest energy eigenstate having relative angular momentum $|M| = 18$, and the breathing mode frequency predicted using the adiabatic hyperspherical approximation should be accurate. It is therefore an observable excitation in the Hilbert space even though it is not the M value of the ground state of the system as a whole.

To conclude this section, using the hyperspherical method we have established the existence of a hyperradial breathing mode in the quantum Hall system. This breathing mode energy is affected by the particle count, the strength and type of the interaction, and the filling factor. Although experimental realizations of this measurement face significant challenges, the modes should be experimentally excitable and measurable. For few-body systems, the presence of disorder will specifically af-

fect excitations located near the disorder center. Our model does not yet account for the possible effects of disorder, but it will likely enable coupling between different hyperangular states, including between states within different K manifolds because the disorder will likely break the rotational symmetry input in our model. Disorder in the atomic traps is unlikely to be a problem, but trap anharmonicity could similarly allow nonhyperradial excitations. We are unable to predict the strength of these effects in our model at this time. As a final speculation, we suggest that, while exciting in its own right as a new collective excitation in the system, this particular measurement could also be useful in establishing direct measurements of the effects of Landau-level mixing. Landau-level mixing refers to deviations from the idealized single-Landau-level approximation due to coupling between different Landau levels. While Landau-level mixing has been estimated through various methods [96–99], the effect is challenging to measure experimentally. In measuring the hyperradial excitation, deviations from the ideal hyperradial vibrational mode energies should be attributed to hyperangular coupling between Landau levels. Such a direct measurement of Landau-level mixing in the hyperangular picture would provide a test for these previous models of interlevel coupling effects in the quantum Hall system.

4. BULK-EDGE CORRESPONDENCE

The chapter temporarily moves away from the hyperspherical approach for solving the quantum Hall Hamiltonian problem. Instead of searching for the ground state and the excitations, the focus will be shifted to the properties of a given ground state, either the ideal model wavefunctions or the ground state of the realistic interactions. In particular, we will study the “bulk-edge correspondence” of the fractional quantum Hall ground states, which is a manifestation of the topological nature of the fractional quantum Hall effect.

Precisely speaking, we substantiate a complete picture of the bulk-edge correspondence conjecture [100]. By studying the eigenstates in the entanglement spectrum for both the ideal and realistic Coulomb ground states of the fractional quantum Hall system, it is verified that the eigenstates in the universal part of the entanglement spectrum purely lie in the Hilbert space of the edge excitations projected onto the physical Hilbert space of the subsystem itself. Hence, not only are the eigenlevels in the entanglement spectrum in one-to-one correspondence with the eigenenergies of an effective dynamical edge Hamiltonian, but all the eigenstates are confirmed to be the actual (projected) edge excitations of the subsystem. This result also reveals the possibility of extracting the full information of the edge excitations from the state of the subsystem reduced from a geometric cut of the pure ground state of the total system in topological phases.

We will first introduce the principle of “bulk-edge correspondence” and related concepts following the historical line of development in the field, and then present a detailed numerical study of this effect.

4.1 Topological Order

Landau symmetry breaking theory has been believed for a long time to describe all possible orders in materials. However, since the late 1980s, it was realized that there exist phases that do not fit into the classification of Landau symmetry breaking theory. The first theoretical example was the chiral spin state [101, 102], which was initially proposed to explain the high temperature superconductor [103]. This particular order of phase was named the “topological order” [104], motivated by the fact that the low energy excitations of the chiral spin liquid can be effectively described by a topological field theory [105]. It was later indicated by experiments that chiral spin states do not describe high temperature superconductors. However, the theory of topological order has been proven to be the correct theory for the quantum Hall states. Similar to the chiral spin states, quantum Hall states at different filling factors possess the same symmetry, while the transition between them is impossible without encountering a phase transition point, typically indicated by a singularity of a physical quantity.

Despite the theoretical importance, states with topological orders exhibit many interesting properties that allow for novel applications. For instance, the fractional statistics or the non-abelian statistics of quasi-particle excitations of a topologically ordered state can be used to realize topological fault-tolerant quantum computing [106–108], which is immune to decoherence induced by local perturbations; perfect conducting edge states also have potential device applications.

It is thus important to have a complete classification of topological orders. It is even more desirable to have a “order parameter” in analog to the Landau symmetry breaking theory. There are various ways to achieve this goal. For instance, at the early stage of the studies of the topological order, it was realized that the ground state degeneracy [109] is closely related to the topology of the manifold on which the system lives. Another prominent approach is to look at the entanglement present in the ground state of the system. This perspective is mostly motivated by the study of quantum information in the past decades. It is argued that ground states with

topological order usually exhibit “long-range entanglement” [110], which can not be destroyed by local operations, e.g., robust against local perturbations or preserved under entanglement re-normalization. In contrast, topologically trivial states, including topological insulators [111], only admit short-ranged entanglement.

The next section elaborates more about the entanglement aspect of the topological order.

4.2 Entanglement Entropy and Entanglement Spectrum

Bipartite entanglement of a pure quantum state can be uniquely characterized [112] by the entanglement entropy. For a quantum state (density matrix) ρ_{AB} on a composed Hilbert space $\mathcal{H}_{AB} = \mathcal{H}_A \otimes \mathcal{H}_B$, where A and B label two subsystems, the entanglement entropy is defined as the von Neumann entropy of one subsystem reduced density matrix:

$$S_A = -\text{tr}(\rho_A \ln \rho_A), \quad (4.1)$$

where

$$\rho_A = \text{tr}_B \rho_{AB} \quad (4.2)$$

is the state (reduced density matrix) for subsystem A . For pure joint quantum state $\rho_{AB} = |\psi_{AB}\rangle\langle\psi_{AB}|$, this quantity captures the entanglement between two of the subsystems, and is independent of the choice of the subsystem for computing von Neumann entropy, i.e., $S_A = S_B$.

For a many-body ground state, the two subsystems are usefully chosen as two systems with distinct spatial degree of freedom, i.e., partition of the total system in real space. Other partitions such as partitions in momentum space are also considered.

In the real space partition scenario, typical states in the Hilbert space, e.g., randomly chosen states, exhibit volume law scaling, i.e., the entanglement entropy of a subsystem is proportional to the volume of the subsystem itself. However, the ground state does not behave “typically”, in the sense that its entanglement entropy scales

linearly with the size of the boundary of the subsystem – the “area law”, which is a universal property of many-body systems.

In a state with topological order, besides the usual “area law” scaling, there emerges another sub-leading term:

$$S = \alpha L - \gamma + \dots \quad (4.3)$$

Here L is the area of the boundary between two subsystems; γ is a constant that is independent of the partition, namely, it is a global feature of entanglement in the ground state. γ is called the topological entanglement entropy and has become a widely recognized signature for topological orders. When the low energy physics of the system is described by a topological quantum field theory, γ is connected to the total quantum dimension D of the system, given by

$$\gamma = \ln D. \quad (4.4)$$

In the context of fractional quantum Hall states, the topological entanglement entropy is related to the filling factor ν :

$$\gamma = -\frac{1}{2} \ln \nu. \quad (4.5)$$

For the fermionic Laughlin state on the sphere geometry, the topological entanglement entropy has been computed numerically [113] and shown to match the theoretical prediction in Eq. (4.5). However, the calculations are performed for electrons on a sphere geometry, i.e., electrons are confined on a finite size sphere instead of on a two dimensional plane. In this case on the sphere geometry [113] the area law, i.e., the linear scaling to the subsystem boundary has not been observed.

In the inset of Fig. 2.6, a numerical simulation on the disk geometry (confined two-dimensional plane as a disk) for the entanglement entropy at various subsystem sizes has been shown. A clear linear scaling exists, up to the point when the subsystem size is half of the total system size, where the edge of the total system starts to affect the scaling law. However, in contrast to the slope of the linear fitting, the extracted sub-leading term, $-\gamma$, is very sensitive to the number of points used in the fitting:

fitting of the first 14 points gives $\gamma = 1.040$, while fitting of the first 3 points gives $\gamma = 0.473$ (The theoretical value is 0.549). This implies that the numerical topological entanglement entropy extracted from the data of a finite number of particles is still unreliable, despite the fact that the linear scaling is evident.

In practice, the entanglement entropy can be computed by performing a singular value decomposition (SVD) of the ground state:

$$|\Psi\rangle = \sum_i e^{-\xi_i/2} |\Psi\rangle_i^A \otimes |\Psi\rangle_i^B. \quad (4.6)$$

(The detailed procedure for performing the decomposition and the algorithms for implementing this decomposition to compute the entanglement spectrum of a fractional quantum Hall state will be given in Appendix E.) In fact the von Neumann entropy equals the classical Shannon entropy computed using the probabilities that appear in the SVD:

$$\begin{aligned} S &= - \sum_i e^{-\xi_i} \log e^{-\xi_i} \\ &= \sum_i e^{-\xi_i} \xi_i. \end{aligned} \quad (4.7)$$

In a recent work [114], Li and Haldane took one step forward. They argued that instead of computing the entropy associated with the SVD, which is just a single number, one can gain more information by looking at the whole spectrum of the probability, or alternatively the spectrum of ξ 's in the SVD. Since the reduced density matrix of subsystem A , according to the SVD in Eq. (4.6), can be written as

$$\rho_A = \sum_i e^{-\xi_i} |\Psi\rangle_i^A \langle \Psi|_i^A. \quad (4.8)$$

It is recognized that ξ_i can be viewed as nothing else but the eigenvalues of an effective Hamiltonian \tilde{H}_A of the form:

$$\rho_A \equiv e^{-\tilde{H}_A}, \quad (4.9)$$

a Gibbs ensemble at temperature $\beta = 1$. Here we use the tilde symbol to indicate that the effective Hamiltonian is distinct from the real Hamiltonian of the subsystem A . The spectrum of the effective Hamiltonian, denoted the set of quasi-energies ξ_i , are named the entanglement spectrum.

However, though not a real Hamiltonian, \tilde{H}_A was shown to be intimately related to the edge physics of the subsystem. Take as an example the ideal fractional quantum Hall states (model wavefunctions such as the Laughlin wavefunction at $1/3$ filling), which is also the case considered in the original work of Li and Haldane. In this case, the particle number and the total angular momentum are still good quantum numbers. Namely, the eigenstates appearing in the reduced density matrix, Eq. (4.8) are also eigenstates of the particle number operator and the total angular momentum operator for the subsystem A . We can then plot the spectrum separately for sectors with different particle number and angular momentum. Interestingly enough, the number of energy levels in the entanglement spectrum for each angular momentum sector has been demonstrated [114] to equal the number of edge excitations (edge states) with the corresponding angular momentum of a quantum Hall ground state at the same filling fraction. This counting structure of the entanglement spectrum is thus connected with the bulk of the system (reduced density matrix in the bulk computed from the ground state of the total system) and the edge physics (number of edge modes).

The counting structure of the entanglement spectrum also exhibits universality: When computed for the realistic numerically computed ground state for a fixed particle number and angular momentum instead of the ideal model wavefunctions, e.g., ground state of the quantum Hall system of electrons under Coulomb interaction, the entanglement spectrum splits into two parts: one universal part that has the same counting structure and similar distribution as the entanglement spectrum for the ideal model wavefunctions, one generic part that has much higher quasi-energies than the universal part.

The generic part and the universal part of the entanglement spectrum are separated by a gap which remains finite in the thermodynamic limit. This is a rather interesting effect. In contrast, it has been known that the difference between the ideal and realistic ground state wavefunctions, gauged in terms of their overlaps, is

not preserved in the thermodynamic limit. The statement holds, even though the model wavefunctions have very high overlaps with realistic ones for few particles.

4.3 Bulk-Edge Correspondence

Both the entanglement entropy and the counting structure of the entanglement spectrum can be naturally interpreted if a relation between the bulk and the physical edge of the subsystem is established. This relation, termed the bulk-edge correspondence [115–117], states that the entanglement Hamiltonian corresponds to an effective dynamical local Hamiltonian acting on a 1-D edge, which represents the boundary of the system.

At first glance, this may seem to be an empty statement. As has been discussed in the previous sections, the entanglement spectrum is the spectrum of an effective Hamiltonian given by Eq. (4.9). In principle one can always cook up an operator acting on a 1-D degree of freedom, whose matrix representation matches precisely this effective Hamiltonian, and call this operator the effective Hamiltonian for a 1-D system. However, one crucial feature that has to be fulfilled is the local structure: Such an effective 1-D Hamiltonian must be “local” in regard to the degree of freedoms it is acting on. In Ref. [117], an effective edge Hamiltonian that respects both locality and conformal symmetry has been constructed to model the entanglement spectrum of the Laughlin state at $1/3$ filling. It has been shown that the entanglement spectrum of the 6-particle sector of the 12-particle total system can be fitted very well to such an effective edge Hamiltonian up to only the second order (only 3 free fitting parameters involved).

The bulk-edge correspondence, originally sketched in the early work of entanglement entropy [118], has been extensively studied in various fields [119–124]. This correspondence emerged in part from general arguments based purely on the topological properties of the system and on the standard renormalization-group method [115], in part from observations of geometric aspects and the Lorentz invariance of the

emergent effective theory [116], and in part through study of model wavefunctions specific to the quantum Hall system constructed from conformal blocks [117]. These arguments are only valid provided certain assumptions hold in the thermodynamic limit.

In the present work, we argue that a complete picture of the bulk-edge correspondence should consist of two pieces. One is that the eigenvalues ξ_i are in one to one correspondence with the eigenvalues of an effective edge Hamiltonian. The other is that the universal eigenstates $|\Psi_i^A\rangle$ that appear in the bulk density matrix (See Fig. 4.1 for an illustration of the universal levels) are all real edge states of the subsystem. To be precise, the universal levels are those appearing in the entanglement spectrum of the ideal model wavefunctions, as well as the part of the spectrum having similar structures for the case of generic interactions. By comparing the entanglement spectrum eigenstates with the actual edge excitations, we are able to identify the universal branch of the spectrum (See Fig. 4.1 for an example). For the first part of the bulk-edge correspondence in the quantum Hall system, the only direct numerical evidence was provided in Ref. [117], where the spectrum of a perturbative local Hamiltonian of an edge system described by a conformal field theory was computed and shown to match quite well the entanglement spectrum obtained for a real space partition of the total system.

Since an effective edge theory usually describes the degrees of freedom that are distinct from those in the original bulk system, direct comparison of their eigenstates is much harder than comparing their eigenenergies. Thus, typical studies of the entanglement spectrum usually focus on the counting structure of the eigenlevels. In the present work, by analyzing the detailed information of the entanglement spectrum eigenstates, we complete the verification of the missing piece of the bulk-edge correspondence for both the model wavefunction and the realistic ground state of Coulomb interactions. The system studied here consists of a few spinless fermions in the lowest Landau level on a two-dimensional disk. In this work, system partitions are restricted to the subsets of the single particle magnetic orbitals in the symmetric

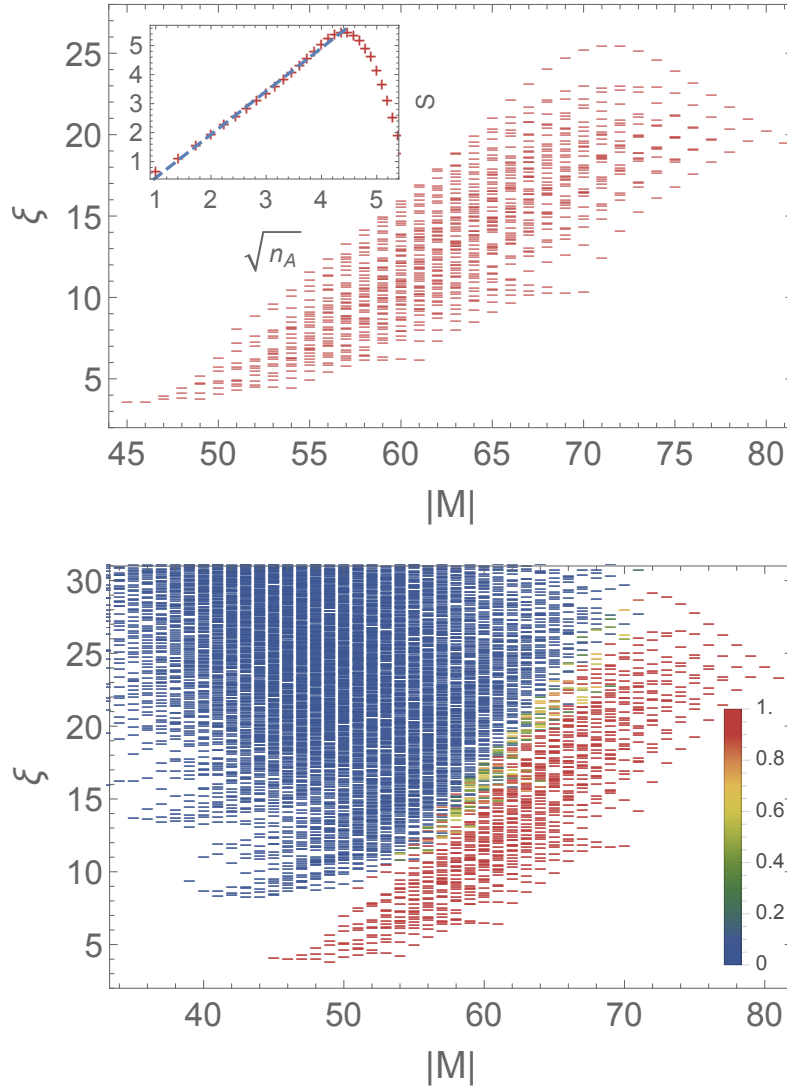


Fig. 4.1. Fig. 1 from Ref. [100]. Entanglement spectrum of the 17-orbital subsystem at the 6-particle sector. The total system of 12 particles in 34 total orbitals is prepared in (Upper) the ideal Laughlin state and (Lower) the realistic Coulomb interaction ground state. The color of the pseudo-energy levels indicate the overlaps between the corresponding entanglement spectrum eigenstates and the edge states of the subsystem. Inset: Entanglement entropy v.s. the square root of the number of orbitals (n_A) in subsystem A , which is proportional to the length of the boundary. The blue dashed line is our fit to the first 17 points, which are in the linear region away from the edge of the total system.

gauge (with unnormalized analytic wavefunction $z^{|m|}e^{-|z|^2/4}$, where $z = x - iy$ is the two dimensional complex coordinate and $m = 0, -1, -2, \dots$ is the angular momentum quantum number). In principle, the orbital cut is a partition in momentum space and is fundamentally nonlocal. However, in the lowest Landau level, these single particle orbitals have localized ring shapes with narrow width in the order of the magnetic length. Thus in many cases the orbital partition mimics approximately the real space partition and provides valuable information about the system.

It is also worthwhile to mention that another commonly used scheme, based on a cut of particle number [113, 125, 126], has usually been adopted for the study of quasi-hole excitations. In some particular model states, the level counting in the orbital entanglement spectrum and the one in the particle entanglement spectrum, which correspond to quasi-hole excitations in the bulk, were shown [127] to be ultimately connected. This relation, also termed “bulk-edge correspondence”, is not to be confused with the one we are considering in the present work.

In the subsystem, the particle number and total angular momentum are still good quantum numbers; Thus, the reduced density matrix of a subsystem contains distinct sectors which do not couple with each other. As an illustration, Fig. 4.1 compares the standard entanglement spectrum for the ideal Laughlin state with that of the realistic Coulomb ground state of 12 particles in the lowest Landau level. For entanglement spectra of the quantum Hall states in other geometry and partition schemes, see also Refs. [125, 126, 128–131]. The subsystem studied in this work involves the inner most $N/2$ -orbitals (with N the even number of total orbitals), which is the largest system that is sufficiently far away from the edge of the total system, in the sense that it is still in the linear region of the entanglement entropy (See the inset in Fig. 4.1). In this region, edge effects are supposed to be removed as much as possible. By analyzing the fraction of each eigenstate that resides in the Hilbert space of edge modes (by the procedure explained in the following), we are able to identify all the universal levels apart from the generic levels in the case of Coulomb interactions. It is observed that the universal and generic parts barely mix with each other, although at larger angular

momenta they start to mix, in contrast to the low angular momenta, where there is a finite gap between them.

4.3.1 Model Edge States

To prove the bulk-edge correspondence, on the “edge” part, we use the well-known series of model wavefunctions [132] for the (neutral) edge excitations of the Laughlin ground state. These analytic model wavefunctions are generated by the power sum symmetric polynomials $s_n = \sum_i z_i^n$, $n = 1, 2, 3, \dots$. To build an edge mode with angular momentum ΔM (this is the additional angular momentum carried by the edge mode beyond the ground state angular momentum), one generates an integer partition $|\Delta M| = \sum_i n_i$, where n_i are positive integers. The corresponding (unnormalized) edge state is constructed as the product of the Laughlin wavefunction and a symmetric polynomial:

$$\Psi_{edge} = \prod_i s_{n_i} \prod_{i < j} (z_i - z_j)^{1/\nu} \prod_i e^{-\frac{|z_i|^2}{4}}, \quad (4.10)$$

where ν is the filling factor. In general $1/\nu$ takes arbitrary odd integer values, while in the following numerical study we focus on $\nu = 1/3$ only. For a given ΔM , the number of different modes is thus the number of integer partitions of $|\Delta M|$. These states are the only zero energy states for the case of the Haldane V_1 pseudo-potential in the lowest Landau level, and they describe the gapless edge excitations of the Laughlin ground state. In the thermodynamic limit, the Hilbert space of the edge modes generated by the order- n power sum polynomials is identical to that generated by the U(1) Kac-Moody algebra [132–134] in a macroscopic theory of the edge physics. However, for finite size systems, when the orders of the symmetric polynomials become larger than the number of particles, these states are no longer linearly independent. In fact, the number of linearly independent symmetric polynomials of order n is the number of partitions of n into at most N parts, where N is the number of particles and the number of variables in the polynomial. Denote this restricted partition as $P(n, N)$. For each such integer partition $n = \sum_i^N n_i$, one alternative way to construct

the edge state is to use the corresponding order- n monomial symmetric polynomial $s_n = \sum_p (\prod_i z_i^{n_i})$, where the summation is taken over all permutations of z_i 's such that the polynomial is symmetrized. This leads to a correction of the number of edge modes for finite size systems compared with the macroscopic theory for systems in the thermodynamical limit.

Another finite size effect arises when comparing the edge modes with the eigenstates in the entanglement spectrum. That is, the ideal edge modes might involve single particle orbitals that are outside the region of the subsystem under consideration. These additional degrees of freedom need to be traced out in formatting the appropriate Hilbert space of the subsystem [117]. Precisely speaking, the Fock space spanned by the free edge states are projected onto a subspace involving only orbitals that are resident in the subsystem. This inevitable projection procedure was also discussed in Ref. [117] for the case the real space partitions. In this manner, the projections of the original linearly independent edge modes might become linearly dependent, such that the projected Fock space could have a smaller dimension than the original Fock space of the free edge states. For illustration, Table 4.1 lists the number of free edge modes, the number of independent projected edge modes, and the number of observed energy levels in the entanglement spectrum for the 5- and 4-particle sectors. The observed level counting in the primary 5-particle sector of the entanglement spectrum matches precisely the reduced dimension of edge modes Hilbert space at every angular momentum sector. In the large particle number limit, the restricted integer partition reduces to the regular integer partition. This is in agreement with the original conjecture for the counting structure of the entanglement spectrum in Ref. [135].

To prove that the universal part of the entanglement spectrum is indeed spanned by the edge modes, we compute the probability for each eigenstate in the entanglement spectrum to reside in this space. For a given eigenstate ψ of the entanglement spectrum, the projection probability is defined as

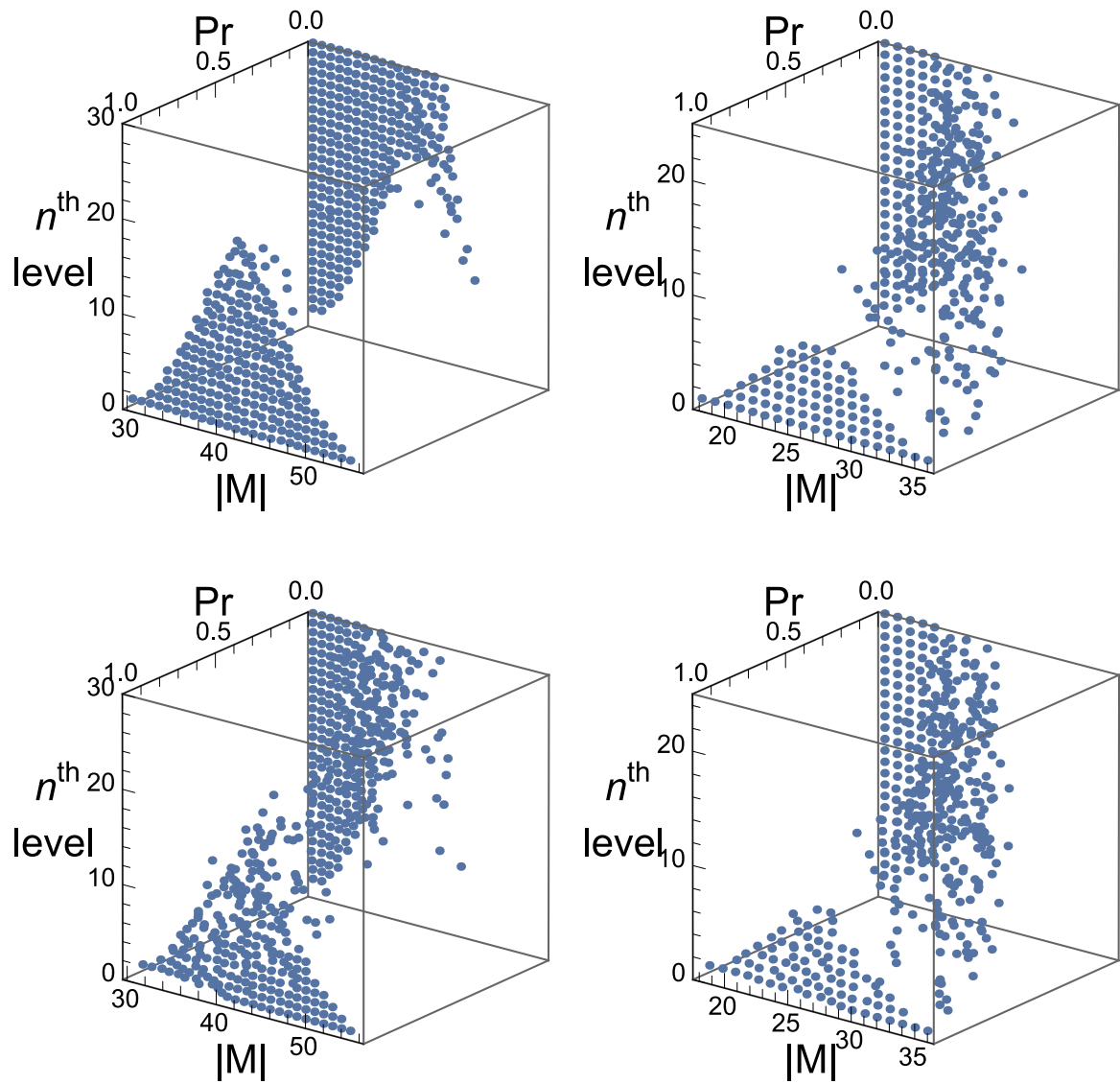


Fig. 4.2. Fig. 2 from Ref. [100]. The projection probabilities for the whole entanglement spectrum of the 5-particle sector (left) and the 4-particle sector (right) for the case of Coulomb ground state. The cases of both ideal edge states (upper) and realistic edge states of Coulomb interaction are examined.

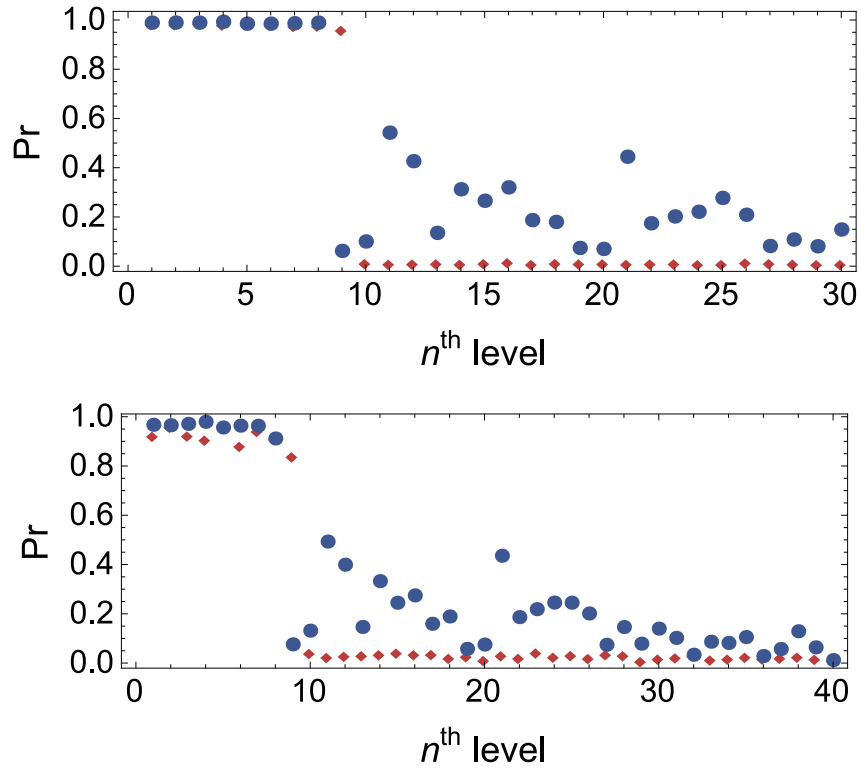


Fig. 4.3. Fig. 3 from Ref. [100]. Typical patterns for the projection probabilities. Red squares represent the probabilities for 5 particles at $\Delta M = 6$ ($|M| = 36$). Blue dots correspond to the 4-particle sector at $\Delta M = 8$ ($|M| = 26$). Projection probabilities are computed using (a) the model edge states for the Laughlin case and (b) the real edge states for Coulomb interactions.

Table 4.1.

Table I from Ref. [100]. The number of edge modes at various angular momentum ΔM in the 14-orbital subsystem. The total system has 10 particles occupying 28 orbitals. Upper and lower tables correspond to five and four particles, respectively. P is the number of free edge modes, i.e., the number of restricted integer partitions. D_p represents the dimension of the Hilbert space of projected edge modes; D_m labels the observed multiplicity of levels in the entanglement spectrum.

$ \Delta M $	0	1	2	3	4	5	6	7	8	9	10	11	12	13	14	15	...
$P(\Delta M , 5)$	1	1	2	3	5	7	10	13	18	23	30	37	47	57	70	84	...
D_p	1	1	2	3	5	7	9	11	14	16	18	19	20	20	19	18	...
D_m	1	1	2	3	5	7	9	11	14	16	18	19	20	20	19	18	...

$ \Delta M $	0	1	2	3	4	5	6	7	8	9	10	11	12	13	14	15	...
$P(\Delta M , 4)$	1	1	2	3	5	6	9	11	15	18	23	27	34	39	47	54	...
D_p	1	1	2	3	5	6	9	11	14	16	19	20	23	23	24	23	...
D_m	1	1	2	3	4	5	7	7	8	8	8	7	7	5	4	3	...

$$Pr(\psi) = |\hat{P}\psi|^2, \quad (4.11)$$

where \hat{P} is the projection operator to the Hilbert space of projected edge modes.

4.3.2 Numerical Results

We are able to compute the entanglement spectrum for both ideal Laughlin state and Coulomb ground state, and the corresponding projection probability defined in previous section, for up to 12-particles using exact diagonalization within the lowest Landau level. The data are presented in Fig. 1, which confirms that the eigenstates in the universal entanglement spectrum clearly stand out with a near unity overlap

with subsystem edge modes. In the following we illustrate more details with the 10-particle system.

For the ideal Laughlin wavefunction, it is confirmed that all the eigenstates in the entanglement spectrum have unity projection probabilities in the Hilbert space of the projected edge states.

For the case of Coulomb ground state, both the ideal edge states and the real edge modes of the subsystem are used to analyze the projection probability Eq. (4.11). The real edge modes are computed from the Coulomb interaction at the corresponding angular momenta with open boundary condition (without performing single particle orbital cut). In the thermodynamic limit, they are supposed to be low-lying modes describing the gapless edge excitations. However, in few-body calculations, there are usually no clear gaps in the spectrum separating the edge modes and the bulk excitations. In this case, we identify each edge state with the aid of high (~ 0.97) projection probabilities onto the Hilbert space of the ideal edge wavefunctions Eq. (4.10). These probabilities scale with the system size in the same way as the overlap between the Laughlin model state and the Coulomb ground state. It is known that the latter overlap does not survive in the thermodynamic limit. However, this is not a problem in this case since the edge states would stand out as gapless modes in the spectrum. For the purpose of the few-body calculations in the present work, high overlaps allow us to singles out the right number of edge states, while all other eigenstates of the Coulomb Hamiltonian have sufficiently small projection probabilities (~ 0.01) onto the Hilbert space of the model edge states.

Fig. 4.2 and Fig. 4.3 show the projection probability patterns. Both the primary 5-particle sector and the sector with particle number offset (4-particle sector in this case) show clear high probability plateaus for the universal levels in the entanglement spectrum. In the 4-particle sector, since the number of universal levels is smaller than the dimension of the projected edge modes (as was shown in Table 4.1), the generic levels also have fluctuating non-zero probabilities, in contrast to 5-particle

sector, where all the generic levels have nearly zero projection probabilities. They are nevertheless clearly separated from the universal part.

In the primary sector, since all universal eigenstates in the entanglement spectrum have nearly identity probabilities in the corresponding Hilbert space of projected edge modes, it is concluded that the information of all edge excitations is hidden in the pure ground state of the total system, which can be extracted from the bulk state of the subsystem. This can be viewed as a complementary effect to a similar result in Ref. [126], where it is observed that the primary sector of the entanglement spectrum under particle partition spans the entire space of quasi-hole excitations of the subsystem.

To further firm up the evidence of the bulk-edge correspondence, we present in Fig. 4.4 the actual energy spectrum of 5 particles under Haldane V_1 interaction with and without boundary conditions. The degenerate zero-energy states for the latter are model edge states. If we did not use the mechanism of projecting the edge states of the subsystem with open boundaries, the nondegenerate low-lying states of the subsystem alone would have been inadequate to explain all the observed universal levels in the entanglement spectrum (Fig. 4.1).

To conclude this section, we have shown that the universal part of the subsystem reduced density matrix, by orbital partition, of the fractional quantum Hall state lies in the Hilbert space of edge modes of the subsystem itself, hence completing the picture of the bulk-edge correspondence conjecture. This result also reveals the possibility of extracting edge excitations from the state of the subsystem reduced by geometric cut of the pure ground state of the total system in topological phases. In the future, it will be informative to apply this method to other systems in topological phases.

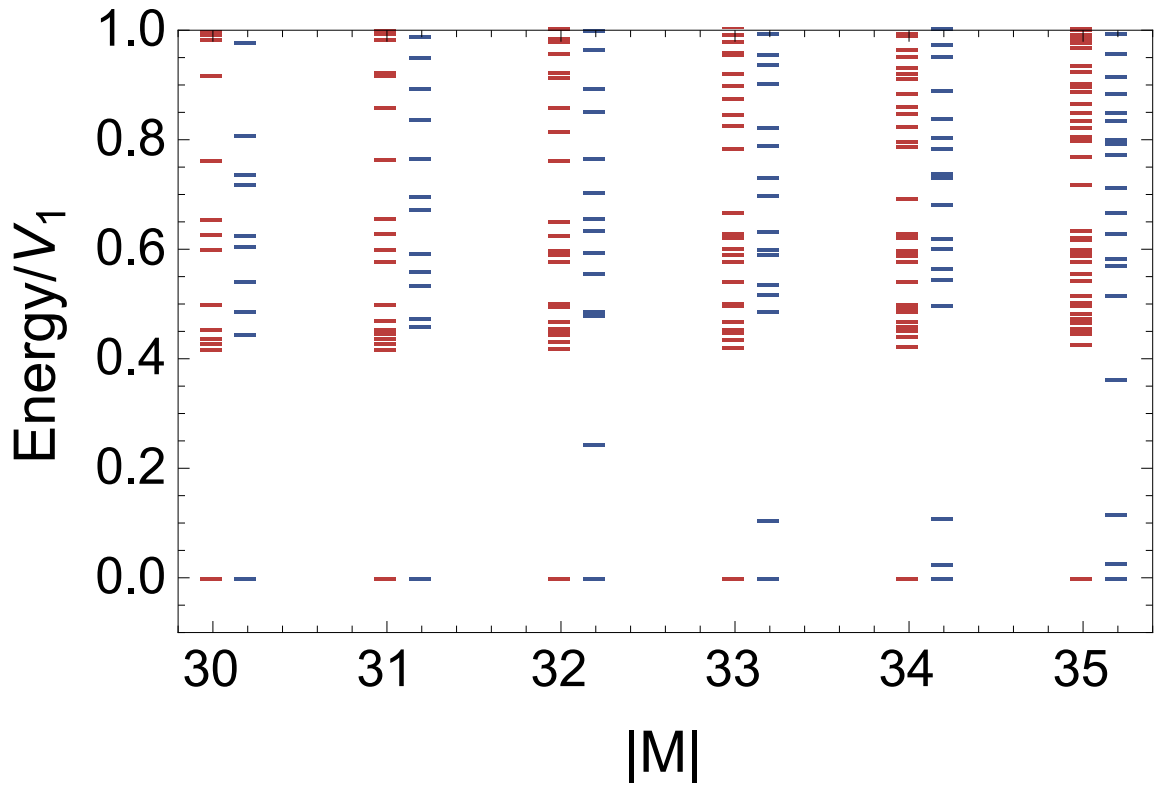


Fig. 4.4. Fig. 4 from Ref. [100]. The spectrum of 5 particles under the Haldane V_1 pseudo-potential with an open boundary condition (red levels) and with the same boundary condition as the 14-orbital subsystem (blue levels). The blue levels are shifted slightly to the right from their corresponding angular momenta. For the case of an open boundary condition, the degeneracies of the ground states are 1, 1, 2, 3, 5, 7, which are identical to the number of the ideal edge states.

5. SUMMARY AND OUTLOOK

To summarize, two achievements have been made in this dissertation. On the one hand, numerical techniques have been developed to fully utilize the framework of the hyperspherical approach to the fractional quantum Hall effect. The hyperspherical method is well developed and widely appreciated in the studies of few-body phenomena. Adopting this method to the context of the fractional quantum Hall effect provides an alternative perspective, which has advantages complementary to previous conventional treatments. It is in particular suitable to study the few-body collective behaviors of the fractional quantum Hall excitations, as has been demonstrated in the prediction of the collective hyperradial breathing mode. This unique type of vibrational mode might be directly measurable in the near future. The hyperspherical method has not seen widespread use in condensed matter physics, however, with the continued interest in realizing the fractional quantum Hall effect in the few-body community and the rapidly developing experimental techniques in highly controlled atomic systems, we expect to witness active applications of this method.

On the other hand, we have studied the principle of bulk-edge correspondence in the finite size quantum Hall states. This principle is universal for matter phases with topological orders. It offers a unified explanation for the topological entanglement entropy and the structure of the entanglement spectrum, e.g., the spectrum generated by the reduced density matrix of a subsystem in the bulk. Previous studies on the bulk-edge correspondence focused only on the energy level distributions of the entanglement spectrum. As has been demonstrated in this work, the eigenstates associated with the entanglement spectrum reveal more information for the state of entire system under consideration. This method could be directly applied to other systems with topological orders. It also provides a way to extract the edge modes purely from the bulk state induced from the global ground state wavefunction. This

is especially useful when the edge excitations are hard to compute directly. The discussion of the state of the reduced density matrix of the bulk subsystem also brings up many interesting directions to explore. For instance, once the connection between the state of the reduced bulk system and an effective edge system has been made, it might be possible to define an effective bulk temperature, even though the global ground state is in absolutely zero.

REFERENCES

REFERENCES

- [1] R. Clark, J. Mallett, S. Haynes, J. Harris, and C. Foxon, “Experimental determination of fractional charge e/q for quasiparticle excitations in the fractional quantum hall effect,” *Physical Review Letters*, vol. 60, no. 17, p. 1747, 1988.
- [2] R. De-Picciotto, M. Reznikov, M. Heiblum, V. Umansky, G. Bunin, and D. Mahalu, “Direct observation of a fractional charge,” *Physica B: Condensed Matter*, vol. 249, pp. 395–400, 1998.
- [3] K. v. Klitzing, G. Dorda, and M. Pepper, “New method for high-accuracy determination of the fine-structure constant based on quantized hall resistance,” *Physical Review Letters*, vol. 45, no. 6, p. 494, 1980.
- [4] D. C. Tsui, H. L. Stormer, and A. C. Gossard, “Two-dimensional magnetotransport in the extreme quantum limit,” *Physical Review Letters*, vol. 48, no. 22, p. 1559, 1982.
- [5] R. B. Laughlin, “Anomalous quantum hall effect: an incompressible quantum fluid with fractionally charged excitations,” *Physical Review Letters*, vol. 50, no. 18, p. 1395, 1983.
- [6] J. K. Jain, “Composite-fermion approach for the fractional quantum hall effect,” *Physical Review Letters*, vol. 63, no. 2, p. 199, 1989.
- [7] F. Haldane, “Fractional quantization of the hall effect: a hierarchy of incompressible quantum fluid states,” *Physical Review Letters*, vol. 51, no. 7, p. 605, 1983.
- [8] F. Haldane and E. Rezayi, “Finite-size studies of the incompressible state of the fractionally quantized hall effect and its excitations,” *Physical review letters*, vol. 54, no. 3, p. 237, 1985.
- [9] B. I. Halperin, “Statistics of quasiparticles and the hierarchy of fractional quantized hall states,” *Physical Review Letters*, vol. 52, no. 18, p. 1583, 1984.
- [10] G. Moore and N. Read, “Nonabelions in the fractional quantum hall effect,” *Nuclear Physics B*, vol. 360, no. 2-3, pp. 362–396, 1991.
- [11] N. Read and E. Rezayi, “Beyond paired quantum hall states: Parafermions and incompressible states in the first excited landau level,” *Physical Review B*, vol. 59, no. 12, p. 8084, 1999.
- [12] S. Girvin and R. Prange, “The quantum hall effect,” 1987.
- [13] B. A. Bernevig and F. Haldane, “Clustering properties and model wave functions for non-abelian fractional quantum hall quasielectrons,” *Physical Review Letters*, vol. 102, no. 6, p. 066802, 2009.

- [14] J. K. Jain, “The composite fermion: a quantum particle and its quantum fluids,” *Physics Today*, vol. 53, no. 4, pp. 39–45, 2000.
- [15] B. I. Halperin, “Quantized hall conductance, current-carrying edge states, and the existence of extended states in a two-dimensional disordered potential,” *Physical Review B*, vol. 25, no. 4, p. 2185, 1982.
- [16] B. A. Bernevig and F. Haldane, “Model fractional quantum hall states and jack polynomials,” *Physical Review Letters*, vol. 100, no. 24, p. 246802, 2008.
- [17] K. Daily, R. Wooten, and C. H. Greene, “Hyperspherical theory of the quantum hall effect: The role of exceptional degeneracy,” *Physical Review B*, vol. 92, no. 12, p. 125427, 2015.
- [18] J. Macek, “Properties of autoionizing states of he,” *Journal of Physics B: Atomic and Molecular Physics*, vol. 1, no. 5, p. 831, 1968.
- [19] C. H. Greene, “Universal insights from few-body land,” *Physics Today*, vol. 63, no. 3, pp. 40–45, 2010.
- [20] S. T. Rittenhouse, J. von Stecher, J. Dincao, N. P. Mehta, and C. H. Greene, “The hyperspherical four-fermion problem,” *Journal of Physics B: Atomic, Molecular and Optical Physics*, vol. 44, no. 17, p. 172001, 2011.
- [21] E. Nielsen and J. Macek, “Low-energy recombination of identical bosons by three-body collisions,” *Physical Review Letters*, vol. 83, no. 8, p. 1566, 1999.
- [22] M. Gattobigio, A. Kievsky, and M. Viviani, “Energy spectra of small bosonic clusters having a large two-body scattering length,” *Physical Review A*, vol. 86, no. 4, p. 042513, 2012.
- [23] C. D. Lin, “Hyperspherical coordinate approach to atomic and other coulombic three-body systems,” *Physics Reports*, vol. 257, no. 1, pp. 1–83, 1995.
- [24] N. Regnault and T. Jolicoeur, “Quantum hall fractions in rotating bose-einstein condensates,” *Physical Review Letters*, vol. 91, no. 3, p. 030402, 2003.
- [25] M. Roncaglia, M. Rizzi, and J. Dalibard, “From rotating atomic rings to quantum hall states,” *Scientific Reports*, vol. 1, p. 43, 2011.
- [26] M. Baranov, K. Osterloh, and M. Lewenstein, “Fractional quantum hall states in ultracold rapidly rotating dipolar fermi gases,” *Physical Review Letters*, vol. 94, no. 7, p. 070404, 2005.
- [27] V. Schweikhard, I. Coddington, P. Engels, V. Mogendorff, and E. A. Cornell, “Rapidly rotating bose-einstein condensates in and near the lowest landau level,” *Physical Review Letters*, vol. 92, no. 4, p. 040404, 2004.
- [28] A. S. Sørensen, E. Demler, and M. D. Lukin, “Fractional quantum hall states of atoms in optical lattices,” *Physical Review Letters*, vol. 94, no. 8, p. 086803, 2005.
- [29] J. K. Jain, *Composite fermions*. Cambridge University Press, 2007.

- [30] B. Yan, R. E. Wooten, K. M. Daily, and C. H. Greene, “Hyperspherical Slater determinant approach to few-body fractional quantum hall states,” *Annals of Physics*, vol. 380, pp. 188–205, 2017.
- [31] “Landau levels.” <http://hitoshi.berkeley.edu/221a/landau.pdf>, 2005.
- [32] X.-G. Wen and Z. Wang, “Classification of symmetric polynomials of infinite variables: construction of abelian and non-abelian quantum hall states,” *Physical Review B*, vol. 77, no. 23, p. 235108, 2008.
- [33] M. Romagny, “The fundamental theorem of alternating functions.” 2005.
- [34] S. H. Simon, E. Rezayi, and N. R. Cooper, “Pseudopotentials for multiparticle interactions in the quantum hall regime,” *Physical Review B*, vol. 75, no. 19, p. 195306, 2007.
- [35] F. W. Olver, D. W. Lozier, R. F. Boisvert, and C. W. Clark, *NIST Handbook of Mathematical Functions*. Cambridge University Press, 2010.
- [36] U. Merkt, J. Huser, and M. Wagner, “Energy spectra of two electrons in a harmonic quantum dot,” *Physical Review B*, vol. 43, no. 9, p. 7320, 1991.
- [37] M. Wagner, U. Merkt, and A. Chaplik, “Spin-singlet–spin-triplet oscillations in quantum dots,” *Physical Review B*, vol. 45, no. 4, p. 1951, 1992.
- [38] P. Maksym, “Eckardt frame theory of interacting electrons in quantum dots,” *Physical Review B*, vol. 53, no. 16, p. 10871, 1996.
- [39] M. Dineykhon and R. Nazmitdinov, “Two-electron quantum dot in a magnetic field: analytical results,” *Physical Review B*, vol. 55, no. 20, p. 13707, 1997.
- [40] S. A. Mikhailov and N. A. Savostianova, “Quantum-dot lithium in the strong-interaction regime: Depolarization of electron spins by a magnetic field,” *Physical Review B*, vol. 66, no. 3, p. 033307, 2002.
- [41] M. Tavernier, E. Anisimovas, F. Peeters, B. Szafran, J. Adamowski, and S. Bednarek, “Four-electron quantum dot in a magnetic field,” *Physical Review B*, vol. 68, no. 20, p. 205305, 2003.
- [42] C. Yannouleas and U. Landman, “Two-dimensional quantum dots in high magnetic fields: rotating-electron-molecule versus composite-fermion approach,” *Physical Review B*, vol. 68, no. 3, p. 035326, 2003.
- [43] G. S. Jeon, C.-C. Chang, and J. K. Jain, “Composite fermion theory of correlated electrons in semiconductor quantum dots in high magnetic fields,” *Physical Review B*, vol. 69, no. 24, p. 241304, 2004.
- [44] Y. Nishi, P. Maksym, D. Austing, T. Hatano, L. Kouwenhoven, H. Aoki, and S. Tarucha, “Intermediate low spin states in a few-electron quantum dot in the $\nu = 1$ regime,” *Physical Review B*, vol. 74, no. 3, p. 033306, 2006.
- [45] O. Ciftja, “Generalized description of few-electron quantum dots at zero and nonzero magnetic fields,” *Journal of Physics: Condensed Matter*, vol. 19, no. 4, p. 046220, 2007.

- [46] Z. Dai, J.-L. Zhu, N. Yang, and Y. Wang, “Spin-dependent rotating wigner molecules in quantum dots,” *Physical Review B*, vol. 76, no. 8, p. 085308, 2007.
- [47] N. Simonović and R. Nazmitdinov, “Magnetic alteration of entanglement in two-electron quantum dots,” *Physical Review A*, vol. 92, no. 5, p. 052332, 2015.
- [48] E. Wach, D. Żebrowski, and B. Szafran, “Imaging quantum-dot-confined electron density in transition to fractional quantum hall regime,” *Semiconductor Science and Technology*, vol. 30, no. 1, p. 015020, 2014.
- [49] P. Kramer and T. Kramer, “Interacting electrons in a magnetic field in a center-of-mass free basis,” *Physica Scripta*, vol. 90, no. 7, p. 074014, 2015.
- [50] S. T. Rittenhouse, A. Wray, and B. Johnson, “Hyperspherical approach to a three-boson problem in two dimensions with a magnetic field,” *Physical Review A*, vol. 93, no. 1, p. 012511, 2016.
- [51] R. Wooten, B. Yan, and C. H. Greene, “Few-body collective excitations beyond kohn’s theorem in quantum hall systems,” *Physical Review B*, vol. 95, no. 3, p. 035150, 2017.
- [52] L. Delves, “Tertiary and general-order collisions,” *Nuclear Physics*, vol. 9, no. 3, pp. 391–399, 1958.
- [53] ———, “Tertiary and general-order collisions (ii),” *Nuclear Physics*, vol. 20, pp. 275–308, 1960.
- [54] Y. F. Smirnov and K. Shitikova, “Method of k harmonics and the shell model,” *Sov. J. Particles Nucl.(Engl. Transl.);(United States)*, vol. 8, no. 3, 1977.
- [55] J. S. Avery, *Hyperspherical harmonics: applications in quantum theory*. Springer Science & Business Media, 2012, vol. 5.
- [56] S. T. Rittenhouse, M. Cavagnero, J. von Stecher, and C. H. Greene, “Hyperspherical description of the degenerate fermi gas: s-wave interactions,” *Physical Review A*, vol. 74, no. 5, p. 053624, 2006.
- [57] M. F. De La Ripelle, S. Sofianos, and R. Adam, “Method for solving the many-body bound state nuclear problem,” *Annals of Physics*, vol. 316, no. 1, pp. 107–159, 2005.
- [58] M. F. de La Ripelle and J. Navarro, “The first order of the hyperspherical harmonic expansion method,” *Annals of physics*, vol. 123, no. 1, pp. 185–232, 1979.
- [59] N. Timofeyuk, “Shell model approach to construction of a hyperspherical basis for a identical particles: Application to hydrogen and helium isotopes,” *Physical Review C*, vol. 65, no. 6, p. 064306, 2002.
- [60] N. Smirnova, A. De Maesschalck, A. Van Dyck, and K. Heyde, “Shell-model description of monopole shift in neutron-rich cu,” *Physical Review C*, vol. 69, no. 4, p. 044306, 2004.
- [61] V. Efros, “Hyperspherical/oscillator brackets and symmetrized states: A simple algorithm for a_j 3 few-body calculations,” *Few-Body Systems*, vol. 19, no. 3, pp. 167–173, 1995.

- [62] N. Barnea, “Hyperspherical functions with arbitrary permutational symmetry: Reverse construction,” *Physical Review A*, vol. 59, no. 2, p. 1135, 1999.
- [63] R. Krivec, “Fbs colloquium hyperspherical-harmonics methods for few-body problems,” *Few-Body Systems*, vol. 25, no. 4, pp. 199–238, 1998.
- [64] M. Viviani, “Transformation coefficients of hyperspherical harmonic functions of an-body system,” *Few-body systems*, vol. 25, no. 4, pp. 177–187, 1998.
- [65] “In typical systems, fractional quantum hall states appear at a higher magnetic field. different physical cut-offs of the system size correspond to changing of the particle density, which also changes the position of the fractional quantum hall states. in the present example, the maximum hyperradius cut-off is chosen such that the integer quantum hall effect appears at around 1 tesla.”
- [66] J. Bardeen, L. N. Cooper, and J. R. Schrieffer, “Theory of superconductivity,” *Physical Review*, vol. 108, no. 5, p. 1175, 1957.
- [67] D. Osheroff, R. Richardson, and D. Lee, “Evidence for a new phase of solid he 3,” *Physical Review Letters*, vol. 28, no. 14, p. 885, 1972.
- [68] K. B. Davis, M.-O. Mewes, M. R. Andrews, N. J. van Druten, D. S. Durfee, D. Kurn, and W. Ketterle, “Bose-einstein condensation in a gas of sodium atoms,” *Physical Review Letters*, vol. 75, no. 22, p. 3969, 1995.
- [69] N. Samkharadze, K. Schreiber, G. Gardner, M. Manfra, E. Fradkin, and G. Csáthy, “Observation of a transition from a topologically ordered to a spontaneously broken symmetry phase,” *Nature Physics*, vol. 12, no. 2, p. 191, 2016.
- [70] D. T. Son, “Is the composite fermion a dirac particle?” *Physical Review X*, vol. 5, no. 3, p. 031027, 2015.
- [71] S. Girvin, A. MacDonald, and P. Platzman, “Collective-excitation gap in the fractional quantum hall effect,” *Physical Review Letters*, vol. 54, no. 6, p. 581, 1985.
- [72] —, “Magneto-roton theory of collective excitations in the fractional quantum hall effect,” *Physical Review B*, vol. 33, no. 4, p. 2481, 1986.
- [73] W. Kohn, “Cyclotron resonance and de haas-van alphen oscillations of an interacting electron gas,” *Physical Review*, vol. 123, no. 4, p. 1242, 1961.
- [74] S. Ilani, J. Martin, E. Teitelbaum, J. Smet, D. Mahalu, V. Umansky, and A. Yacoby, “The microscopic nature of localization in the quantum hall effect,” *Nature*, vol. 427, no. 6972, p. 328, 2004.
- [75] A. Levy, U. Wurstbauer, Y. Kuznetsova, A. Pinczuk, L. Pfeiffer, K. West, M. Manfra, G. Gardner, and J. Watson, “Optical emission spectroscopy study of competing phases of electrons in the second landau level,” *Physical Review Letters*, vol. 116, no. 1, p. 016801, 2016.
- [76] T. Maag, A. Bayer, S. Baierl, M. Hohenleutner, T. Korn, C. Schüller, D. Schuh, D. Bougeard, C. Lange, R. Huber *et al.*, “Coherent cyclotron motion beyond kohns theorem,” *Nature Physics*, vol. 12, no. 2, p. 119, 2016.

- [77] D. Yoshioka, B. Halperin, and P. Lee, “Ground state of two-dimensional electrons in strong magnetic fields and $1/3$ quantized hall effect,” *Physical Review Letters*, vol. 50, no. 16, p. 1219, 1983.
- [78] G. S. Jeon, C.-C. Chang, and J. K. Jain, “Composite fermion theory of correlated electrons in semiconductor quantum dots in high magnetic fields,” *Physical Review B*, vol. 69, no. 24, p. 241304, 2004.
- [79] C. Yannouleas and U. Landman, “Unified microscopic approach to the interplay of pinned-wigner-solid and liquid behavior of the lowest landau-level states in the neighborhood of $\nu=1/3$,” *Physical Review B*, vol. 84, no. 16, p. 165327, 2011.
- [80] Y. F. Smirnov and K. Shitikova, “Physics of elementary particles and atomic nuclei,” *Fiz. Elem. Chastits. At. Yadra*, vol. 8, p. 847, 1977.
- [81] J. J. Quinn and A. Wójs, “Composite fermions in fractional quantum hall systems,” *Journal of Physics: Condensed Matter*, vol. 12, no. 20, p. R265, 2000.
- [82] A. Wójs, “Electron correlations in partially filled lowest and excited landau levels,” *Physical Review B*, vol. 63, no. 12, p. 125312, 2001.
- [83] K. Osterloh, N. Barberán, and M. Lewenstein, “Strongly correlated states of ultracold rotating dipolar fermi gases,” *Physical Review Letters*, vol. 99, no. 16, p. 160403, 2007.
- [84] I. Tokatly and G. Vignale, “New collective mode in the fractional quantum hall liquid,” *Physical Review Letters*, vol. 98, no. 2, p. 026805, 2007.
- [85] J. Eisenstein and H. Stormer, “The fractional quantum hall effect,” *Science*, vol. 248, no. 4962, pp. 1510–1516, 1990.
- [86] A. Wójs, K.-S. Yi, and J. J. Quinn, “Fractional quantum hall states of clustered composite fermions,” *Physical Review B*, vol. 69, no. 20, p. 205322, 2004.
- [87] S. Mukherjee, S. S. Mandal, Y.-H. Wu, A. Wójs, and J. K. Jain, “Enigmatic $4/11$ state: A prototype for unconventional fractional quantum hall effect,” *Physical Review Letters*, vol. 112, no. 1, p. 016801, 2014.
- [88] D. Jin, J. Ensher, M. Matthews, C. Wieman, and E. A. Cornell, “Collective excitations of a bose-einstein condensate in a dilute gas,” *Physical Review Letters*, vol. 77, no. 3, p. 420, 1996.
- [89] E. Vogt, M. Feld, B. Fröhlich, D. Pertot, M. Koschorreck, and M. Köhl, “Scale invariance and viscosity of a two-dimensional fermi gas,” *Physical Review Letters*, vol. 108, no. 7, p. 070404, 2012.
- [90] M. Lu, N. Q. Burdick, and B. L. Lev, “Quantum degenerate dipolar fermi gas,” *Physical Review Letters*, vol. 108, no. 21, p. 215301, 2012.
- [91] M. Aymar and O. Dulieu, “Calculation of accurate permanent dipole moments of the lowest $\sigma+1, 3$ states of heteronuclear alkali dimers using extended basis sets,” *The Journal of Chemical Physics*, vol. 122, no. 20, p. 204302, 2005.

- [92] S. K. Baur, K. R. Hazzard, and E. J. Mueller, “Stirring trapped atoms into fractional quantum hall puddles,” *Physical Review A*, vol. 78, no. 6, p. 061608, 2008.
- [93] N. Gemelke, E. Sarajlic, and S. Chu, “Rotating few-body atomic systems in the fractional quantum hall regime,” *arXiv:1007.2677*, 2010.
- [94] M. Kunitski, S. Zeller, J. Voigtsberger, A. Kalinin, L. P. H. Schmidt, M. Schöffler, A. Czasch, W. Schöllkopf, R. E. Grisenti, T. Jahnke *et al.*, “Observation of the efimov state of the helium trimer,” *Science*, vol. 348, no. 6234, pp. 551–555, 2015.
- [95] F. Serwane, G. Zürn, T. Lompe, T. Ottenstein, A. Wenz, and S. Jochim, “Deterministic preparation of a tunable few-fermion system,” *Science*, vol. 332, no. 6027, pp. 336–338, 2011.
- [96] S. H. Simon and E. H. Rezayi, “Landau level mixing in the perturbative limit,” *Physical Review B*, vol. 87, no. 15, p. 155426, 2013.
- [97] I. Sodemann and A. MacDonald, “Landau level mixing and the fractional quantum hall effect,” *Physical Review B*, vol. 87, no. 24, p. 245425, 2013.
- [98] M. R. Peterson and C. Nayak, “More realistic hamiltonians for the fractional quantum hall regime in gaas and graphene,” *Physical Review B*, vol. 87, no. 24, p. 245129, 2013.
- [99] R. Wooten, J. Macek, and J. Quinn, “Including landau level mixing in numerical studies of the quantum hall effect,” *Physical Review B*, vol. 88, no. 15, p. 155421, 2013.
- [100] B. Yan, R. R. Biswas, and C. H. Greene, “Bulk-edge correspondence in fractional quantum hall states,” *Physical Review B*, vol. 99, no. 3, p. 035153, 2019.
- [101] V. Kalmeyer and R. Laughlin, “Equivalence of the resonating-valence-bond and fractional quantum hall states,” *Physical Review Letters*, vol. 59, no. 18, p. 2095, 1987.
- [102] X.-G. Wen, F. Wilczek, and A. Zee, “Chiral spin states and superconductivity,” *Physical Review B*, vol. 39, no. 16, p. 11413, 1989.
- [103] J. G. Bednorz and K. A. Müller, “Possible high c superconductivity in the Ba-La-Cu-O system,” *Zeitschrift für Physik B Condensed Matter*, vol. 64, no. 2, pp. 189–193, 1986.
- [104] X.-G. Wen, “Topological orders in rigid states,” *International Journal of Modern Physics B*, vol. 4, no. 02, pp. 239–271, 1990.
- [105] E. Witten, “Topological quantum field theory,” *Communications in Mathematical Physics*, vol. 117, no. 3, pp. 353–386, 1988.
- [106] C. Nayak, S. H. Simon, A. Stern, M. Freedman, and S. Das Sarma, “Non-abelian anyons and topological quantum computation,” *Review of Modern Physics*, vol. 80, no. 3, pp. 1083–1159, 2008.

- [107] M. Freedman, A. Kitaev, M. Larsen, and Z. Wang, “Topological quantum computation,” *Bulletin of the American Mathematical Society*, vol. 40, no. 1, pp. 31–38, 2003.
- [108] A. Y. Kitaev, “Fault-tolerant quantum computation by anyons,” *Annals of Physics*, vol. 303, no. 1, pp. 2–30, 2003.
- [109] X.-G. Wen and Q. Niu, “Ground-state degeneracy of the fractional quantum hall states in the presence of a random potential and on high-genus riemann surfaces,” *Physical Review B*, vol. 41, no. 13, pp. 9377–9396, 1990.
- [110] X. Chen, Z.-C. Gu, and X.-G. Wen, “Local unitary transformation, long-range quantum entanglement, wave function renormalization, and topological order,” *Physical Review B*, vol. 82, no. 15, p. 155138, 2010.
- [111] J. E. Moore, “The birth of topological insulators,” *Nature*, vol. 464, no. 7286, p. 194, 2010.
- [112] R. Horodecki, P. Horodecki, M. Horodecki, and K. Horodecki, “Quantum entanglement,” *Review of Modern Physics*, vol. 81, no. 2, pp. 865–942, Jun. 2009.
- [113] M. Haque, O. Zozulya, and K. Schoutens, “Entanglement entropy in fermionic Laughlin states,” *Physical Review Letters*, vol. 98, no. 6, p. 060401, 2007.
- [114] H. Li and F. Haldane, “Entanglement spectrum as a generalization of entanglement entropy: Identification of topological order in non-abelian fractional quantum hall effect states,” *Physical Review Letters*, vol. 101, no. 1, p. 010504, 2008.
- [115] X.-L. Qi, H. Katsura, and A. W. Ludwig, “General relationship between the entanglement spectrum and the edge state spectrum of topological quantum states,” *Physical Review Letters*, vol. 108, no. 19, p. 196402, 2012.
- [116] B. Swingle and T. Senthil, “Geometric proof of the equality between entanglement and edge spectra,” *Physical Review B*, vol. 86, no. 4, p. 045117, 2012.
- [117] J. Dubail, N. Read, and E. Rezayi, “Edge-state inner products and real-space entanglement spectrum of trial quantum hall states,” *Physical Review B*, vol. 86, no. 24, p. 245310, 2012.
- [118] A. Kitaev and J. Preskill, “Topological entanglement entropy,” *Physical Review Letters*, vol. 96, no. 11, p. 110404, 2006.
- [119] Z. Liu, D. L. Kovrizhin, and E. J. Bergholtz, “Bulk-edge correspondence in fractional Chern insulators,” *Physical Review B*, vol. 88, no. 8, p. 081106, 2013.
- [120] R. A. Santos, “Bulk-edge correspondence of entanglement spectrum in two-dimensional spin ground states,” *Physical Review B*, vol. 87, no. 3, p. 035141, 2013.
- [121] W. W. Ho, L. Cincio, H. Moradi, D. Gaiotto, and G. Vidal, “Edge-entanglement spectrum correspondence in a nonchiral topological phase and Kramers-Wannier duality,” *Physical Review B*, vol. 91, no. 12, p. 125119, 2015.

- [122] X. Chen, A. Tiwari, and S. Ryu, “Bulk-boundary correspondence in (3+1)-dimensional topological phases,” *Physical Review B*, vol. 94, no. 4, p. 045113, 2016.
- [123] W. W. Ho, L. Cincio, H. Moradi, and G. Vidal, “Universal edge information from wave-function deformation,” *Physical Review B*, vol. 95, no. 23, p. 235110, 2017.
- [124] M. Koch-Janusz, K. Dhochak, and E. Berg, “Edge-entanglement correspondence for a gapped topological phase with symmetry,” *Physical Review B*, vol. 95, no. 20, p. 205110, 2017.
- [125] O. S. Zozulya, M. Haque, K. Schoutens, and E. H. Rezayi, “Bipartite entanglement entropy in fractional quantum hall states,” *Physical Review B*, vol. 76, no. 12, p. 125310, 2007.
- [126] A. Sterdyniak, N. Regnault, and B. A. Bernevig, “Extracting excitations from model state entanglement,” *Physical Review Letters*, vol. 106, no. 10, p. 100405, 2011.
- [127] A. Chandran, M. Hermanns, N. Regnault, and B. A. Bernevig, “Bulk-edge correspondence in entanglement spectra,” *Physical Review B*, vol. 84, no. 20, p. 205136, 2011.
- [128] A. M. Läuchli, E. J. Bergholtz, J. Suorsa, and M. Haque, “Disentangling entanglement spectra of fractional quantum hall states on torus geometries,” *Physical Review Letters*, vol. 104, no. 15, p. 156404, 2010.
- [129] J. Dubail, N. Read, and E. Rezayi, “Real-space entanglement spectrum of quantum hall systems,” *Physical Review B*, vol. 85, no. 11, p. 115321, 2012.
- [130] A. Sterdyniak, A. Chandran, N. Regnault, B. A. Bernevig, and P. Bonderson, “Real-space entanglement spectrum of quantum hall states,” *Physical Review B*, vol. 85, no. 12, p. 125308, 2012.
- [131] I. D. Rodríguez, S. H. Simon, and J. K. Slingerland, “Evaluation of ranks of real space and particle entanglement spectra for large systems,” *Physical Review Letters*, vol. 108, no. 25, p. 256806, 2012.
- [132] X.-G. Wen, “Theory of the edge states in fractional quantum hall effects,” *International Journal of Modern Physics B*, vol. 6, no. 10, pp. 1711–1762, 1992.
- [133] —, “Electrodynamical properties of gapless edge excitations in the fractional quantum hall states,” *Physical Review Letters*, vol. 64, no. 18, p. 2206, 1990.
- [134] —, “Chiral luttinger liquid and the edge excitations in the fractional quantum hall states,” *Physical Review B*, vol. 41, no. 18, p. 12838, 1990.
- [135] H. Li, “Numerical studies of quantum entanglement in fractional quantum hall effect systems,” *Dissertation at Princeton University*, 2009.

APPENDICES

A. BOSON-FERMION CORRESPONDENCE

Representation of (Anti-)Symmetric Polynomials

Denote λ and μ the partition of an integer M , e.g., $\lambda = \{n_1, \dots, n_i, \dots, n_N\}$, where $n_1 \leq \dots \leq n_i \leq \dots \leq n_N$ are N non-negative integers summing up to M . For each partition there associates a unique Slater determinant and a monomial symmetric polynomial, which are defined respectively as

$$m_\lambda = \hat{\mathcal{S}} \prod_{i=1}^M z_i^{n_i} d_\lambda = \hat{\mathcal{A}} \prod_{i=1}^M z_i^{n_i}, \quad (\text{A.1})$$

where $\hat{\mathcal{S}}$ and $\hat{\mathcal{A}}$ are symmetrization and anti-symmetrization operators. For a given set of all partitions $\{\lambda\}$ of integer M with a fixed length N , m_λ and d_λ form a complete basis for the symmetric and anti-symmetric polynomials of N variables and total order M , respectively. Beside the monomial symmetric functions, we introduce here another basis for the symmetric polynomials of order M , the Schur functions, which is defined from a given partition λ as

$$s_\lambda = \frac{d_{\bar{\lambda}}}{\prod_{z_i > z_j} (z_i - z_j)}, \quad (\text{A.2})$$

where $\bar{\lambda}$ is a partition that generated from λ :

$$\bar{\lambda} = \{n_1, n_2 - 1, n_3 - 2, \dots, n_i - (i - 1), \dots, n_N - (N - 1)\}. \quad (\text{A.3})$$

It can be checked that s_λ has the correct order of M . The transformation between the basis of Schur functions and the monomial symmetric polynomials is an important subject in the field of representation theory. There is a well know quantity, the Kostka number, $K_{\lambda\mu}$, that relates the two basis:

$$s_\lambda = \sum_{\mu} K_{\lambda\mu} m_\mu. \quad (\text{A.4})$$

We quote here a formula for the inverse Kostka number $K_{\lambda\mu}^{-1}$ which is the coefficient of the inverse transformation

$$m_\lambda = \sum_{\mu} K_{\lambda\mu}^{-1} s_\mu. \quad (\text{A.5})$$

$K_{\lambda\mu}^{-1}$ is recurrently given by

$$K_{\lambda\mu}^{-1} = \sum_{1 \leq j \leq d \text{ and } r_j = \mu_i + i - 1} (-1)^{i-1} K_{\lambda[j], \{\mu_1 - 1, \dots, \mu_{i-1} - 1, \mu_{i+1}, \dots, \mu_l\}}^{-1}. \quad (\text{A.6})$$

Here, we assume that μ has no zero elements. d is the number of groups of identical numbers in the partition λ . $\lambda[j]$ refers as a new partition that is generated by removing a number r_j from the j -th group of identical numbers in λ . For instance, if $\lambda = \{1, 1, 3, 3, 3, 4, 6\}$, then $d = 4$ and $\lambda[2] = \{1, 1, 3, 3, 4, 6\}$.

Mapping of Boson and Fermion Wave Functions

Equipped with a normalization factor and an exponential Gaussian factor (which are usually ignored), each of the above polynomial corresponds to a N body bosonic or fermionic wave function in the lowest Landau level with total angular momentum M :

$$\phi_\lambda^B = N_\lambda^B m_\lambda \phi_\lambda^F = N_\lambda^F d_\lambda, \quad (\text{A.7})$$

where N is the normalization factor which has known analytic forms. The indexes F and B labels fermion and boson respectively. Schur functions in Eq.A.2 can also be used as the many-body basis functions. However, there are two defects of using Schur functions: 1) the analytic normalization factors can not be trivially found; 2) they are not orthogonal under the normal definition of inner product between quantum mechanical wave functions. The mapping introduced in Chapter 2 generally maps each ϕ_λ^B into a linear combination of ϕ_λ^F in the corresponding fermionic Hilbert space. To find out the transformation coefficients, we note the fact that ϕ_λ^B can be expanded into Schur functions with the help of Kostka numbers. Each Schur function would be mapped to a single functions ϕ_λ^F , which is apparently seen from the definition Eq. (A.2). This process is as following.

Assume a generic normalized N boson wave function

$$\Psi^B = \sum_i c_i^B \phi_i^B, \quad (\text{A.8})$$

which can be written in terms of monomial symmetric functions and farther be expanded into Schur functions:

$$\begin{aligned} \Psi^B &= \sum_i c_i^B N_i^B m^i \\ &= \sum_{i,j} c_i^B N_i^B \hat{K}_{ij}^{-1} s_j. \end{aligned} \quad (\text{A.9})$$

The resulting N fermion wave function mapped from the above bosonic wave function is

$$\Psi^F = \mathcal{A} \prod_{z_i > z_j} (z_i - z_j) \sum_{i,j} c_i^B N_i^B \hat{K}_{ij}^{-1} s_j, \quad (\text{A.10})$$

where \mathcal{A} is an overall normalization of the wave function Ψ^F . Using Eq. A.2, the Schur function together with the Vandermonde factor are farther transformed into Slater determinant:

$$\Psi^F = \mathcal{A} \sum_{i,j} c_i^B N_i^B \hat{K}_{ij}^{-1} \frac{1}{N_j^F} \phi_j^F. \quad (\text{A.11})$$

We now get the mapped fermionic wave function which has expanding coefficients

$$c_j^F = \mathcal{A} \sum_{i,j} c_i^B N_i^B \hat{K}_{ij}^{-1} / N_j^F. \quad (\text{A.12})$$

B. TWO-BODY MATRIX ELEMENTS OF THE COULOMB POTENTIAL

In this section we derive the formula for the Coulomb potential matrix elements in the basis of two-body state. The derivations are carried out generally, involving particles in any Landau levels.

Notations

The single particle state can be written as:

$$\psi_n^m(r, \phi) = \sqrt{\frac{n!}{2^{|m|+1}\pi(n+|m|)!}} e^{im\phi} r^{|m|} e^{-r^2/4} L_n^{|m|}(r^2/2) \quad (\text{B.1})$$

with energy and angular momentum

$$\begin{aligned} E &= \hbar\omega_c \left(n + \frac{m+|m|}{2} + \frac{1}{2} \right), \quad n = 0, 1, 2, \dots, +\infty \\ L_z &= m\hbar \quad m = n, n-1, \dots, 0, -1, -2, \dots -\infty \end{aligned} \quad (\text{B.2})$$

Denote $|n, m\rangle$ as the single particle state (here n has a different meaning as in Eq. B.1) on the n 'th Landau level, with energy $\hbar\omega_c(n + \frac{1}{2})$ and angular momentum quantum number m . Under this convention, $|n, m\rangle$ takes the form of Eq. B.1 with effective nodal quantum number

$$n_{eff} = n - \frac{m+|m|}{2}. \quad (\text{B.3})$$

Define the following Ladder operators:

$$\begin{aligned}
\hat{a}^\dagger &= -i\sqrt{\frac{1}{2}}(2\partial - \frac{1}{2}\bar{z}) \\
\hat{a} &= -i\sqrt{\frac{1}{2}}(2\bar{\partial} + \frac{1}{2}z) \\
\hat{b}^\dagger &= \sqrt{\frac{1}{2}}(-2\bar{\partial} + \frac{1}{2}z) \\
\hat{b} &= \sqrt{\frac{1}{2}}(2\partial + \frac{1}{2}\bar{z})
\end{aligned} \tag{B.4}$$

then the state $|n, m\rangle$ can be generated with raising operators from the vacuum state $|0\rangle$:

$$|n, m\rangle = \mathcal{A}\hat{a}^\dagger\hat{b}^{\dagger n-m}|0\rangle, \tag{B.5}$$

or be eliminated using lowering operators:

$$\mathcal{A}\hat{a}\hat{b}^{n-m}|n, m\rangle = |0\rangle, \tag{B.6}$$

where \mathcal{A} is the normalization factor

$$\mathcal{A} = \frac{(-1)^{\min\{n, n-m\}}}{\sqrt{n!(n-m)!}}, \tag{B.7}$$

and

$$\min\{n, n-m\} = n - \frac{m + |m|}{2}. \tag{B.8}$$

Transformation of Basis

Denote $|n_1 m_1 n_2 m_2\rangle$ as a two body state where the first particle is in state $|n_1 m_1\rangle$ and the second in state $|n_2 m_2\rangle$. Another useful two-body basis is the center of mass(CM) and relative coordinate basis $|NMnm\rangle$, which means that the CM motion is in the state $|NM\rangle$ and the relative coordinate motion is in state $|nm\rangle$. Next we derive the transformation coefficients between these two basis. Using Eq.B.6, $|n_1 m_1 n_2 m_2\rangle$ can be written as

$$\langle n_1 m_1 n_2 m_2 | = \langle 0 | \mathcal{A}_1 \mathcal{A}_2 \hat{a}_1^{n_1} \hat{b}_1^{n_1 - m_1} \hat{a}_2^{n_2} \hat{b}_2^{n_2 - m_2}. \tag{B.9}$$

Expand the single particle basis Ladder operators with CM-relative coordinate basis operators as

$$\begin{aligned}
& \hat{a}_1^{n_1} \hat{b}_1^{n_1-m_1} \hat{a}_2^{n_2} \hat{b}_2^{n_2-m_2} \\
& = \mathcal{C} (\hat{a}_c + \hat{a}_r)^{n_1} (\hat{b}_c + \hat{b}_r)^{n_1-m_1} (\hat{a}_c - \hat{a}_r)^{n_2} (\hat{b}_c - \hat{b}_r)^{n_2-m_2} \\
& = \mathcal{C} \sum_{i=0}^{n_1} \sum_{j=0}^{n_2} \sum_{k=0}^{n_1-m_1} \sum_{l=0}^{n_2-m_2} (-1)^{2n_2-m_2-j-l} \\
& \quad \times C_{n_1}^i C_{n_2}^j C_{n_1-m_1}^k C_{n_2-m_2}^l \hat{a}_c^{i+j} \hat{a}_r^{n_1+n_2-i-j} \hat{b}_c^{k+l} \hat{b}_r^{n_1+n_2-m_1-m_2-k-l}
\end{aligned} \tag{B.10}$$

where $\mathcal{C} = (1/\sqrt{2})^{2n_1+2n_2-m_1-m_2}$. In doing the inner product between the two basis, the only survived terms in the above summation are those that satisfy

$$\begin{aligned}
i + j &= N \\
k + l &= N - M \\
n_1 + n_2 &= N + n \\
m_1 + m_2 &= M + m,
\end{aligned} \tag{B.11}$$

leaving the final transformation coefficient as

$$\begin{aligned}
& \langle n_1 m_1 n_2 m_2 | N M n m \rangle \\
& = \mathcal{C} \frac{\mathcal{A}_1 \mathcal{A}_2}{\mathcal{A}_c \mathcal{A}_r} \sum_{i=0}^{n_1} \sum_{j=0}^{n_2} \sum_{k=0}^{n_1-m_1} \sum_{l=0}^{n_2-m_2} (-1)^{2n_2-m_2-j-l} C_{n_1}^i C_{n_2}^j C_{n_1-m_1}^k C_{n_2-m_2}^l,
\end{aligned} \tag{B.12}$$

where factor \mathcal{A} s are given by Eq. B.7.

Coulomb Pseudo-Potential

In the following we derive the analytic formula for the Coulomb potential matrix element in the basis of two-body CM-relative coordinate basis, $\langle N M n m | \hat{V} | N' M' n' m' \rangle$. In the lowest Landau level, this term has the form of $\delta_{N,N'} \delta_{M,M'} \delta_{n,n'} \delta_{m,m'} V(m)$, where $V(m)$ is know as the Haldane pseudo-potential. Generally, including higher Landau levels, the two-body Coulomb matrix elements read

$$\begin{aligned}
& \langle \psi_N^M(R, \Phi), \psi_n^m(r, \phi) | \frac{1}{\sqrt{2r}} | \psi_{N'}^{M'}(R, \Phi) \psi_{n'}^{m'}(r, \phi) \rangle \\
& = \mathcal{N} \mathcal{N}' \sqrt{2\pi} \delta_{m,m'} \delta_{N,N'} \delta_{M,M'} \int_0^\infty dr r^{2|m|} e^{-r^2/2} L_n^{|m|} \left(\frac{r^2}{2} \right) L_{n'}^{|m|} \left(\frac{r^2}{2} \right),
\end{aligned} \tag{B.13}$$

where \mathcal{N} is the normalization factor of the single particle wave function, $L_n^m(x)$ is the generalized Laguerre polynomial. Note that in the above equation, N and n are nodal quantum numbers given by Eq. B.1, instead of Landau level indexes. To perform the calculation numerically, we farther reduce the above integration to

$$\begin{aligned}
& \int_0^\infty dr r^{2|m|} e^{-r^2/2} L_n^{|m|} \left(\frac{r^2}{2} \right) L_{n'}^{|m|} \left(\frac{r^2}{2} \right) \\
& = \int_0^\infty dr r^{2|m|} e^{-r^2/2} \sum_{i=0}^n (-1)^i C_{n+|m|}^{n-i} \frac{(r^2/2)^i}{i!} \sum_{j=0}^{n'} (-1)^j C_{n'+|m|}^{n'-j} \frac{(r^2/2)^j}{j!} \\
& = \sum_{i=0}^n \sum_{j=0}^{n'} \frac{(-1/2)^{i+j} C_{n+|m|}^{n-i} C_{n'+|m|}^{n'-j}}{i! j!} \int_0^\infty dr e^{-r^2/2} r^{2|m|+2i+2j} \\
& = \sum_{i=0}^n \sum_{j=0}^{n'} \frac{(-1/2)^{i+j} C_{n+|m|}^{n-i} C_{n'+|m|}^{n'-j}}{i! j!} (2|m| + 2i + 2j - 1)!!.
\end{aligned} \tag{B.14}$$

C. ENUMERATION OF SLATER DETERMINANTS OF A FIXED $\{K, M_{TOT}\}$ MANIFOLD

As stated earlier, listing the complete set of N -particle Slater determinants spanning a fixed $\{K, M_{tot}\}$ manifold is equivalent to finding the complete list of sets of single-particle orbitals that satisfy the rules listed in Section 3.2.1. Because N , K , M_{tot} , and all of the single-particle orbital quantum numbers are integers, we can use techniques from number theory to find the allowed sets of single-particle orbitals. One efficient method for finding the Slater determinants is to find the integer partitions on K and on the number of total excitations in the desired system, and use those partitions to construct contingency tables.

We start by noting that the grand angular momentum K is the total order of the harmonic polynomial part of the final, N -particle Slater determinants.

Since K is the order of the polynomial we seek, we must include all Slater determinants in which the polynomial orders of the individual orbitals sum up to K . The order of the polynomial of the single-particle orbital $|\epsilon, m\rangle$ is $2\epsilon - m$, thus the restriction is

$$K = \sum_{j=1}^N (2\epsilon_j - m_j) = 2n_\epsilon - M_{tot}. \quad (\text{C.1})$$

Here, n_ϵ is the total number of Landau level excitations. This restriction is equivalent to finding the integer partitions of K of length less than or equal to N , where the partition of an integer A of length B is simply the list of all possible (ordered) sets of integers that sum up to A with exactly B elements in each ordered set.

For example, for a three particle system and $K = 4$, the allowed partitions are $[4, 0, 0]$, $[3, 1, 0]$, $[2, 2, 0]$, and $[2, 1, 1]$. For this system, there are 4 different ways to divide the total polynomial order, K , among the 3 single-particle orbitals without any reference to the information about the specific orbitals chosen.

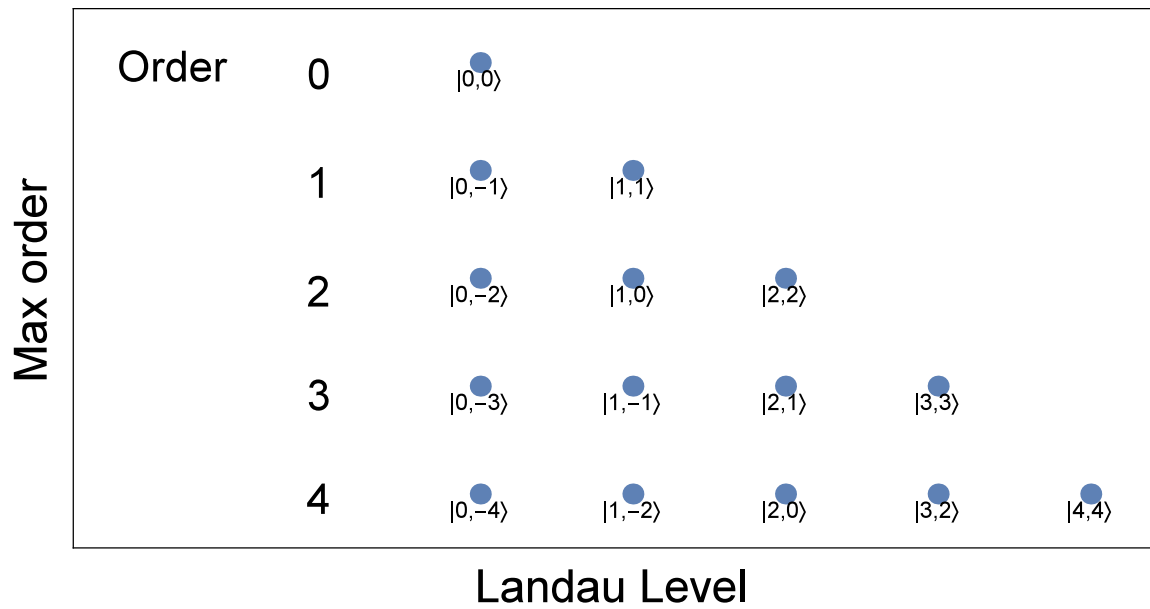


Fig. C.1. Diagram describing the ordering of the single-particle orbitals $|\epsilon, m\rangle$ by Landau level and order of the polynomial.

Figure C.1 shows how the single-particle orbitals are arranged by the order of their polynomial part and Landau level. Notice that the integer partitions of K can be recast into an alternate notation which identifies the number of orbitals to pick from each row of Fig. C.1. Taking partition $[4, 0, 0]$, for example, it is recast to $\{2, 0, 0, 0, 1\}$, which means we can pick two orbitals of order 0, no orbitals of order 1, no orbitals of order 2, no orbitals of order 3, and one orbital of order 4. The rest of the partitions in this example become $\{1, 1, 0, 1\}$, $\{1, 0, 2\}$, and $\{0, 2, 1\}$, respectively.

The second observation is that there is only one orbital with order 0 polynomial ($|0, 0\rangle$), only two orbitals of order 1 ($|0, -1\rangle$ and $|1, 1\rangle$), three orbitals of order 2 ($|0, -2\rangle$, $|1, 0\rangle$, and $|2, 2\rangle$), and so on. This presents an additional restriction; namely, in this example the $\{2, 0, 0, 0, 1\}$ set of column choices is not allowed because one can not take two unique orbitals from the 0th-order set of orbitals.

We perform a similar partitioning and restriction by fixing M . This can be done by brute force to enumerate every possibility given the restrictions on K , but this is inefficient. Alternatively, the restriction on M can be restated as a restriction on the number of Landau level excitations n_ϵ . Looking back at Eq. (C.1), the total number of Landau level excitations is equal to $n_\epsilon = (K + M_{tot})/2$. Dividing the number of excitations among the different Landau levels is again equivalent to finding the integer partitions, this time of n_ϵ , restricted by the number of particles. Continuing the example for $N = 3$ and $K = 4$, if $M_{tot} = 0$, then this implies that $n_\epsilon = 2$ and its integer partitions are $[2, 0, 0]$ and $[1, 1, 0]$. Recasting these in terms of the number of orbitals to pick from each column of Fig. C.1, yields $\{2, 0, 1\}$ and $\{1, 2\}$, respectively.

Combining the results, from the restrictions on K we have all possible lists of the number of orbitals to choose from each *row* of Figure C.1, and from the restrictions on n_ϵ we have all possible lists of the number of orbitals to choose from each *column* of Figure C.1. Said differently, the number of Slater determinants that contribute to the subspace of fixed M and K is equivalent to counting all possible triangular binary rectangular contingency tables with specified margins.

The row margins, that is, the restricted sums over row elements, are given by the set of numbers that count how many times a given number appears in the integer partitions of K . The column margins, that is, the restricted sums over column elements, are given by the set of numbers that count how many times a given number appears in the integer partitions of n_ϵ . Both integer partitions are restricted to have no more than N parts. There are known algorithms to efficiently enumerate the possibilities, but the problem scales polynomially with K and n_ϵ .

Continuing the example, there are six possible contingency matrices:

$$\begin{array}{c}
 \begin{array}{c} 2 \ 0 \ 1 \\ \hline 1 \left| \begin{array}{ccc} \cdot & 0 & 0 \\ 1 & \cdot & 0 \\ 0 & \cdot & \cdot \\ 1 & \cdot & \cdot \end{array} \right. \end{array} \quad
 \begin{array}{c} 1 \ 2 \\ \hline 1 \left| \begin{array}{cc} \cdot & 0 \\ \cdot & \cdot \\ \cdot & \cdot \\ \cdot & \cdot \end{array} \right. \end{array} \quad
 \begin{array}{c} 2 \ 0 \ 1 \\ \hline 1 \left| \begin{array}{ccc} \cdot & 0 & 0 \\ \cdot & \cdot & 0 \\ \cdot & \cdot & \cdot \end{array} \right. \end{array} \\
 \end{array} \tag{C.2}$$

$$\begin{array}{c}
 \begin{array}{c} 1 \ 2 \\ \hline 1 \left| \begin{array}{cc} \cdot & 0 \\ \cdot & \cdot \\ \cdot & \cdot \end{array} \right. \end{array} \quad
 \begin{array}{c} 2 \ 0 \ 1 \\ \hline 0 \left| \begin{array}{ccc} \cdot & 0 & 0 \\ \cdot & \cdot & 0 \\ \cdot & \cdot & \cdot \end{array} \right. \end{array} \quad
 \begin{array}{c} 1 \ 2 \\ \hline 0 \left| \begin{array}{cc} \cdot & 0 \\ \cdot & \cdot \\ \cdot & \cdot \end{array} \right. \end{array} \\
 \end{array} \tag{C.3}$$

The row and column restrictions are indicated to the left of and above the matrices, respectively. The upper triangle of each is made up of zeros as there are no orbitals to pick from in these locations. Dots indicate elements that are unknown within the matrix (not including trivial zero rows or zero columns). By inspection, it is straightforward to enumerate all possible matrices, namely

$$\begin{array}{c}
 \begin{array}{c} 2 \ 0 \ 1 \\ \hline 1 \left| \begin{array}{ccc} 1 & 0 & 0 \\ 1 & 0 & 0 \\ 0 & 0 & 0 \\ 1 & 0 & 0 \end{array} \right. \end{array} \quad
 \begin{array}{c} 1 \ 2 \\ \hline 1 \left| \begin{array}{cc} 1 & 0 \\ 0 & 1 \\ 0 & 0 \\ 0 & 1 \end{array} \right. \end{array} \quad
 \begin{array}{c} 2 \ 0 \ 1 \\ \hline 1 \left| \begin{array}{ccc} 1 & 0 & 0 \\ 0 & 0 & 0 \\ 1 & 0 & 1 \end{array} \right. \end{array} \quad
 \begin{array}{c} 1 \ 2 \\ \hline 0 \left| \begin{array}{cc} 0 & 0 \\ 1 & 1 \\ 0 & 1 \end{array} \right. \end{array} \\
 \end{array} \tag{C.4}$$

which translate to the Slater determinants $|0, 0\rangle|0, -1\rangle|2, 1\rangle$, $|0, 0\rangle|1, 1\rangle|1, -1\rangle$, $|0, 0\rangle|0, -2\rangle|2, 2\rangle$, and $|0, -1\rangle|1, 1\rangle|1, 0\rangle$, respectively. It is observable that by restricting n_e , all of these Slater determinants do in fact have $M_{tot} = 0$, as was desired. In practice, we enumerate the possible configurations of a single contingency matrix by starting with the first column. For the first column there are $\binom{N}{c_1}$ possible 0-1 column vectors, where c_1 is the first column restriction. Choosing one of the allowed 0-1 column vectors, the resulting counting problem is identical to the previous step, though with a new matrix of one less column and new row restrictions.

D. CENTER-OF-MASS OPERATORS

Expressed in terms of the ladder operators, the single-particle coordinates are

$$x = \frac{1}{2^{1/2}} (a + a^\dagger + b + b^\dagger) \quad y = \frac{i}{2^{1/2}} (a - a^\dagger - b + b^\dagger) \quad (\text{D.1})$$

$$\frac{\partial}{\partial x} = \frac{1}{2^{3/2}} (a - a^\dagger + b - b^\dagger) \quad \frac{\partial}{\partial y} = \frac{-i}{2^{3/2}} (-a - a^\dagger + b + b^\dagger). \quad (\text{D.2})$$

The center of mass coordinates and its partial derivatives, expressed in the single-particle coordinates, are

$$x_{CM} = \frac{1}{N} \sum_{j=1}^N x_j \quad y_{CM} = \frac{1}{N} \sum_{j=1}^N y_j \quad (\text{D.3})$$

$$\frac{\partial}{\partial x_{CM}} = \sum_{j=1}^N \frac{\partial}{\partial x_j} \quad \frac{\partial}{\partial y_{CM}} = \sum_{j=1}^N \frac{\partial}{\partial y_j}. \quad (\text{D.4})$$

In the following, it is also useful to use the commutator relations, which are

$$[a, a^\dagger] = 1 \quad (\text{D.5})$$

$$[b, b^\dagger] = 1 \quad (\text{D.6})$$

$$[a, b] = [a^\dagger, b^\dagger] = [a^\dagger, b] = [a, b^\dagger] = 0. \quad (\text{D.7})$$

Angular Momentum

The angular momentum of the center of mass becomes

$$\begin{aligned}
L_{CM} &= -i\hbar \left(x_{CM} \frac{\partial}{\partial y_{CM}} - y_{CM} \frac{\partial}{\partial x_{CM}} \right) \\
&= -\frac{i\hbar}{N} \sum_{j=1}^N \sum_{k=1}^N \left(x_j \frac{\partial}{\partial y_k} - y_j \frac{\partial}{\partial x_k} \right) \\
&= -\frac{\hbar}{4N} \sum_{j=1}^N \sum_{k=1}^N \left[\left(a_j + a_j^\dagger + b_j + b_j^\dagger \right) \left(-a_k - a_k^\dagger + b_k + b_k^\dagger \right) \right. \\
&\quad \left. + \left(a_j - a_j^\dagger - b_j + b_j^\dagger \right) \left(a_k - a_k^\dagger + b_k - b_k^\dagger \right) \right] \\
&= -\frac{\hbar}{2N} \sum_{j=1}^N \sum_{k=1}^N \left[a_j b_k - b_j a_k + a_j^\dagger b_k^\dagger - b_j^\dagger a_k^\dagger - a_j a_k^\dagger - a_j^\dagger a_k + b_j b_k^\dagger + b_j^\dagger b_k \right] \\
&= -\frac{\hbar}{2N} \sum_{j=1}^N \sum_{k=1}^N \left[-a_j a_k^\dagger - a_j^\dagger a_k + b_j b_k^\dagger + b_j^\dagger b_k \right]. \tag{D.8}
\end{aligned}$$

It can be seen that the ab terms cancel (a and b commute) when summing over all indices.

Center of Mass Hamiltonian

We wish to transform the center of mass Hamiltonian H_{CM} in terms of the raising and lowering operators of the quantum Hall problem. In cyclotron units and assuming equal mass particles, the center of mass Hamiltonian is

$$H_{CM} = -\frac{1}{2N} \left(\frac{\partial^2}{\partial x_{CM}^2} + \frac{\partial^2}{\partial y_{CM}^2} \right) + \frac{N}{8} (x_{CM}^2 + y_{CM}^2) + \frac{1}{2\hbar} L_{CM} \tag{D.9}$$

The $x_{CM}^2 + y_{CM}^2$ term yields

$$\begin{aligned}
x_{CM}^2 + y_{CM}^2 &= \frac{1}{N^2} \sum_{j=1}^N \sum_{k=1}^N (x_j x_k + y_j y_k) \\
&= \frac{1}{2N^2} \sum_{j=1}^N \sum_{k=1}^N \left[\left(a_j + a_j^\dagger + b_j + b_j^\dagger \right) \left(a_k + a_k^\dagger + b_k + b_k^\dagger \right) \right. \\
&\quad \left. - \left(a_j - a_j^\dagger - b_j + b_j^\dagger \right) \left(a_k - a_k^\dagger - b_k + b_k^\dagger \right) \right] \\
&= \frac{1}{N^2} \sum_{j=1}^N \sum_{k=1}^N \left[a_j b_k + b_j a_k + a_j^\dagger b_k^\dagger + b_j^\dagger a_k^\dagger + a_j a_k^\dagger + a_j^\dagger a_k + b_j b_k^\dagger + b_j^\dagger b_k \right]
\end{aligned} \tag{D.10}$$

The $\frac{\partial^2}{\partial x_{CM}^2} + \frac{\partial^2}{\partial y_{CM}^2}$ terms become

$$\begin{aligned}
\frac{\partial^2}{\partial x_{CM}^2} + \frac{\partial^2}{\partial y_{CM}^2} &= \sum_{j=1}^N \sum_{k=1}^N \left(\frac{\partial}{\partial x_j} \frac{\partial}{\partial x_k} + \frac{\partial}{\partial y_j} \frac{\partial}{\partial y_k} \right) \\
&= \frac{1}{8} \sum_{j=1}^N \sum_{k=1}^N \left[\left(a_j - a_j^\dagger + b_j - b_j^\dagger \right) \left(a_k - a_k^\dagger + b_k - b_k^\dagger \right) \right. \\
&\quad \left. - \left(-a_j - a_j^\dagger + b_j + b_j^\dagger \right) \left(-a_k - a_k^\dagger + b_k + b_k^\dagger \right) \right] \\
&= \frac{1}{4} \sum_{j=1}^N \sum_{k=1}^N \left(a_j b_k + b_j a_k + a_j^\dagger b_k^\dagger + b_j^\dagger a_k^\dagger - a_j a_k^\dagger - a_j^\dagger a_k - b_j b_k^\dagger - b_j^\dagger b_k \right)
\end{aligned} \tag{D.11}$$

Combining Eq. (D.8), Eq. (D.10), and Eq. (D.11) as in the center of mass Hamiltonian, Eq. (D.9), yields

$$H_{CM} = \frac{1}{2N} \sum_{j=1}^N \sum_{k=1}^N \left(a_j a_k^\dagger + a_j^\dagger a_k \right) \tag{D.12}$$

Hyperangular Operator

The squared grand angular momentum operator \hat{K}^2 in 2-D takes the form [?]

$$\begin{aligned} \hat{K}^2 = & -R^2 \nabla^2 + \sum_{j=1}^N \sum_{k=1}^N \left(x_j x_k \frac{\partial}{\partial x_j} \frac{\partial}{\partial x_k} + x_j y_k \frac{\partial}{\partial x_j} \frac{\partial}{\partial y_k} + y_j x_k \frac{\partial}{\partial y_j} \frac{\partial}{\partial x_k} + y_j y_k \frac{\partial}{\partial y_j} \frac{\partial}{\partial y_k} \right) \\ & + (2N - 1) \sum_{j=1}^N \left(x_j \frac{\partial}{\partial x_j} + y_j \frac{\partial}{\partial y_j} \right) \end{aligned} \quad (\text{D.13})$$

where R is the hyperradius and ∇^2 is the Laplacian operator. Expanding out these terms yields

$$\begin{aligned} \hat{K}^2 = & \sum_{j=1}^N \sum_{k=1}^N \left(x_j x_k \frac{\partial}{\partial x_j} \frac{\partial}{\partial x_k} + x_j y_k \frac{\partial}{\partial x_j} \frac{\partial}{\partial y_k} + y_j x_k \frac{\partial}{\partial y_j} \frac{\partial}{\partial x_k} + y_j y_k \frac{\partial}{\partial y_j} \frac{\partial}{\partial y_k} \right) \\ & - \sum_{j=1}^N \sum_{k=1}^N (x_j^2 + y_j^2) \left(\frac{\partial^2}{\partial x_k^2} + \frac{\partial^2}{\partial y_k^2} \right) + (2N - 1) \sum_{j=1}^N \left(x_j \frac{\partial}{\partial x_j} + y_j \frac{\partial}{\partial y_j} \right). \end{aligned} \quad (\text{D.14})$$

Diagonal Terms

For ease of computation, we break up our calculation of \hat{K}^2 into its diagonal ($j = k$) and off-diagonal ($j \neq k$) parts. There are two contributions to the diagonal terms; the $j = k$ terms of the double sum and the single summation of Eq. (D.14).

First, leaving off the j label for convenience, the double sum becomes

$$\begin{aligned} & \frac{1}{4} \sum_{j=k} \left(a a a^\dagger a^\dagger + a a^\dagger a a^\dagger + a^\dagger a a^\dagger a + a^\dagger a^\dagger a a + b b b^\dagger b^\dagger + b b^\dagger b b^\dagger + b^\dagger b b^\dagger b + b^\dagger b^\dagger b b \right. \\ & \quad - 2 [a a^\dagger b b^\dagger + a a^\dagger b^\dagger b + a^\dagger a b b^\dagger + a^\dagger a b^\dagger b] \\ & \quad \left. + a^\dagger b b^\dagger b^\dagger - a^\dagger b^\dagger b^\dagger b + a^\dagger a a b - a a a^\dagger b - a b b b^\dagger + a b^\dagger b b + a a^\dagger a^\dagger b^\dagger - a^\dagger a^\dagger a b^\dagger \right). \end{aligned} \quad (\text{D.15})$$

Applying the commutator rules Eqs. (D.5) and (D.6) to put as many of the terms into number operator form (e.g. $a^\dagger a$) as possible, after much algebra yields

$$\sum_{j=k} (1 + a^\dagger a a^\dagger a + b^\dagger b b^\dagger b - 2a^\dagger a b^\dagger b + a^\dagger b^\dagger - a b). \quad (\text{D.16})$$

Second, the single summation of Eq. (D.14) becomes

$$(2N - 1) \sum_{j=1}^N \left(x_j \frac{\partial}{\partial x_j} + y_j \frac{\partial}{\partial y_j} \right) = (2N - 1) \sum_{j=1}^N (-1 + ab - a^\dagger b^\dagger) \quad (\text{D.17})$$

Combining Eqs. (D.16) and (D.17) yields

$$-2N(N - 1) + \sum_{j=1}^N \left(\left[a_j^\dagger a_j - b_j^\dagger b_j \right]^2 + 2(N - 1) \left[a_j b_j - a_j^\dagger b_j^\dagger \right] \right) \quad (\text{D.18})$$

where additional factors of N have come from pulling out the 1's from the summations.

Off-Diagonal Terms

The off-diagonal parts of the \hat{K}^2 operator come from the double summation, where it is assumed that $j \neq k$. There are a total of $N(N - 1)$ terms in this summation. In ladder operator form, putting all j indices to the left and all k indices to the right, the off-diagonal part is

$$\begin{aligned} \frac{1}{2} \sum_j \sum_{k \neq j} & \left([aa^\dagger + 2a^\dagger b^\dagger + bb^\dagger]_j [aa^\dagger - 2ab + bb^\dagger]_k \right. \\ & \left. + [a^\dagger a + 2ab + b^\dagger b]_j [a^\dagger a - 2a^\dagger b^\dagger + b^\dagger b]_k \right) \end{aligned} \quad (\text{D.19})$$

where we use a compact notation where a subscript on the parenthesis implies all elements within the parenthesis have that label. Applying the commutator rules Eqs. (D.5) and (D.6) yields

$$\begin{aligned} \frac{1}{2} \sum_j \sum_{k \neq j} & \left(4 + 2[a^\dagger a - 2ab + b^\dagger b]_k + 2[a^\dagger a + 2a^\dagger b^\dagger + b^\dagger b]_j \right. \\ & \left. + [a^\dagger a + 2a^\dagger b^\dagger + b^\dagger b]_j [a^\dagger a - 2ab + b^\dagger b]_k \right. \\ & \left. + [a^\dagger a + 2ab + b^\dagger b]_j [a^\dagger a - 2a^\dagger b^\dagger + b^\dagger b]_k \right). \end{aligned}$$

Expanding and simplifying yields

$$\begin{aligned} 2N(N - 1) + 2(N - 1) \sum_{j=1}^N & \left(a_j^\dagger a_j + b_j^\dagger b_j - a_j b_j + a_j^\dagger b_j^\dagger \right) \\ + \sum_j \sum_{k \neq j} & \left([a^\dagger a + b^\dagger b]_j [a^\dagger a + b^\dagger b]_k - 2 \left(a_j^\dagger b_j^\dagger a_k b_k + a_j b_j a_k^\dagger b_k^\dagger \right) \right). \end{aligned} \quad (\text{D.20})$$

Full \hat{K}^2 Operator

Combining Eqs. (D.18) and (D.20) yields

$$\begin{aligned} \hat{K}^2 = & \sum_{j=1}^N \left([a^\dagger a - b^\dagger b]_j^2 + (2N - 2) [a^\dagger a + b^\dagger b]_j \right) \\ & + \sum_j \sum_{k \neq j} \left([a^\dagger a + b^\dagger b]_j [a^\dagger a + b^\dagger b]_k - 2 \left(a_j^\dagger b_j^\dagger a_k b_k + a_j b_j a_k^\dagger b_k^\dagger \right) \right). \end{aligned} \quad (\text{D.21})$$

Note that only the last term can lead to coupling between Slater determinants.

E. ALGORITHMS FOR COMPUTING ENTANGLEMENT SPECTRUM

Given two Hilbert spaces \mathcal{H}_A and \mathcal{H}_B with complete sets of basis $\{|i\rangle^A\}$ and $\{|j\rangle^B\}$, respectively. Any pure quantum state on the composed system $\mathcal{H}_A \otimes \mathcal{H}_B$ can be written as

$$|\Psi\rangle^{AB} = \sum_{i,j} c_{ij} |i\rangle^A |j\rangle^B. \quad (\text{E.1})$$

The task is to find the reduced density matrices for the subsystems, and then compute the eigenvalues (entanglement spectrum) and the associated eigenstates.

Method I: The reduced density matrix for subsystem A can be computed directly by performing a partial trace over the subsystems B :

$$\begin{aligned} \rho^A &\equiv \text{tr}_B |\Psi\rangle^{AB} \langle\Psi|^{AB} \\ &= \sum_m \langle m|^B \left(\sum_{i,j} \sum_{k,l} c_{ij} c_{kl}^* |i\rangle^A |j\rangle^B \langle k|^A \langle l|^B \right) |m\rangle^B \\ &= \sum_{i,k} \left(\sum_m c_{im} c_{km}^* \right) |i\rangle^A \langle k|^A \end{aligned} \quad (\text{E.2})$$

Thus, represented in the basis of $\{|i\rangle^A\}$, the reduced density matrix of subsystem A has matrix elements

$$\rho_{i,j}^A = \sum_m c_{im} c_{jm}^*. \quad (\text{E.3})$$

Once the reduced density matrix is known, it can be further diagonalized to compute the entropy,

$$\begin{aligned} S_A &\equiv -\text{tr} \rho^A \ln \rho^A \\ &= -\sum_i \lambda_i \ln \lambda_i, \end{aligned} \quad (\text{E.4})$$

where λ_i 's are the eigenvalues of ρ^A .

Method II: The total wavefunction admits a Schmidt decomposition:

$$\begin{aligned} |\Psi\rangle^{AB} &= \sum_{i,j} c_{ij} |i\rangle^A |j\rangle^B \\ &= \sum_i \sqrt{\lambda_i} |\Psi_i\rangle^A |\Psi_i\rangle^B. \end{aligned} \quad (\text{E.5})$$

Here $|\Psi_i\rangle^{A(B)}$ are orthonormal wavefunctions for subsystem $A(B)$. It can be seen that λ_i 's are automatically the eigenvalues for $\rho^{A(B)}$, since $\rho^{A(B)}$ in the diagonal form is

$$\rho^{A(B)} = \sum_i \lambda_i |\Psi_i\rangle^{A(B)} \langle \Psi_i|^{A(B)}. \quad (\text{E.6})$$

λ_i 's as well as the wavefunctions $|\Psi_i\rangle^{A(B)}$'s appearing in the Schmidt decomposition can be computed using the singular value decomposition of the coefficient matrix $\overline{c_{ij}}$:

$$\overline{c_{ij}} = \mathbf{U} \mathbf{\Lambda} \mathbf{V}^*. \quad (\text{E.7})$$

Here $\mathbf{\Lambda}$ is diagonal, \mathbf{U} and \mathbf{V} are unitary matrices. Since

$$c_{ij} = \sum_k \mathbf{U}_{ik} \mathbf{\Lambda}_{kk} \mathbf{V}_{kj}, \quad (\text{E.8})$$

the Schmidt decomposition can be written as

$$\begin{aligned} |\Psi\rangle^{AB} &= \sum_{i,j} c_{ij} |i\rangle^A |j\rangle^B \\ &= \sum_{ij} \sum_k \mathbf{U}_{ik} \mathbf{\Lambda}_{kk} \mathbf{V}_{kj}^* |i\rangle^A |j\rangle^B \\ &= \sum_k \mathbf{\Lambda}_{kk} \left(\sum_i \mathbf{U}_{ik} |i\rangle^A \right) \otimes \left(\sum_j \mathbf{V}_{kj}^* |j\rangle^B \right). \end{aligned} \quad (\text{E.9})$$

It is recognized that Schmidt decomposition is connected to the singular value decomposition of the coefficient matrix $\overline{c_{ij}}$ through

$$\begin{aligned} \lambda_k &= \mathbf{\Lambda}_{kk}, \\ |\Psi_k\rangle^A &= \sum_i \mathbf{U}_{ik} |i\rangle^A, \\ |\Psi_k\rangle^B &= \sum_j \mathbf{V}_{kj}^* |j\rangle^B. \end{aligned} \quad (\text{E.10})$$

Example: Suppose the total system is a chain of four sites. Each site has either 0 or 1 electron. For instance, $|0100\rangle$ is a basis state (Fock basis in the second quantized form) for the total system, which means that there is only an electron on the second site.

Consider the total wavefunction

$$|\Psi^{AB}\rangle = a_1|0101\rangle + a_2|0011\rangle + a_3|1100\rangle + a_4|1010\rangle. \quad (\text{E.11})$$

Subsystem A (B) is chosen as the first (last) two site.

Define the basis for system A as $|1\rangle^A = |00\rangle$, $|2\rangle^A = |01\rangle$, $|3\rangle^A = |10\rangle$, $|4\rangle^A = |11\rangle$. The basis for system B can be labeled in the same way. The total wavefunction, recast into to form of Eq. (E.1), is

$$|\Psi^{AB}\rangle = c_{22}|2\rangle^A|2\rangle^B + c_{14}|1\rangle^A|4\rangle^B + c_{41}|4\rangle^A|1\rangle^B + c_{33}|3\rangle^A|3\rangle^B, \quad (\text{E.12})$$

where $c_{22} = a_1$, $c_{14} = a_2$, $c_{41} = a_3$, $c_{33} = a_4$.

Algorithms: The entanglement spectrum and the associated eigenstates for a quantum Hall ground state can be computed by implementing the methods described above. The crucial step is to find the coefficient matrix $\overline{c_{ij}}$.

The fractional quantum Hall ground state is computed by exact diagonalization in the Fock basis. The target ground state is represented as a linear combination of the Fock basis $\{|k\rangle\}$:

$$|\Psi_g\rangle = \sum_k a_k |k\rangle. \quad (\text{E.13})$$

Each basis is a particular particle occupation, e.g., $|00100\dots1001001\rangle$, which is a product of the basis of the two subsystems, i.e., $|00100\dots\rangle^A \otimes |\dots1001001\rangle^B$. If $|00100\dots\rangle^A$ and $|\dots1001001\rangle^B$ are the i -th and j -th basis for the two subsystems, respectively, Then the coefficient of this particular basis $|00100\dots1001001\rangle$ contributes to the corresponding coefficient matrix element c_{ij} .

However, the subsystems have a large number of basis functions, while the total ground state only involves a small portion of the large basis set. It is inefficient to store the entire subsystem basis set. Instead, the involved subsystem basis are read out through the target ground state. This can be done through the following algorithm:

- Step 1: Create a space to store the subsystem basis set.
- Step 2: Read in the first basis and the corresponding coefficient from the target ground state. Extract the subsystem basis functions in this basis function for the total system.
- Step 3: Compare the extracted subsystem basis with the subsystem basis set. If this subsystem basis function exists in the subsystem basis set, read out its index. If this subsystem basis function does not exist in the basis set, add it to the basis set and create a new index for it. The index is then used to identify the corresponding coefficient matrix element c_{ij} .
- Step 4: Move to the next basis in the target ground state and repeat Step 3.

In the above algorithm, each Fock basis is assigned a unique real number. The basis set is stored as an array of these real numbers. To implement fast search for a given element, the array is sorted using Quicksort algorithm.

VITA

VITA

Bin Yan**EDUCATION**

Ph.D. student, Purdue University, August 2012 – Present

B.S. in theoretical physics, University of Science and Technology of China, June 2008

EMPLOYMENT

Graduate Research Assistant, Los Alamos National Laboratory, July 2018 – Present

Graduate Research Assistant, Purdue University, August 2014 – May 2018

Graduate Teaching Assistant, Purdue University, August 2012 – July 2014

PROFESSIONAL EXPERIENCES

Refereeing – AMS Mathematical Reviews (4), Physical Review Letters (4), Physical Review A (3), Physical Review B (2), Conference on QIP (1), OSA Optica (1)

Teaching – undergraduate general physics laboratory, Purdue University, 2013, 2014

PUBLICATIONS

Bin Yan, Lukasz Cincio, Wojciech H. Zurek, Information scrambling and Loschmidt echo, preprint: arXiv:1903.02651 (2019).

Bin Yan, Rudro R. Biswas and Chris H. Greene, Bulk-edge correspondence in fractional quantum Hall states, Phys, Rev. B 99, 035153 (2018).

Bin Yan, Algebraic probability-theoretic characterization of quantum correlations, Phys. Rev. A 96, 052120 (2017).

Bin Yan, Rachel E. Wooten Kevin M. Daily and Chris H. Greene, Hyperspherical Slater determinant approach to few-body fractional quantum Hall states, Annals of

Physics, 380, 188205 (2017).

Rachel E. Wooten, Bin Yan and Chris H. Greene, Few-body collective excitations beyond Kohns theorem in quantum Hall systems, Phys. Rev. B. 95, 035150 (2017).

Bin Yan and Chris H. Greene, Coupled-square-well model and Fano-phase correspondence, Phys. Rev. A 95, 032706 (2017).

Bin Yan, Quantum correlations are tightly bound by the exclusive principle, Phys. Rev. Lett. 110, 260406 (2013).

PRESENTATIONS

Information scrambling and Fermi's golden rule, APS March Meeting, Boston, MA, March 2019

Bulk-edge correspondence in fractional quantum Hall states, APS March Meeting, Los Angeles, CA, March 2018

Algebraic probability-theoretic characterization of quantum correlations, APS March Meeting, Los Angeles, CA, March 2018

Coupled square well model and Fano-phase correspondence, 48th Annual APS DAMOP Meeting, Sacramento, CA June 2017

Time Domain Fano Resonance, Midwest Cold Atom Workshop, Chicago, IL, October 2016

Connections between fermions and bosons that rotate in two dimensional harmonic traps, 47th Annual APS DAMOP Meeting, Providence, RI May 2016

Hyperspherical approach to the fractional quantum Hall effect, Purdue Quantum Center Workshop on "Quantum Control of Light and Matter, West Lafayette, IN, October 2015